Dissertation
submitted to the
Combined Faculty of Mathematics, Engineering and Natural Sciences
of Heidelberg University, Germany
for the degree of
Doctor of Natural Sciences

Put forward by

M. Sc. Viviane Charlotte Schmidt
born in Wiesbaden (Germany)

Oral examination: 23rd of July, 2024

Study of the unimolecular decay of highly-excited anionic carbon dimers

Referees:

Prof. Dr. Klaus Blaum
Prof. Dr. Roland Wester

Dedicated to the memory of Dr. Robert von Hahn

Untersuchung des unimolekularen Zerfalls hoch-angeregter anionischer Kohlenstoffdimere

Die vorliegende Arbeit umfasst zwei Forschungsschwerpunkte. Im ersten Teil wird der neu implementierte isochrone Betrieb des kryogenen Speicherrings (CSR) in Heidelberg vorgestellt. Er ermöglicht die Identifizierung der im Ring gespeicherten Ionensorten. Dabei werden die Massen der verschiedenen Strahlkomponenten mit Hilfe ihre Flugzeit gemessen. Mit dieser Methode kann man Ionensorten mit relativen Massenunterschieden von $\gtrsim 10^{-5}$ und relativen Strahlanteilen von $\gtrsim 10^{-3}$ auflösen. Außerdem werden erste Versuche zur Entfernung unerwünschter Strahlkontaminationen vorgestellt.
Der zweite Themenschwerpunkt der Arbeit beschäftigt sich mit dem Zerfall von hoch-angeregten C_2^- Dimeren. Bei den zugrundeliegenden Messungen wurden die Anionen in einer Sputter-Quelle erzeugt. Ein kleiner Teil der Dimere hatte so hohe innere Energien, dass es zu spontaner Elektronenablöse (AD) oder Fragmentation (AF) kam. Signale, die von diesen beiden Prozessen herrühren, wurden am CSR gemessen. Detaillierte Berechnungen der Raten der destruktiven Zerfallskanäle AD und AF sowie der radiativen Abregung durch Photonenemission wurden für eine große Anzahl von ro-vibronischen Zuständen durchgeführt. Die gemessenen Signale konnten mit Hilfe eines Zerfallsmodells reproduziert werden. Darüber hinaus konnte das Millisekunden-AD-Signal von C_2^-, das bereits an mehreren anderen experimentellen Einrichtungen beobachtet wurde, zum ersten Mal durch einen neuen Mechanismus, der rotationsunterstützten Elektronenablöse, erklärt werden.

Study of the unimolecular decay of highly-excited anionic carbon dimers

The research focus of this thesis is two-fold. First, the newly implemented isochronous operation of the Cryogenic Storage Ring (CSR) in Heidelberg is presented. It enables the identification of the stored ion species, including molecular isobars. Here, the masses of the different beam components are measured through their flight time. The method is sufficient to resolve species with relative mass differences of $\gtrsim 10^{-5}$ and relative beam fractions $\gtrsim 10^{-3}$. Furthermore, first attempts to remove unwanted beam-contaminants are presented.
The second research focus of this thesis is on the decay of highly-excited C_2^- dimers. In the underlying measurements, the anions were produced in a sputter source. Consequentially, a small fraction of the dimers had sufficiently high internal excitation to undergo spontaneous auto-detachment (AD) or auto-fragmentation (AF). Signals stemming from both of these processes were recorded at the CSR. Detailed rate calculations for the destructive decay channels, AD and AF, as well as radiative relaxation were carried out for a wide range of ro-vibronic states. The measured signals could be reproduced employing a decay model. Furthermore, the millisecond AD signal of C_2^- already observed at multiple other facilities could be explained for the first time by a new mechanism of rotationally assisted auto-detachment.

Contents

1 Introduction

It was Amedeo Avogadro in the year 1811, who first discussed the possible existence of molecular systems [1]. In his work he considered different gases and the components they consist of, which he all called "molecules". Here, he distinguished between "single molecules" (which one would call "atoms" today) and "compound molecules" (today's molecules). In this study he came to the conclusion that the "molecules" which make up pure oxygen or nitrogen gases must each consist of two "half-molecules". This observation presents the first published description not only of a molecule but also of a homo-nuclear diatomic system.

Since Avogadro's postulation of their existence, molecules have become an established field of research in both physics and chemistry. Next to a wide range of diatomic molecules [2], also a vast number of more complex systems have been discovered [3] not only on earth but even in space [4]. These were additionally found to exist in different charge configurations (neutral or singly/multiply positively/negatively charged). In contrast to the inquiries in 1811, the atomic composition of these species is now well understood. The focus of the study of molecules has therefore shifted over the centuries.

The large success of the theory of quantum dynamics in the 1920s facilitated the rise of a new area of research, molecular quantum dynamics (also known as "quantum chemistry"). Molecules were now considered as complex quantum systems with discrete states described through wave functions. Advances both in experimental techniques as well as theoretical (computational) models over the following decades enabled an increasingly detailed understanding of these systems.

In these studies, the investigation of the internal states available within a molecule proved to be particularly interesting. The states were found to exhibit different properties. These were, for example, the energy available in the system, the motion of the constituent particles (atoms and electrons), timescales on which the system occupies these states, chemical reaction rates with other species and even the probability of the molecule's destruction through the break-away of one or multiple of its constituent particles. The ability of the molecule to go from one state to another was found to be governed by the rules of quantum mechanics. Depending on the initial state of the molecule and its environment, different types of state changes, "transitions", are possible.

One type of such transitions is the radiative decay of excited molecules. Here, the system is initially in a state with internal energy E_i and goes to a lower state with internal energy $E_f < E_i$. This process happens via the emission of one or multiple photons, through which the excess energy $E_i - E_f$ is radiated away. The molecule itself stays intact during the transition and merely changes its internal state. However, if the amount of energy in the system is sufficiently large, the molecule can break apart instead. This can for example happen through fragmentation, where one or multiple atoms break away from the system. Another process is the ejection of one or multiple electrons. This mechanism is especially interesting for negatively charged species, which consist of more electrons than protons. Here, the excess electrons are typically only weakly bound. Depending on the internal state of the molecule, multiple different decay mechanisms might be available at once and in competition with each other. The likelihood that the system will decay through one of the channels can then be estimated by comparing the probabilities for the different mechanisms. If this probability is significantly larger for one mechanism than the others, the molecule will predominantly decay through this channel.

A method which proved successful in studying different decay channels is the experimental investigation of the unimolecular decay of highly-excited, negatively charged molecules [5, 6, 7, 8, 9, 10, 11]. Here, the species are either produced with large internal energies or excited, e.g., by the radiation with photons. Afterwards, their decay is monitored over a prolonged period of time, even seconds and beyond. An ideal molecular system to study different decay processes and their competition is the negatively charged carbon dimer C_2^-. It offers a large number of internal excitations with vastly varying decay probabilities and mechanisms [12, 13, 14, 15]. Furthermore, while it is known for more than two decades that the system can eject its excess electron on millisecond timescales, the underlying mechanism has long been a mystery [16, 17, 18, 19].

To study the properties of molecular ions experimental set-ups, which enable the storage of charged particles through electrostatic and/or magnetic fields, are typically employed [20, 21, 22, 23, 24, 25]. One such device is the electrostatic Cryogenic Storage Ring (CSR) [20], located at the Max-Planck-Institut für Kernphysik in Heidelberg. It can be used for a number of different experiments to investigate the properties of charged atomic and molecular systems [26, 27, 28]. For these studies, it is important that the correct species, and ideally only this selected molecular or atomic species, is stored inside the device. To this end, efficient methods have to be implemented to detect the different constituents of the stored ion beam and remove the unwanted contaminants.

The rest of this thesis is structured as follows: First, the experimental facility, the Cryogenic Storage Ring (CSR) at the Max-Planck-Institut für Kernphysik in Heidelberg, is described in Chapter 2. Afterwards, the implementation of a new method to identify the different species stored inside the CSR is presented in Chapter 3. The approach applied here is the isochronous operation of the ring, which is demonstrated for the first time in an electrostatic storage ring. It enables the identification of different species according to their masses. The chapter furthermore outlines first attempts to remove unwanted species stored inside the ring.

Following these two technical chapters, Chapter 4 then focuses on the decay of highly-excited C_2^- anions. Here, theoretical calculations are preformed to model and compare the expected auto-detachment and auto-fragmentation rates to experimental results obtained at the CSR. To this end, a variety of decay channels available in the system are investigated. The results include a likely explanation of the millisecond auto-detachment signal, which has so far been unknown. The corresponding mechanism, rotationally assisted auto-detachment, is described for the first time in the course of this project. In the end, a summary of the work presented in this thesis and an outlook are given in Chapter 5.

2 The Cryogenic Storage Ring (CSR)

This chapter provides a brief introduction into storage ring physics and important parameters (Sec. 2.1) before presenting a summary of the main features of the Cryogenic Storage Ring facility in Sec. 2.2.

2.1 A short introduction into Storage Ring Physics

2.1.1 Three-dimensional confinement of charged particles

As Samuel Earnshaw already remarked in 1842, it is impossible to confine one (or multiple) charged particle(s) in a stable static equilibrium using electromagnetic potentials (Earnshaw's theorem). This apparent dilemma for physicists with the desire to study charged particles under well-defined storage conditions has been circumvented with a multitude of different experimental set-ups over the years. All rely on the Lorentz force, which describes the influence of electric $\vec{E}$ and magnetic $\vec{B}$ fields on the trajectory of a charged particle:

$$\vec{F_L} = q\vec{E} + q\vec{v} \times \vec{B}. \tag{2.1}$$

Here, m, q and $\vec{v}$ are the particle's mass, charge and velocity, respectively.

Different configurations using static or dynamic electric and static magnetic potentials, or combinations of those, can be used to achieve well-defined 3D-confinement of charged particles. One set of such devices are ion traps, four notable examples will be shortly listed here. In a Paul trap, a combination of a static and dynamic electric field is used to confine the charged particles in two dimensions [29]. These devices are often used as mass filters. The 22-pole trap can be seen as an extension of the Paul trap. It features a larger field-free region in the trap center, creating good conditions also for measurements focusing on, e.g., spectroscopy or buffer gas cooling. A Penning trap uses both an electrostatic and a magnetic field to achieve trapping and is predominantly used for high-precious experiments [30]. In an electron ion beam trap (EIBT) or Zajfman trap, the ions oscillate between two electrostatic mirrors, while ion optical elements provide the sufficient focusing to achieve 3D confinement [31]. The different devices offer varying advantages and disadvantages with respect to mass/momentum acceptance, amount of particles stored simultaneously, ability to probe the the stored particles and many more. The other set of devices employed to study ions on well-defined trajectories are storage rings. These will be discussed in more detail in the next Section 2.1.2.

2.1.2 Storage ring basics

This sub-section introduces basic concepts of particle movements in storage rings. Here, the focus is placed on devices which store ions at a constant energy. Other types of storage rings, for example electron synchrotrons like DESY in Hamburg [32] are not considered here.

Ions are generated in an ion source and accelerated to the desired kinetic energy. The resulting ion beam is then guided towards a storage ring and injected into the device. Here, the ions are stored on trajectories that in first approximation resemble a circle. To this end, the strength of the Lorentz force is chosen such that it equals the centrifugal force of the ions' orbit with curvature ρ inside the ring,

$$|\vec{F}_L| = \frac{mv^2}{\rho}. \tag{2.2}$$

This can either be achieved through electrostatic or magnetic fields (see Eq. (2.1)), which can be realized by two different types of storage rings: electrostatic storage rings or magnetic storage rings. However, the principle of ion confinement employed in both cases are the same.

Inside the device, the ions are guided by dipole fields resulting in the approximately circular trajectory. Quadrupole fields and sometimes higher order fields shape the ion beam. For describing the particles' motion inside the ring, it is advantageous to define a *central orbit* on which an ideal ion, the *synchronous particle*, flies. This path goes through the center of all ion optical elements. In practice, particles predominantly do not propagate on the central orbit, but on *closed orbits*. These paths also form an approximately circular motion inside the ring, but do not go through the center of all optical elements. Particles on these trajectories are constantly refocused on their closed orbits by the quadrupole (and sometimes higher order) fields.

It is convenient to define a co-moving coordinate system for the ion's trajectory, where s is the path along the closed orbit and x and y are the displacement from this ideal path in both dimensions, as is shown in Fig. 2.1. The particle's motion around the closed orbit is called *betatron oscillation* and is described by the *betatron functions* $\beta_{x,y}$ for the two dimensions [33]. The number of betatron oscillations a particle performs within one revolution is called the *tune*,

$$Q_{x,y} = \frac{1}{2\pi} \oint \frac{ds}{\beta_{x,y}(s)}. \tag{2.3}$$

While the strength of the dipole fields is determined by the kinetic energy (momentum) of the ions in an electrostatic (magnetic) ring, storage is possible for a number of configurations for the focusing fields. These *modes* are characterized by different storage ring parameters, which are introduced in Sec. 2.1.3.

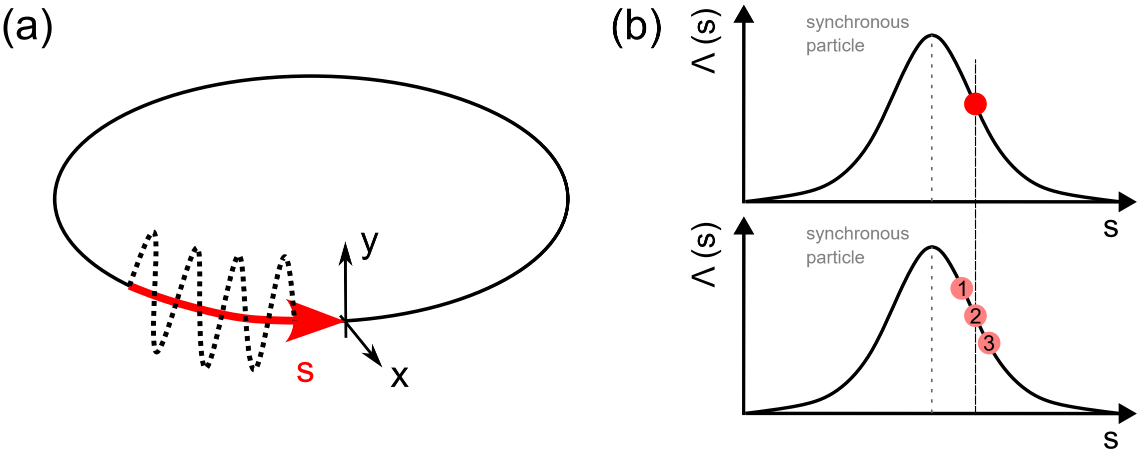

Figure 2.1: (a) Schematic drawing of an ion's trajectory in a storage ring. The solid black line represents a closed orbit, with the co-moving coordinate s and perpendicular coordinates x and y. The dashed line shows a betatron oscillation of an exemplary particle. (b) Space charge distribution Λ as a function of the co-moving coordinate s. A dashed line indicates the position of the synchronous particle. The upper panel shows the position of an exemplary particle (red circle) inside the ion pulse. The lower panel shows the position of this particle after one revolution for slip factors $\eta < 0$, $\eta = 0$, and $\eta > 0$ marked with 1, 2, and 3, respectively.

Typically a large number of ions ($> 10^4$) are injected in a pulse called *bunch* into the device. As a result, the ions' motion is not only influenced by the electrostatic/magnetic fields of the ring's optical elements but also by the *space charge*. The stored ions have the same charge state and therefore experience Coloumb repulsion from the other particles. Ions within a bunch will experience a position dependent force, given by the *space charge distribution* $\Lambda(s)$. The magnitude of this space charge field in longitudinal direction $E_{||}$ is directly proportional to the derivative of $\Lambda(s)$ [34]

$$E_{||} \propto -\frac{\delta\Lambda(s)}{\delta s}. \tag{2.4}$$

This force points outwards of the bunch. As a result, particles positioned at the front/back of the ion pulse will be accelerated/decelerated by the space charge field. The behaviour of the bunch structure with storage time due to this effect will be discussed for different modes in Sec. 2.1.3.

While the basic principles of electrostatic and magnetic storage rings are the same, there are also notable differences between the two types. One is the mass dependence of the necessary deflection field to achieve storage. Electrostatic fields deflect according to the kinetic energy-to-charge ratio E/q of the ions, while in the case of magnetic storage rings there is an additional momentum (and therefore mass) dependence for a given kinetic energy (see Eqs. (2.1) and (2.2)). As a result, electrostatic storage rings offer an advantage for the study of heavy, e.g., molecular, ions species in low charge states with large momentum. Due to the technological limitation in electrostatic field strength, all electrostatic storage rings are operated at non-relativistic kinetic energies of the particles, in contrast to most magnetic devices. Furthermore, the electrostatic facilities are typically smaller in size and cryogenic operation is possible [20, 21, 24]. The rest of this chapter concentrates on electrostatic storage rings and their properties, although many features can be transferred to magnetic devices as well.

2.1.3 Relevant storage ring parameters

In this section storage ring parameters relevant for this work are introduced. They describe the performance of the mode the electrostatic device is operated in, which is predominantly given by the settings of the focusing elements (see Sec. 2.2.2).

The *acceptance* is defined as the maximum phase-space area, which can be occupied by the stored particles, divided by π. Its value influences the maximum value of parameters like energy spread, number of ions and emittance of an ion bunch stored in the ring.

The *working point* (Q_x, Q_y) is given by the two tunes (see Eq. 2.3). In order to achieve stable storage, the working point cannot lie on a resonance, for which the following condition applies

$$n_x Q_x + n_y Q_y = k \qquad \text{with } n_x, n_y, k \in \mathbb{Z}. \tag{2.5}$$

This is due to small impurities of the storage ring fields, which perturbate the ion's orbit. If the working point lies on a resonance, the ions will periodically fly on the exact same path inside the ring within their betatron oscillations. Consequentially, they will repeatedly see the same field. This generates periodic, resonance-like enhancements of the trajectory perturbations due to the small field impurities. This leads to a constant orbit distortion, which will eventually move the ions out of the ring's acceptance. Since the two tunes (Q_x, Q_y) can couple, the same condition also applies for combinations of both.

The *slip factor* η describes the dependence of the revolution frequency f of a particle on its momentum p,

$$\eta = \frac{\Delta f / f}{\Delta p / p}. \tag{2.6}$$

The relative momentum and frequency deviation of a particle, Δp and Δf, respectively is always given with respect to the *synchronous particle* (see Sec. 2.1.2). The relative revolution time difference of an ion with kinetic energy E, mass m and charge Q with respect to the synchronous particle is given by

$$\frac{\Delta T}{T} = \frac{1}{2}\frac{\Delta(m/Q)}{m/Q} - \frac{\eta}{2}\frac{\Delta(E/Q)}{E/Q} \tag{2.7}$$

in first order [34]. One can distinguish between three different operation modes, which are defined by the slip factor:

$\eta > 0$ If the slip factor is larger than zero, the ring operates in a *dispersive* mode. Here, the revolution time of the particles increase with increasing momentum. Due to the momentum spread of the stored beam, the injected ion pulse will increase with storage time until the particles are approximately equally distributed in the ring. Furthermore, the ions will experience a change of momentum dependent on their position within the bunch. An ion situated at the front of the pulse, for example, experiences an accelerating force. The momentum increase and consequentially the revolution time decrease (see Eq. (2.6) for $\eta > 0$) will move the particle further in front of the synchronous particle in the next revolution. This is shown in case 3 in Fig. 2.1(b).

$\eta = 0$ In the case, where the particle's revolution time inside the ring becomes independent of the kinetic energy (see Eq. (2.6) for $\eta = 0$), the *isochronous* condition is reached. Here, the momentum deviation from the synchronous particle will not change the position of the ion inside the bunch, as is shown in case 2 in Fig. 2.1(b). Consequentially, the particles will always experience the same space charge field and therefore a constant acceleration/deceleration. The resulting energy increase/decrease will eventually result in the loss of the particles as they leave the acceptance of the ring.

$\eta < 0$ For negative slip factors, the operation enters the *self-bunching* regime. Here, e.g. for ions which experience an increase in momentum by the space charge, the revolution time will decrease (see Eq. (2.6) for $\eta < 0$). This will cause the particle to move closer to the synchronous particle in the next revolution, as is shown by case 1 in Fig. 2.1(b). This trend will continue until the ion moves behind the synchronous particle. At this point, it will start experiencing a decelerating force, which induces an increase in revolution frequency. As a result, the ions will oscillate inside the bunch around the position of the synchronous particle.

The slip factor is determined by the *dispersion function* $D_p(s)$ inside the storage ring. The dispersion describes the horizontal displacement of particles with a momentum deviating from the mean value with respect to the closed orbit.

In some cases the γ_{tr} *parameter* is used instead of the slip factor. The relation between the two is given by

$$\eta = 1 - \frac{1}{\gamma_{tr}^2}. \tag{2.8}$$

Additionally, the *momentum compaction factor* α_p describes the change of the closed orbit length C with a change in the ion's momentum p, which can also be expressed via the slip factor [34]

$$\alpha_p = \frac{\Delta C/C_0}{\Delta p/p_0} = \frac{1-\eta}{2}. \tag{2.9}$$

Here, C_0 is the length of the central orbit and p_0 the momentum of the synchronous particle.

2.2 The Cryogenic Storage Ring facility

The electrostatic Cryogenic Storage Ring (CSR) is located at the Max-Planck-Institut für Kernphysik in Heidelberg, Germany. An overview of the facility is shown in Fig. 2.2. The beam path of the ≈ 35 m circumference ring is housed in a nested two-chamber system. The inner experimental chambers can be cooled down to temperatures of about 4 K using a closed-cycle liquid helium system. As a result, very low effective radiation fields can be reached (see for example Meyer et al. [26]). Furthermore, the cold experimental chambers act like a cryopump, enabling residual gas densities in the order of 1000 particles/cm^3. The experimental chambers are shielded from the 300 K radiation by two layers of shields to avoid direct radiation, super-insulation, and a second isolation chamber system to minimize convective heating. A detailed description of the facility can be found in [20].

This section shortly describes the main characteristics of the CSR facility, starting with the ion production and selection in Sec. 2.2.1, followed by an outline of the optical elements and diagnostics in the ring in Sec. 2.2.2, as well as an overview of the different experimental stations in Sec. 2.2.3.

2.2.1 Ion production and injection into CSR

The ion species stored inside CSR are produced on one of two different high-voltage platforms. For the measurements contributing to this thesis, only the high-voltage platform labelled "1" in Fig. 2.2 was employed and only its beamline towards CSR will be shortly discussed here. A description of the small high-voltage platform, labelled "2" in Fig. 2.2, can for example be found in [28]. The potentials of the high-voltage platform number 1, can be set to reach a total acceleration of the particles up to ±300 keV per elementary charge. Ions produced on this potential

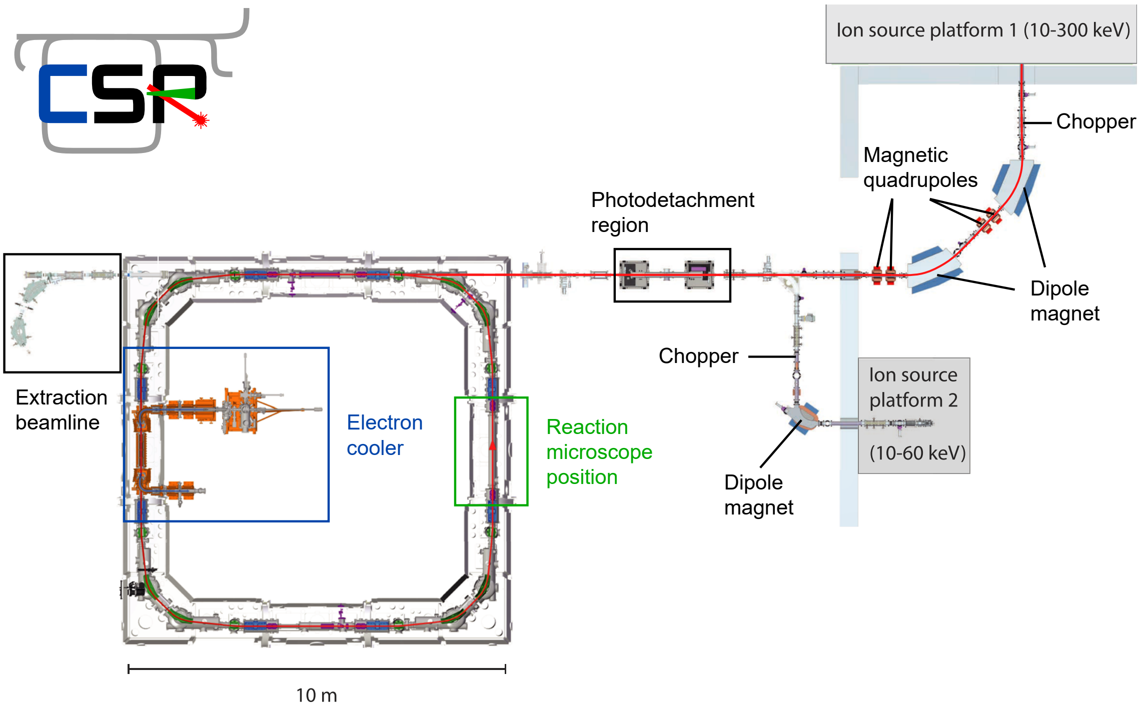

Figure 2.2: Overview picture of the CSR facility including the two high-voltage platforms and injection and extraction beamlines, modified from [28]. A red line marks the path of the ions from platform 1 into the CSR and inside the ring. In the top left corner of the figure: The CSR logo designed in the course of this thesis.

are accelerated to ground when leaving the platform. A fast electrostatic deflector, called "chopper", is installed in the beginning of the injection beamline. It creates short pulses for injection out of the continuous ion beam produced in the source. Afterwards, two dipole magnets deflect the produced ions according to their mass-to-charge ratio m/q. The magnets serve two functions, they are both acting as a beam guide to direct the ions towards the storage ring and function as a mass filter. This is crucial due to the electrostatic nature of the CSR, which stores ions according to their kinetic energy-to-charge ratio E_{kin}/q. The mass resolution of the dipole magnet pair alone is approximately $\Delta m/m = 130$ for a beam with 200 keV kinetic energy [35]. Quadrupole magnets placed before and after the dipole elements are used to focus the beam.

The high-voltage platforms of the CSR can be equipped with a number of ion sources to produce both positively and negatively charged ion beams. For the data discussed in this thesis, a Middleton Ion Sputter Source (MISS) was used. Here, caesium cations are accelerated towards a target. The impinging ions sputter material from the surface. As a result, a range of molecules and clusters are produced.

For the formation of negative species, neutral caesium present in the source can act as an electron donor [36]. Due to the harsh creation process, the resulting particles are typically highly internally excited with previous studies putting the vibrational and rotational temperature in the range of a few thousand Kelvin [37, 38, 39, 40]. Possible population models stemming from this type of source will be discussed in Sec. 4.6.2. Produced species can be made up both of atoms present in the target material as well as any gasses present in the source. Due to the applied acceleration voltage for Cs^+, only negative species are extracted from the source which are predominantly singly charged. Further sources available at the facility are a Penning source [41], an ECR source, a duoplasmatron source, Laser vaporisation source, etc..

2.2.2 Optical lattice and diagnostics of CSR

Fig. 2.3 shows a schematic drawing of the optical elements and diagnostic tools of the CSR. The ions are kept on orbit by **dipole deflectors and quadrupole electrodes** placed in identical configuration in each of the four corners. The 90° bend is achieved by two 39° deflectors and two 6° deflectors, which a framed by two quadrupole doublets. Voltages applied to the deflectors are identical for all of the corners, while the quadrupole setting can vary to run the ring in different modes (see Sec. 2.1). Currently, the quadrupoles can be grouped together in up to four families, which are sets of quadrupoles where the same absolute voltage is applied.

In order to measure the ion beam position inside the ring, Sections (A), (C) and (D) have position pick-ups while Section (B) features wire scanners (see Fig. 2.3). They were not relevant for the measurements discussed in this thesis. However, the interested reader can find details about the functionality and performance of these devices in reference [42].

The CSR is furthermore equipped with a **Schottky pick-up** in Section (C) (see Fig. 2.3). The details of this diagnostic tool are given in [42] and will only briefly be summarized here. This device is used to measure the revolution frequency of coasting or bunched ion beams inside the ring. Ion bunches induce a mirror current and thus an induced voltage each time they pass through the cylindrical pick-up electrode. This periodic signal can be read out and turned into a frequency spectrum by applying a Fourier transformation, which is done by a spectrum analyzer.

A drift tube, called the **rf system**, is available in Section (A) of the CSR (see Fig. 2.3). It consists of two segments, an advantage for the ion-neutral experiments performed in this section [28], however, for the measurements discussed in this thesis one segment of the system was grounded. A sinus shape potential is applied on the other segment, when the rf system is switched on. Depending on the phase, ions passing the drift tube are either accelerated or decelerated by the changing potential. When the frequency of the rf-system matches a harmonic of an ion species revolution frequency inside the CSR, the ions can either be bunched in non-isochronous operation or excited out of the ring's energy acceptance in isochronous operation,

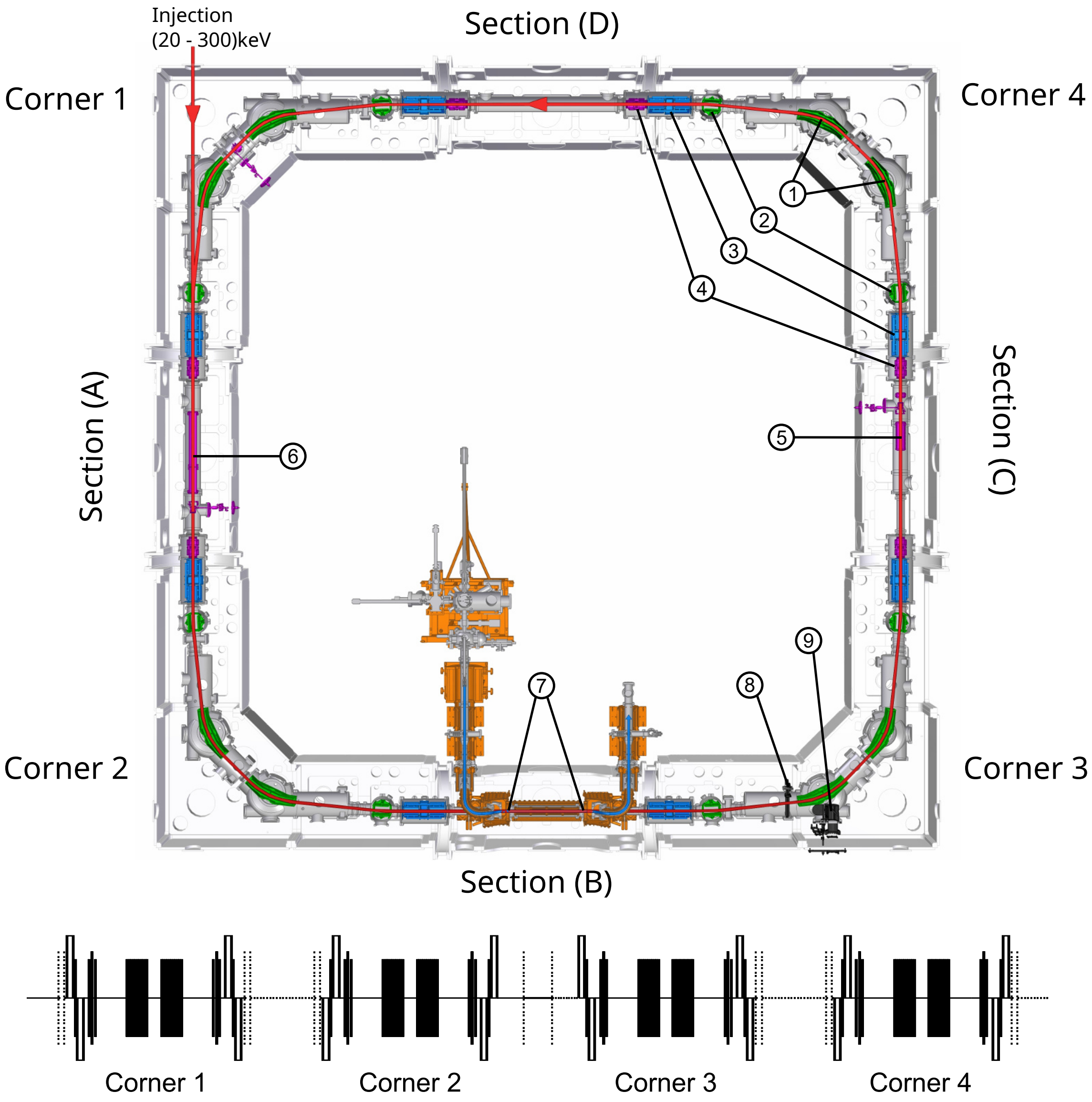

Figure 2.3: Overview of the optical elements and diagnostics inside the CSR, modified from [20]. Upper panel: (1) 39° deflectors, (2) 6° deflectors, (3) quadrupole duplets, (4) position pick-up electrodes, (5) Schottky pick-up, (6) RF-system, (7) wire-scanners, (8) COMPACT detector, (9) NICE detector. The elements (1)-(3) are identical in all corners, while the position-pick-up electrodes are present in all sections except in section (B), where instead the wire-scanners are implemented. Lower panel: Optical lattice of the CSR. Closed/open rectangles mark the deflectors/quadrupoles. The dashed lines correspond to the positions of the pick-up electrodes and the wire-scanners.

which will be further discussed in Sec. 3.4.4 and Sec. 3.4.2, respectively. A detailed description of the CSR's rf system is given in [42].

2.2.3 Experimental stations of CSR

The primary research aim of the CSR is the study of molecular ions. This includes spontaneous destruction of highly-excited species as well as collision experiments between internally cold molecules with a range of particles (photons, electrons, neutral atoms and molecules) [43]. For latter, different interaction regions are build into the straight sections of the ring. These feature a variety of single particle detectors placed strategically to measure products from the interaction experiments. In Section (A) the stored molecular ions can be merged with neutral atomic or molecular beams to study reactions of astrochemical relevance [28]. In-ring detectors and an extraction beamline in corner 2 measure the reaction products (see Fig. 2.2).

An electron cooler is situated in Section (B) of the CSR (see Fig. 2.3). It can cool the ion beam through elastic collision and reduce the beam's area in the phase space. This feature, which is predominantly employed in magnetic storage ring facilities, originally earned it the name of "cooler" [44]. Additionally, it can also cool the molecular ions' internal excitations through inelastic collisions. This process was first experimentally verified for rotational deexcitation at the CSR [45]. Furthermore, the electron beam can be used as a target for merged beam experiments with the stored molecular and atomic ions, where the process of electron capture and possibly the sub-sequential decay of the often highly-excited formed species is studied [27, 46, 47]. Different types of continuous-wave (cw) and pulsed lasers can be coupled into Section (B) as well to carry out photo-detachment and photo-dissociation measurements [48, 26, 49].

Two detectors placed in corner 3 of CSR are relevant for the measurements presented in this thesis and are marked in Fig. 2.3. One is the MCP-based COld Movable PArticle CounTer (**COMPACT**) detector [50]. It is placed behind the first 6° deflector in corner 3 and can be moved perpendicular to the ion beam. This enables the detection of charged and neutral reaction products created in Section (B). Additionally, it can destructively sample ions stored on large orbits inside the ring, depending on the position of the detector. COMPACT has a darkcount rate below 0.1 Hz and an efficiency close to unity [50]. The second detector in corner 3 is the Neutral particle Imaging in Cold Environment (**NICE**) detector. It is employed to detect neutral reaction products produced in the preceding straight section [51]. NICE is positioned in the neutral port of corner 3, which is located in the path of neutral reaction products that are not deflected by the ion optical elements. It has imaging capability not available for COMPACT. At about 50 Hz this detector's dark count rate is much higher though.

Section (C) does not facilitate any experimental set-up and is instead home to the CSR's beam monitoring tools [42], while Section (D) features a newly installed cryogenic reaction microscope [52], which however was not yet implemented when the data presented in this thesis was taken.

3 Mass measurements and beam purification at the CSR

The primary research focus of the CSR is the detailed study of reaction processes of astrophysical relevance involving molecular ions. Here, it is desirable to perform measurements with only one species stored in the ring at a time. Otherwise, the assignment of the measured rates to a specific molecule are often difficult to impossible. However, commonly used ion sources produce a variety of different molecules simultaneously and the selection of only a single specie of interest prior to the injection into the CSR is not always possible. This problem can be addressed in a two-step process. First, the molecular composition of the stored beam inside the ring has to be determined. Afterwards, undesirable species (contaminations) have to be removed from the beam.

At the CSR facility, the ions are produced at one of the high-voltage ion source platforms and accelerated to the desired kinetic energy when leaving the platforms' potentials (see Sec. 2.2.1). Bending magnets in the injection beamline act as a mass-to-charge separator for the produced ions. Their resolving power ($\Delta m/m \approx 130$ at $200\,\mathrm{keV}$) enables the separation of species with different integer masses. However, they are not sufficient to filter out all possible contaminants inside the ion beam. The most critical of those are molecular isobars. These are species, which have the same total number of nucleons, but different atomic compositions, for example $^{12}\mathrm{C}_4^{16}\mathrm{O}^-$ and $^{16}\mathrm{O}_4^-$ ($m \approx 64\,\mathrm{u}$). They typically have a relative mass difference in the range of $10^{-4} - 10^{-5}$. All ions which pass the bending magnets and are injected into the CSR will be stored in the device. This is due to the electrostatic nature of the ring's optical elements.

In principle, the slightly different masses of the stored species would enable their separation with Time-of-Flight (ToF) methods. These rely on the difference in propagation time of ions with the same kinetic energy but slightly different masses and hence velocities. However, processes during ion production (location of ionization in the source potential, charge distribution inside the source,...) result in a kinetic energy spread of the ions. In order to ensure a large ion number inside the CSR, both the injection beamline and the ring itself were optimized to have a large momentum acceptance of several 10^{-3} [20]. Therefore, ion beams stored inside the ring typically exhibit a kinetic energy spread up to a range of a few 10^{-3}. In the case of large mass differences ($\Delta m/m \gtrsim 0.01$), the difference in revolution frequency can be sufficient for the species to separate inside the ring despite the momentum spread. However, for contaminants with small mass differences and therefore small revolution time differences compared to the kinetic energy spread, the separation in normal (non-isochronous) operation is difficult to impossible. Here, the only option for identification in non-isochronous operation is typically specific features in reaction rates (photo-dissociation, electron recombination), which have to be previously known.

The isochronous operation of the CSR, presented in this chapter, was motivated by the need for an in-ring method to resolve all ion species in the stored beam. The procedure must have a mass resolution sufficient to separate molecular isobars. These have a relative mass difference $\Delta m/m$ of typically 10^{-4} or less. Furthermore, the sensitivity of the method has to be sufficient to detect contaminants which make up only very small fractions of the beam. The sensitivity required varies for different reaction processes of interest, therefore it is not possible to put a hard lower limit here. However, identification of beam fractions below 10^{-4} can be seen as a appropriate goal. After the identification of contaminants in the CSR, the removal of these species from the stored beam is the final step towards contaminant-free measurements in the ring.

The rest of this chapter is structured as follows. First, a short introduction into isochronous mass measurements is given in Sec. 3.1. Here, a primary focus is placed on electrostatic storage rings before other types of devices are shortly discussed in Sec. 3.1.1. Afterwards, the set-up of the CSR in the isochronous mode is summarized in Sec. 3.2. The two methods employed for mass measurements, using the revolution frequency or the revolution time of the ions in the ring, are presented in Sec. 3.3. First attempts to clean the beam of contaminants during storage in the ring are described in detail in Sec. 3.4. At the end, a discussion and outlook are given in Sec. 3.5.

3.1 Introduction to isochronous mass measurements

The mass of a particle is a fundamental property. If measured with sufficient accuracy, it can not only identify the particle unambiguously, but also act as a test for theory from the standard model to new physics [30]. Penning-trap experiments currently offer the highest precision mass measurements of charged particles, where recently a relative mass uncertainty of 4×10^{-12} could be reached [53]. However, these set-ups have their limitations. In cases where very short-lived species are under investigation or the mass distribution of a large number of ions has to be determined, isochronously operated storage rings and electrostatic ion beam traps (EIBT) are typically employed [30, 54, 55, 56]. Latter are also referred to as Multi-Reflection Time-of-Flight (MR-ToF) devices when used for mass measurements. Their functionality will be explained below.

In storage ring or EIBT experiments, the masses of ions are determined by measuring the periodic motion of the particles inside the devices. Here, either the revolution

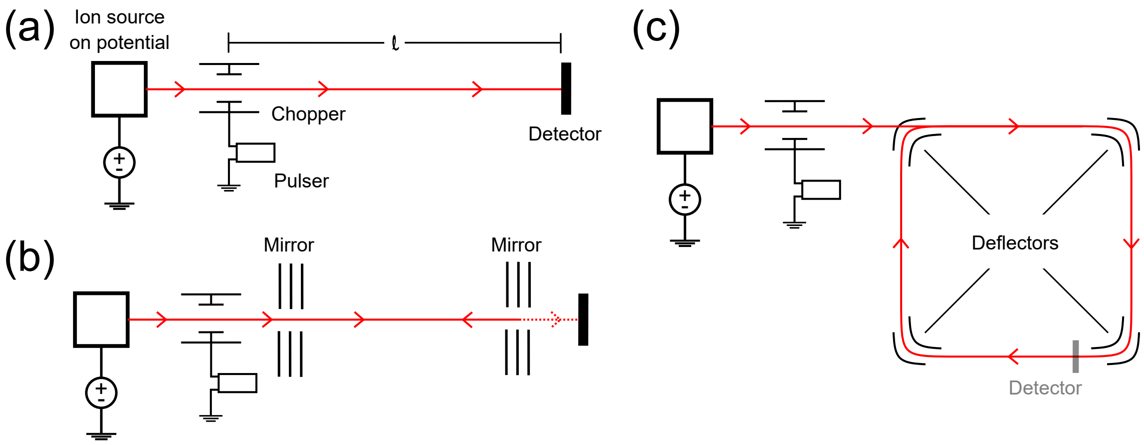

Figure 3.1: Schematic drawing of Time-of-Flight set-ups: (a) Single Pass experiment, (b) Multiple-Pass (MR-ToF), (c) Storage Ring

frequency or its inverse, the revolution time, can be considered. For the latter case, the Time-of-Flight (ToF) method is used. A schematic drawing of the simplest form of a ToF experiment is shown in Fig. 3.1(a). Different species are accelerated by the same electrostatic potential. An ion pulse is created, for example using a chopper, if a continuous beam comes out of the source. The ion of interest with mass m can be "weighted" against a reference with a known mass m_0 by measuring the time both ions take to travel a fixed distance l,

$$\frac{m}{m_0} = \left(\frac{T}{T_0}\right)^2 . \tag{3.1}$$

Here, T and T_0 are the flight times of the ion of interest and the reference, respectively. For the sake of simplicity non-relativistic kinetic energies are considered, which are available in the CSR. In an experiment the arrival times on the detector can only be measured to a certain precision. In order to enhance the mass resolution it is therefore advantageous to increase the propagation length of the ions. This can be achieved by sending the particles along the same path many times. Fig. 3.1(b) shows a simplified drawing of a possible multi-pass set-up, in this case a Multi-Reflection Time-of-Flight (MR-ToF) device [57, 56]. Here, the ions oscillate between electrostatic mirrors. Particle detection can be carried out by a detector placed behind one of the electrostatic mirrors. It collects either neutral fragments produced in the trap, which were flying towards the detector during neutralization. Or it can be used to measure ions trapped in the device directly. To this end, the voltages of the mirror in front of the detector are lowered after a chosen number of revolutions and the ions are are dumped for detection. Another option to recycle the same path of the ions many times is a storage ring. A schematic drawing of which is shown in Fig. 3.1(c). The concept of these devices has already been introduced in Chapter 2. The rest of this section will introduce the principle of mass measurements based on electrostatic storage rings with non-relativistic energies. A comparison to isochronous mass measurements in MR-ToF devices and magnetic storage rings is given in Sec. 3.1.1.

The relation in Eq. (3.1) is valid in the ideal scenario, where the kinetic energy spread is zero ($\Delta E = 0$) and the trajectory of the different species is identical. In electrostatic devices, which are the focus of this thesis, the path of the ions are mass-independent and therefore species independent trajectories are assumed below. A short discussion of this effect in magnetic storage rings, where the paths of the ions are mass-dependent, is given in Sec. 3.1.1. Independent of the fields employed for storage (electrostatic or magnetic), the kinetic energy spread of the ions can only be fixed within a certain precision ΔE in an experimental set-up. In the case of identical trajectories the energy uncertainty propagates to the mass determination for a particle of interest according to

$$\Delta m = \frac{\Delta E}{E} m. \tag{3.2}$$

Two different approaches can be employed to reduce this uncertainty of the measured mass. Either, the energy spread of the particles can be minimized, or the path of the particles can be varied to compensate for the energy difference. In storage ring experiments, both approaches have been explored. Electron cooling can be employed [44] to reduce the energy spread within the same species. However, it results in different kinetic energies for ions with different masses. This line of action will not be discussed here any further. The other approach of varying the trajectories of ions with different kinetic energies in order to compensate for the energy spread is explained below.

As outlined in Sec. 2.1.3, the particles' revolution time inside the storage ring becomes independent of their momentum when $\eta = 0$. This condition can be achieved by the right settings of the quadrupole elements inside the device, which focus the particles dependent on their kinetic energy. In the field free regions of the ring, the ions' velocity is dependent on the particles' kinetic energy alone. The resulting difference in propagation time can be compensated in the deflector regions of the device. A schematic drawing of this principle in an electrostatic deflector assuming the storage of anions is shown in Fig. 3.2. The energy dependent orbits of the ions inside the deflector influence the particles' flight time in this region of the ring in two different ways. On the one hand, the trajectory length of the particles increases with increasing kinetic energy. Additionally, apart from the synchronous particle with $\Delta E/E = 0$ all ions fly on trajectories which are displaced from the center of the deflector. Consequentially, particles with larger/smaller kinetic energy are decelerated/accelerated upon entering the fringe field and pass the detector with a smaller/larger velocity then the synchronous particle. They are accelerated/decelerated to their original velocities upon exiting the field. Both effects cause particles with larger/smaller kinetic energy to spend more/less time in

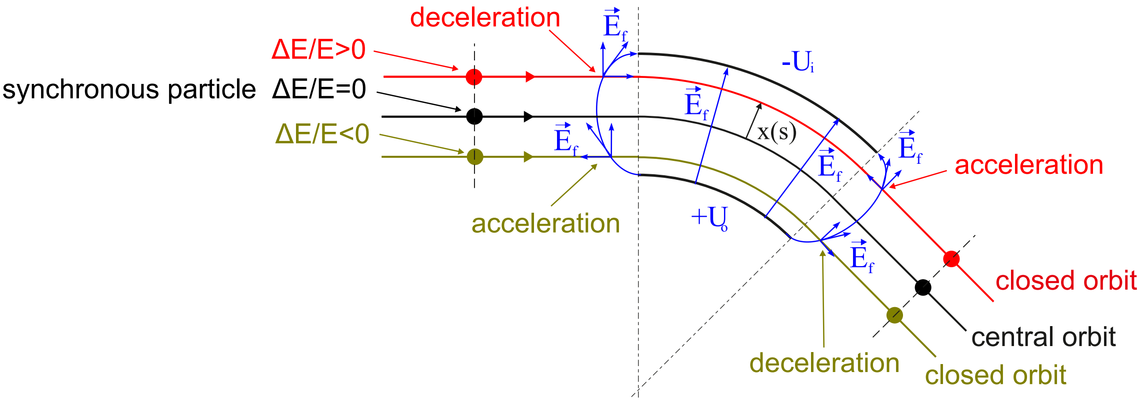

Figure 3.2: Schematic drawing of the trajectories of anions with different kinetic energies through a cylindrical deflector during isochronous operation. The synchronous particle flies through the center of the deflector. Particles with non-zero energy deviations propagate on displaced paths, experiencing an acceleration or deceleration force in the fringe fields of the deflector. As a result, ions with larger/smaller kinetic energy than the synchronous particle have a smaller/larger velocity inside the deflector. Additionally, the different trajectories are also longer/shorter for ions with $\Delta E > 0/\Delta E < 0$. The figure is modified from [34].

the deflector then the synchronous particle. In the isochronous condition, this time difference exactly compensates the one gained in the field-free regions of the ring, which also include betatron oscillations, which will not be discussed here.

The mathematical derivation for the ions' revolution time T and frequency f in an electrostatic storage ring is given in [34] and will not be repeated here. The exact relation between the revolution times/frequencies of a reference of mass m_0 and charge Q_0 compared to a particle with m and Q during isochronous operation is given by

$$\frac{f_0}{f} = \frac{T}{T_0} = \sqrt{\frac{m/Q}{m_0/Q_0}}. \tag{3.3}$$

3.1.1 Comparison of isochronous operation in different devices

Isochronous mass measurements (IMS) are also carried out in magnetic storage rings and MR-ToFs. The underlying principle is the same as in the case of electrostatic storage rings, which is the focus of Sec. 3.1. Optical elements are used to achieve the isochronous conditions in which the revolution time of the ions inside the device becomes independent of their kinetic energy. The main differences to the performance in electrostatic storage rings are outlined below.

IMS was first carried out in magnetic storage rings. The main focus here are radio-nuclei with short lifetimes [30, 54, 55, 58]. The practical implementation of the isochronous mode in magnetic storage rings compared to their electrostatic counterparts is very similar. In both cases, the focusing elements, in this case quadrupole (and optionally also higher-order) magnets are used to define the particles' orbits. However, the two field types, electrostatic and magnetic, result in some differences. In contrast to electrostatic devices, the measurements at magnetic storage rings are predominantly carried out at relativistic energies. This is advantageous for the short lifetimes of the species of interest. Due to the field limitations of optical elements, these velocities cannot be reached in electrostatic devices. Another difference is the acceleration and deceleration effect of the ions in the fringes of the electronic deflectors (see Fig. 3.2). This effect is not present for magnetic storage rings. As a result, larger orbit changes are necessary to compensate for the velocity differences. This can also be seen in the relation between the momentum compaction factor α_p with respect to the slip factor η, which is given for electrostatic storage rings in Eq. (2.9). For magnetic devices, the factor of 1/2 is omitted. Consequentially, the need arises for larger values in the dispersion function compared to electrostatic rings. Additionally, while electrostatic fields deflect dependent on the kinetic-energy-to-charge ratio, an additional momentum (and thus mass) dependence enters for magnetic deflection. As a result, the ions' trajectories are not only kinetic energy but also mass and therefore species dependent. The length of a closed orbit of a particle with mass m, charge q, and velocity v is dependent on the magnetic rigidity $(B\rho)$

$$B\rho = \gamma m v / q, \tag{3.4}$$

where γ is the relativistic Lorentz factor [58]. All magnetic storage rings have a maximum rigidity above which storage is no longer possible. This results in an upper mass limit for a given kinetic energy of the ions not present for electrostatic devices. Additionally, for the simultaneous measurement of multiple species at any setting a magnetic rigidity acceptance range applies, e.g., for the ESR at GSI in isochronous operation this is about $\delta(B\rho)/(B\rho) = 2 \times 10^{-3}$ [58]. Consequentially, only species with similar mass-to-charge-ratios can be investigated at the same time. Furthermore, precise mass measurements typically require the storage of multiple references with known masses simultaneous to the ion species of interest. This is due to the higher-order corrections of the revolution frequency caused by the magnetic rigidity dependent orbit length differences [58]. This is not the case for IMS in electrostatic storage rings, where the orbits are mass independent. Here, the simple relation given by Eq. (3.3) is exact in the isochronous condition and the simultaneous storage of a reference species is not required.

Isochronous operation is also available in MR-ToF devices, where the ions oscillate between electrostatic mirrors (see Fig. 3.1(b)). The isochronous condition can here be reached by manipulating the penetration depth of the particles inside the mirrors, such that the oscillation frequency again becomes independent of the kinetic energy of the particles. In practice, the injection path length as well as the distance to the detector, which is typically outside the trap, has to be taken into account. Therefore, in the device itself, the isochronous condition is often not exactly met as the time focusing is moved to the detection plain [59]. A detailed description of the implementation of IMS in MR-ToF traps can for example be found in [56]. Due to the electrostatic nature of the device, the paths are mass independent as is the case for electrostatic storage rings. Therefore, the calibration difficulties outlined above for magnetic storage rings do not apply. Additionally, this enables the study of species with a much higher mass-to-charge ratio then typically available in magnetic storage ring. As a result, the devices are also used for the study of cluster species [60]. The kinetic energy in these devices is non-relativistic and typically in the range of a few to a few tens of keV, compared to the up to 300 keV in the CSR. Furthermore, the typical ion number that can be stored in the trap simultaneously is in the order of $10^2 - 10^3$ and hence much lower than in storage rings. The ion-ion interactions also differ in the MR-ToF devices. This is due to the oscillating motion of the particles in the trap which results in ion bunches not only overtaking one another but also passing through each other while travelling in opposite directions.

3.2 Description of the isochronous mode in the CSR

The first isochronous operation of the CSR was successfully tested in 2020. These measurements were part of this thesis and are described in detail in [34] and are only shortly summarized below.

Calculations were carried out by Dr. Manfred Grieser to find quadrupole settings which allowed the isochronous operation of the CSR. It was only possible to find a configuration with $\eta \approx 0$ when grouping the 16 quadrupole electrodes of the ring into more than two families. Here, a family describes a set of electrodes where the same absolute voltage is applied. In the standard mode of CSR, which is described in [20], only two families are used. The increase in the number of applied voltages to the quadrupole electrodes reduced the periodicity of the CSR's optical elements from four to two, meaning that now the lattice functions of the ring repeat after half of the circumference. In Fig. 3.3(a), the optical elements of the CSR are shown and numbers mark the assignment of the quadrupole electrodes to the four families. Multiple settings were calculated which met the conditions of isochronous operation. Only the one discussed in [34] was thoroughly investigated and will be shown here. In Fig. 3.3(b), the dispersion function for this isochronous mode is shown. The maximum dispersion was kept below 4.5 m. An additional limiting factor is the smaller vertical beam tube in the electron cooler section of the ring compared to the other straight sections. Therefore, the vertical beta function in section (B), and due to the periodicity of 2 in section (D) as well, is smaller than that in sections (A) and (C) (see Fig. 3.3(b)).

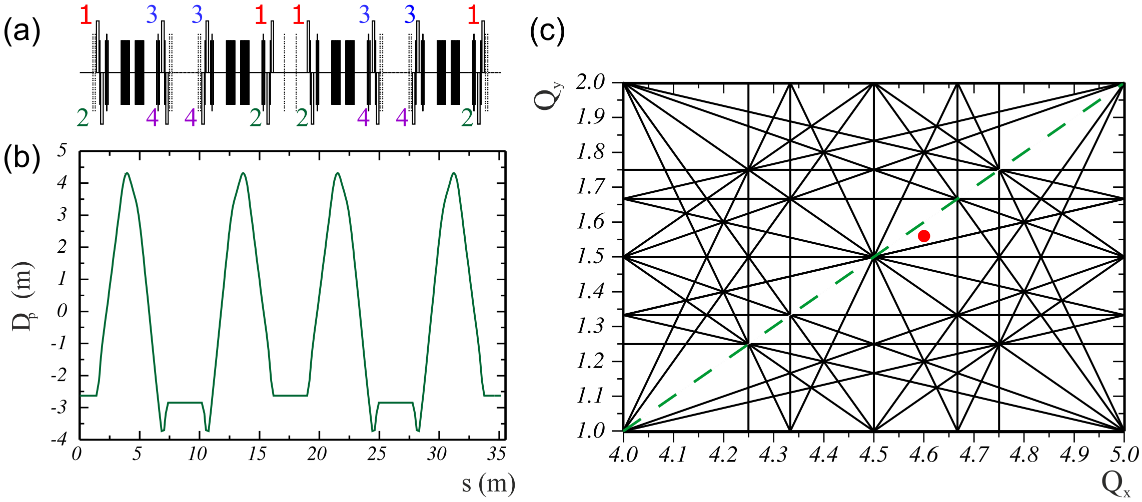

Figure 3.3: Description of the isochronous mode: (a) Optical elements of the CSR (see Fig. 2.3) with the assignment of the quadrupole electrodes to the four families (1-4) (b) Dispersion function D_p plotted versus the co-moving coordinate s. Here, $s = 0\,\mathrm{m}$ is the injection point into the CSR. (c) Working diagram of the CSR, the red dot marks the working point of the isochronous mode. The green dashed line is the coupling resonance $Q_x - Q_y = 3$. The figure is modified from [34].

Figure 3.3(c) shows the working diagram. The working point (see Sec. 2.1.3) is marked in red and is situated at $(Q_x, Q_y) = (4.6, 1.56)$. For the choice of the working point, the space charge field had to be taken into account. It causes a defocusing of the ions in both vertical and horizontal direction, which is called incoherent tune shift. This effect decreases both tunes, Q_x and Q_y, causing the working point to shift within the diagram on a line parallel to the coupling resonance $Q_x - Q_y = 3$ marked in green. The working point was therefore chosen in such a way that a relatively large incoherent tune shift is possible without reaching a resonance. These are drawn as black lines in the working diagram.

In order to experimentally deduce the slip factor, the momentum compaction factor α_p of the ring (see Sec. 2.1.3) was measured using the method described in [61]. For the measurement, voltages of all ion optical elements were scaled by a common factor χ_{scal} and the change in revolution frequency was measured with the Schottky pick-up system (see Sec. 2.2.2) to get the momentum compaction factor

$$\alpha_p = \frac{\Delta f/f}{\Delta \chi_{scal}}. \tag{3.5}$$

The value was measured as $\alpha_p = 0.502$. Using the Eq. (2.9), this gives a slip factor of $\eta = -0.004$. The slightly negative value was chosen to combat the space charge effects for $\eta = 0$. As outlined in Sec. 2.1.3, the isochronous operation causes all particles to stay at their respective positions inside the bunch. Therefore, each ion always experiences the same space charge. The constant, homogeneous energy change causes the loss of the stored particles. Hence, it is advantageous for the ions to change their position inside the bunch. At negative slip factors, the particles start oscillating around the synchronous particle (see Sec. 2.1.3). For very small deviations from the isochronous conditions ($\eta \lesssim 0$), the oscillations are slow and self-bunching is not dominant yet. However, the movement inside the bunch is sufficient to counterbalance the large energy increase/decrease of the ions, therefore allowing mass measurements for longer storage times.

3.3 Mass measurements at the CSR

The first isochronous mass measurement at the CSR was carried out using an ion beam with different anionic carbon-containing molecules of mass $\sim 26\,\mathrm{u}$. Here, it was necessary to verify the presence of the vinylidene anion $\mathrm{CCH_2^-}$ in the stored beam. The underlying experiment investigated the internal lifetime of this molecule is discussed elsewhere [62]. The isochronous measurements during this campaign were part of this thesis and have already been published in [34].

In this section, data from another CSR campaign in the winter of 2023 will be used to discuss the mass measurement methods. Here, an ECR source was filled with a mix of nitrogen and hydrogen gasses. For the data discussed below, a bottle of ^{15}N enriched nitrogen was used (purity: $90 - 95\%$). The underlying objective of these mass measurements was to produce $^{15}\mathrm{N_2H^+}$ for dissociative recombination studies. To this end, a cation beam of mass $m \approx 31\,\mathrm{u}$ was produced on the large ion source platform (see Sec. 2.2.1) and the ions accelerated to 150 keV. The chopper in the injection beamline (see Sec. 2.2) was employed to produce a short ion pulse of about 1 µs width, which was stored in the CSR. Below, the two approaches to perform mass measurements at the CSR are discussed.

3.3.1 Frequency measurements

The Schottky pick-up electrode in section (C) of the CSR (see Sec. 2.2.2) was used to measure the revolution frequency of the ion species stored inside the ring. To this end, a frequency range was chosen, which includes the $11th$ harmonic of the revolution frequencies of the ions inside the CSR ($f \approx 302.75\,\mathrm{kHz}$). The resolution of the spectrum analyser was set to 10 Hz. The measurement was conducted for the first 189 ms after injection, no background subtraction was performed.

The spectrum is shown in Fig. 3.4. Four peaks are visible. Vertical lines mark the maxima of those, defined here as the highest data point of each feature. The resolution of the spectrum analyzer was set to 10 Hz in the measurement. This corresponds to a relative precision of $\sim 3 \times 10^{-5}$ of the measured frequencies. Peak "4",

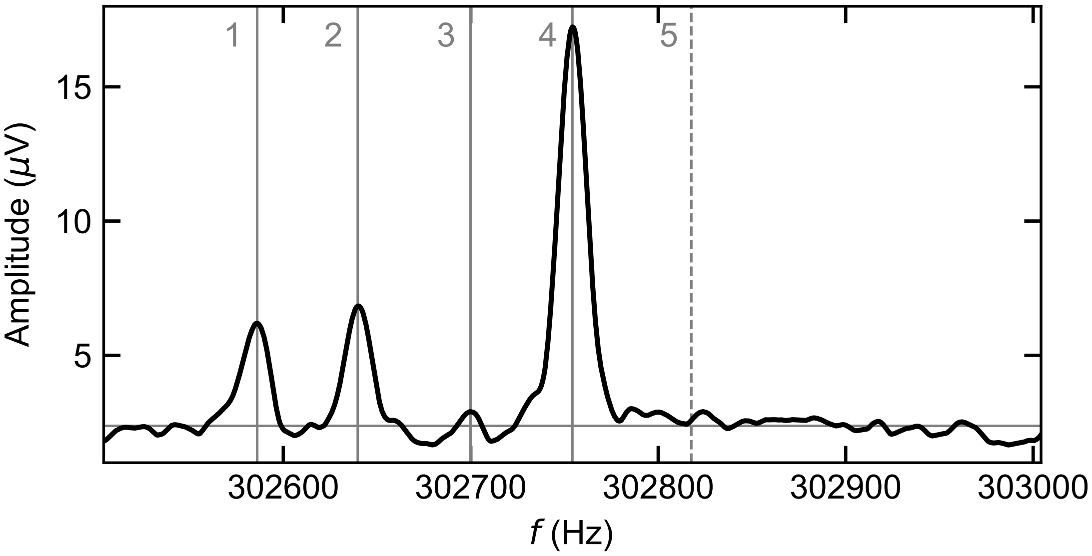

Figure 3.4: Schottky spectrum for the 11*th* harmonic of a mass ≈ 31 u beam at 150 keV. Four distinct peaks are visible. Vertical lines are drawn through the maxima of the peaks. A horizontal line indicates the average background signal. The measured masses and assignment to ion species is given in Tab. 3.1.

which corresponds to $^{15}N_2H^+$, was used as a reference and the other masses determined using Eq. (3.3). The identification of the corresponding species is shown in Tab. 3.1. For the third peak, two possible species could be found. The literature value of the ^{13}C containing ion ($^{12}C^{13}CD_2H^+$) is closer to the measured mass. However, the other species, $^{12}C^{14}NH_5^+$, is the more likely candidate for this peak, due to the low natural abundance of ^{13}C (∼ 1% according to [63]). The relative deviations between the measured mass and both literature values are below the resolution of the measurement, which is in the 10^{-5} range. Overall, the relative precision between measured mass and literature values is in the low 10^{-5} range or below.

This precision of the measurement can be improved by increasing the resolution of the spectrum analyser. A value down to 1 Hz is possible for this device, however, the chosen resolution of 10 Hz is sufficient for the example presented here. Furthermore, the mass resolution can be improved by measuring at higher harmonics of the revolution frequency. However, this will decrease the intensity of the measured peaks in the spectrum and therefore the sensitivity for low abundant contaminants. An attempt to fit Gaussian distributions to the peaks was also undertaken. Here, the fitted maxima deviated from the highest data points of the peaks by a relative value in the range of 10^{-6}. This uncertainty is smaller than the resolution of the data points, which were recorded with 10 Hz steps (relative precision in the 10^{-5}

Table 3.1: Assignment of the peaks shown in Fig. 3.4. Theoretical masses were calculated using the atomic mass values given in [63] and subtracting one electron mass. For the determination of the experimental masses, peak 4 ($^{15}N_2H^+$) was used as a reference. The relative mass differences between the measured masses and the literature values are given. For peak 3, two different species have literature values close to the measured mass. A discussion of their likelihoods is given in the text.

# Peak	Species	m_{theo} (u)	m_{ex} (u)	$\Delta m/m_{\mathrm{ex}}$	I_{rel}
1	$^{14}N^{15}NH_2^+$	31.018 284	31.018 629	1.11×10^{-5}	0.16
2	$^{12}C^{15}NH_4^+$	31.030 860	31.030 960	3.22×10^{-6}	0.19
3	$^{12}C^{14}NH_5^+$	31.041 651	31.041 959	9.92×10^{-6}	0.02
(3)	($^{12}C^{13}CD_2H^+$)	(31.042 190)	(31.041 959)	(7.44×10^{-6})	(0.02)
4	$^{15}N_2H^+$	31.007 494	Ref.	-	0.63
5	$^{15}N^{16}O^+$	30.994 475	-	-	-

range). During the fitting procedure it became apparent, that the recorded peaks are not perfectly described by a Gaussian function. Furthermore, the background signal in the data is not flat (see Fig. 3.4). The small deviation between the fitted maximum and the highest measured value of each peak is therefore at least in parts caused by the imperfect description of the measured features by the underlying fit function. Therefore, a Gaussian fit was not used to identify the peak positions here.

Furthermore, relative intensities I_{rel} of the four peaks visible in Fig. 3.4 are given in Tab. 3.1. These were calculated by subtracting the average background, indicated with a horizontal grey line in the figure, from the maximum values of the peak. The obtained value for each mass was then divided by the sum over all corrected intensities. Due to the non-constant background signal in the spectrum and the asymmetric peak shape, I_{rel} is only a rough estimation. From the measurement discussed here, a sensitivity for this method can be estimated. The minimal relative beam fraction required to resolve a contaminant in the frequency spectrum is roughly 1%. A dashed vertical line with the number "5" indicates the position of $^{15}N^{16}O^+$, which could be detected with the Time-of-Flight method discussed in the next Subsection 3.3.2. The sensitivity of the Schottky was not sufficient to identify this species in the ring. In order to improve the sensitivity, it is possible to separately measure the background signal and subtract this from the measured spectrum, which was not done in the measurement presented here.

3.3.2 Time-of-Flight (ToF) measurement

Next to the revolution frequency, the revolution time of the ions inside the device can also be used to calculate the masses. To this end, the movable single particle detector COMPACT in corner 3 of the CSR is employed (see Sec. 2.2.3). The device can be placed at different positions perpendicular to the stored ion beam's trajectory. To perform the Time-of-Flight (ToF) measurements, two detector positions are commonly used. One is the neutral position. Here, the detector is placed on the path of neutral reaction products created in section (B) of the ring. These particles are continuously created by collisions of the stored ions with residual gas, but can also be induced, e.g., by photo-detachment or -dissociation via a laser. The second detector position is the so called "halo position". Here, COMPACT is placed very closely to the stored ion beam's trajectory and collects particles with very large betatron oscillations. These ions form a halo-like structure in the beam profile in the plane perpendicular to the orbit path.

The two positions come with different advantages and disadvantages. In the neutral position only reaction products are collected. Therefore, when observing the residual gas induced events at low pressure inside the CSR (e.g., during cryogenic operation), the required measurement time can increase to hours in order to reach the high number of counts required to identify low abundance species. Furthermore, the abundances of the different species can not be directly inferred by the count rate on the detector, since it is convoluted with the species specific cross-section of the underlying reaction process. However, this can also be used as an advantage. In some cases it is possible to enhance the detection efficiency of specific species by selective destruction, e.g., via laser-dissociation or -detachment (see [34]). This is not possible in the halo position, where stored ions are collected directly. Though in this positions it is easier to estimate the abundances of the different species by the detector count rate. Furthermore, the number of events is independent of the residual gas pressure inside the ring. However, the method can only be employed for beams which have a significant amount of ions in the halo. For low emittance beams, this detector position cannot be used. In this case, the detector has to be moved too far into the stored beam to collect particles. As a result, the count rate on the detector is immediately very high causing saturation effects. Additionally, the majority of ions are destroyed via detection at very short time scales insufficient for mass measurements.

The measurement and data analysis for the ToF method is the same regardless of detector position. When an ion pulse of a specific species passes section (B) of the CSR, COMPACT can either collect neutral reaction products or ions in the halo of the stored beam. This causes a periodic increase of the detector countrate, which can be averaged over many injections to acquire good statistics. In order to read out this signal, a 2D ToF histogram can be created. The corresponding figure for the $^{15}N_2H^+$ beamtime with COMPACT on neutral position is shown in Fig. 3.5.

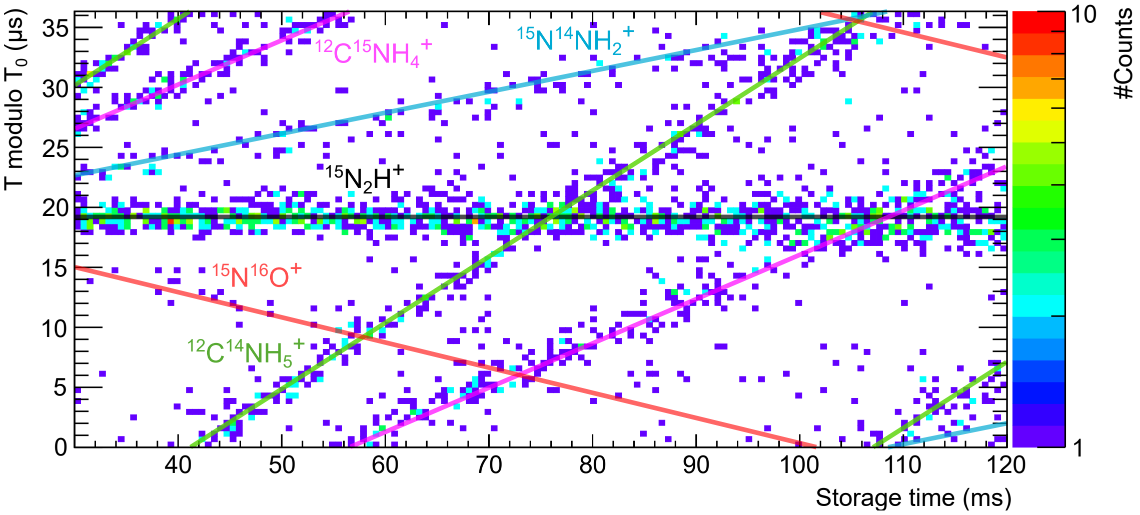

Figure 3.5: ToF histogram for $m \approx 31\,\mathrm{u}$ cations with COMPACT at the neutral position. $^{15}N_2H^+$ was chosen as reference. Lines for four contaminants visible in the spectrum are indicated. The theoretical masses used to calculate their slopes are given in Tab. 3.1. A description of how to generate such a plot is given in the text.

Here, the arrival time T of the counts on the detector with respect to the injection time modulo the revolution time of the reference ion T_0 is plotted on the y-axis. The storage time is plotted on the x-axis. By displaying the data like this, counts that correspond to a species that has a revolution time which matches T_0 appear on a horizontal line in the plot. The y-axis position is given by the initial phase between the start of the data acquisition and the first time the ions pass section (B) of the ring. In Fig. 3.5, $^{15}N_2H^+$ was chosen as the reference. Counts corresponding to species with different revolution times than the reference appear on slopes. Their inclination is proportional to the revolution time difference between the species and the reference and can be calculated using Eq. (3.3). A negative slope indicates a mass lighter than the reference. Here, the ions get further in front of the reference with each revolution. The opposite is the case for positive inclinations, which correspond to heavier species.

The three heavier contaminants $^{15}N^{14}NH_2^+$, $^{12}C^{15}NH_4^+$ and $^{12}C^{14}NH_5^+$, which were already observed in the frequency spectrum (see Fig. 3.4), are clearly visible in Fig. 3.5. Coloured lines mark the calculated positions using the literature values given in Tab. 3.1, which agree well with the measured count rates. An additional line is barely visible and corresponds to the $^{15}N^{16}O^+$ cation. Here, the slope has an opposite inclination, because this species is lighter than the reference. It is difficult to estimate the relative abundances of the different molecular isobars from the figure. First of all, the measured count rate is given by a convolution of the abundances with the destruction cross-section of the species. Additionally, the mass lines cross at different storage times, at which it is impossible to assign the individual counts to a certain species. Therefore, the ToF measurements have so far been used for qualitative identification of contaminants.

A slight bend of the reference signal downwards is visible in the last $\sim 20\,\mathrm{ms}$ of storage time shown in Fig. 3.5. This can be explained by looking at the injection process. In order to inject an ion bunch, the 6° degree deflector in Corner 1 in front of Section (A) (see Fig. 2.3) is switched off. To ensure storage of the ions, this deflector has to be put back on voltage before the injected particles reach it again after one revolution. Therefore, a high-voltage (Behlke) switch is connected to this electrode. It can restore the deflector to almost all of its intended voltage in less than 100 ns. At this setting, the ions are already stored in the ring. The deflector reaches its final voltage (up to $\sim 20\,\mathrm{kV}$ at 300 keV beam energy) after $\sim 100\,\mathrm{ms}$. At this point in time, the slightly stronger deflection causes the ions to fly on smaller orbits than before, resulting in smaller revolution times. Therefore, the signal bends downwards in the ToF figure.

3.3.3 Discussion and comparison of the two methods

The two different mass measurement methods employing the Schottky pick-up and the detector can be viewed as complementary procedures. The high sensitivity of the ToF method provides the opportunity to detect species that have very low abundances. In the example of the $m \approx 31\,\mathrm{u}$ beamtime, this can be observed for the $^{15}\mathrm{N}^{16}\mathrm{O}^{+}$ molecular isobar, which is only visible in the ToF plot. Using the measurement discussed in [34], which has better statistics than the one shown in Fig. 3.5, a sensitivity of 1 : 4600 could be reached. For the frequency measurement this value is lower and the detection limit currently estimated at an abundance of $\sim 1\%$. This observation is also supported by the measurement discussed in Sec. 3.3.1.

Assuming a sufficient abundance of a contaminant in order to be visible for both mass measurement methods, the frequency approach to determine the mass of the species is more accurate and also more straight forward than the one using the revolution time of the ions. The Schottky spectrum enables the determination of masses via the peak positions, which has a relative accuracy in the low 10^{-5} to 10^{-6} region. This value could further be improved by measuring higher harmonics of the revolution frequency of the ions. This will however reduce the sensitivity to low abundant contaminants for this method. The determination of measured masses to the features visible in the ToF spectra is less obvious and was recently the subject of the Bachelor thesis of Tobias Orlemann [64]. Here, the uncertainty of the masses extracted from the detector data was estimate to lie in the 10^{-4} range.

Next to the molecular composition, the relative abundances are also crucial information for the measurements performed in the CSR. This can entail the number of ions of one species in relation to the total number of particles in the beam. For sufficiently abundant species, this is best determined with the Schottky pick-up measurement. For contaminants that make up less then $\sim 1\%$ of the beam, the halo position of the COMPACT detector can be employed to collect ions cross-section independent and perform a rough abundance estimation. However, sometimes it is necessary to understand the species relative contribution to the rate of a reaction process. This was for example the case for the CCH_2^- measurement discussed in [34, 62]. Here, the photo-detachment of the different beam components for a certain wavelength had to be determined. This can only be accomplished with the ToF method and the detector at neutral position, while the halo position and the frequency measurement are not sensitive to reaction processes.

3.4 First tests to clean the beam of contaminants inside the CSR

With the isochronous operation of CSR, described and characterized in Sec. 3.2 and 3.3, the identification of ion species in the stored beam is now possible even for contaminants with small abundances or small relative mass deviations. In order to carry out contaminant-free experiments in future measurements, it is not only necessary to know the composition of the ion beam, but also to remove unwanted species. In a first approach, the ion source settings can be adjusted. The beam composition can then be measured in the CSR with the isochronous mode. However, it is not always possible to remove all contaminants with this approach, necessitating in-ring methods to remove species. Two different approaches to clean the stored beam of contaminants during isochronous operation have been qualitatively tested during four days in July 2021. Details of this measurement campaign are given in Sec. 3.4.1. One method uses the rf system of the ring, while for the other a fast switch was attached to one of the vertical deflectors. They will be presented in Sec. 3.4.2 and 3.4.3, respectively.

Due to the short beam lifetime in the isochronous mode (see Sec. 3.2), reaction studies, which typically require lifetimes in the order of hundreds of seconds or above, are not feasible with these ring settings. Furthermore, a change of mode from isochronous operation to one of the modes used for reaction studies cannot be carried out while a beam is stored. On the one hand, the ring has very different working points in these modes and several resonances have to be crossed when switching between two of them, which would result in a loss of the stored beam (see Sec. 2.1.2). On the other hand, the parities of the applied voltages on some of the quadrupole electrodes are opposite for the isochronous operation compared to the other modes. Switching the parity of the quadrupole electrodes will also lead to a loss of the stored beam. Therefore, the isochronous mode can only be used as a diagnostic tool to identify all species produced by the source. For contaminant-

Table 3.2: List of ion species visible in the ToF plots recorded during the beam cleaning tests. For total nuclei numbers A, where more than one ion is expected, the species with the higher natural abundance is listed first. The molecular isobar, its mass as well as the relative mass difference of the two are also given. Masses are derived using the atomic masses as well as the electron mass taken from [63].

A (u)	Species	m_1 (u)	Isobars	m_2 (u)	$\frac{\Delta m}{m_1}$
194	$^{182}\mathrm{W}^{12}\mathrm{C}^-$	193.948 75	-	-	-
195	$^{183}\mathrm{W}^{12}\mathrm{C}^-$	194.95077	$^{182}\mathrm{W}^{13}\mathrm{C}^-$	194.952 11	6.85e-6
196	$^{184}\mathrm{W}^{12}\mathrm{C}^-$	195.95148	$^{183}\mathrm{W}^{13}\mathrm{C}^-$	195.954 13	1.35e-5
197	$^{197}\mathrm{Au}^-$	196.967 01	-	-	-

free measurements, the beam has to be cleaned in non-isochronous operation, where often the different species can no longer be distinguished. Sec. 3.4.4 will show the very first attempts to remove contaminants from a beam stored in non-isochronous operation.

3.4.1 Beam time parameters

For the beam cleaning tests, the tungsten carbin anion WC$^-$ was chosen as a system and produced in a MISS (see Sec. 2.2.1). Both tungsten and carbon have multiple stable isotopes, ^{182}W, ^{183}W, ^{184}W, ^{186}W for tungsten and ^{12}C and ^{13}C for carbon. Consequentially, WC$^-$ has multiple isotopologues and two molecular isobars at masses 195 u and 196 u. They are listed in table 3.2. A kinetic energy of 150 keV was chosen for the ions, the maximum energy at which the voltage stabilization on the high-voltage platform could have been used at the time.

At the time of the measurement, the CSR was operated at room-temperature. Therefore, the residual gas pressure was in the order of 10^{-11} mbar (compared to $\sim 10^{-14}$ mbar at 4 K). This considerably increased the number of events induced by residual gas collisions compared to cryogenic operation and limited the beam lifetime inside the device. For the isochronous operation, however, the reduced storage time was not a problem due to the short beam lifetime caused by space charge effects (see Sec. 3.2).

An exemplary ToF spectrum of the ion beam composition for the beam cleaning tests is shown in Fig. 3.6. It was not possible to resolve the molecular isobars in this measurement, due to the unfavourable combination of small relative mass difference and low abundance of the second species. However, this does not have an effect on the beam cleaning tests discussed below.

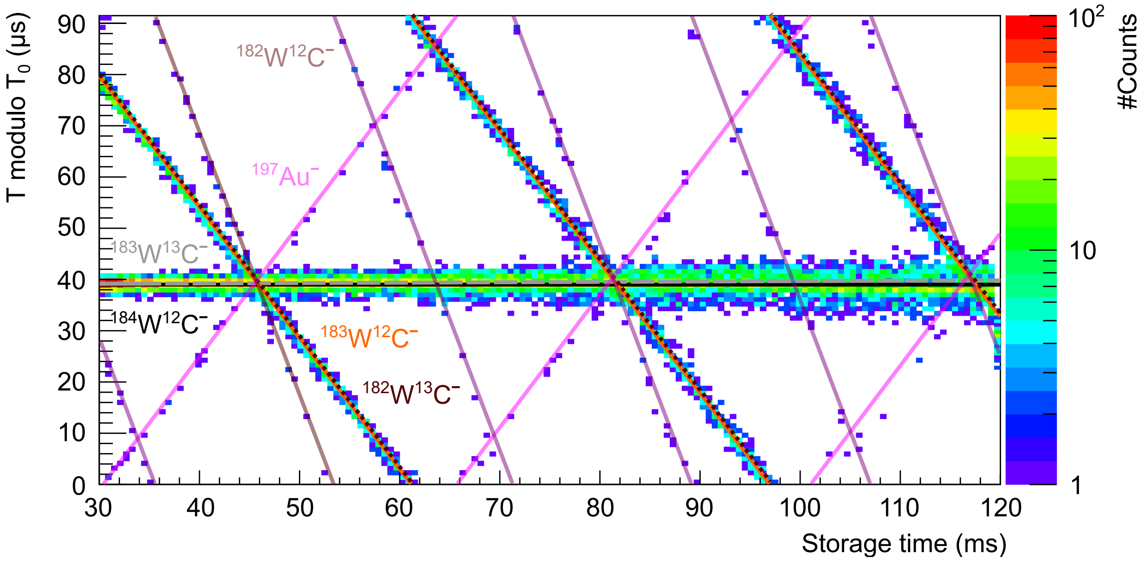

Figure 3.6: ToF plot for the beam used for the first in-ring contamination removal tests. Coloured lines indicate the theoretical positions for different ion species. The literature values of the masses are given in Tab. 3.2. For species with 195 and 196 nucleons two molecular isobars of WC^- exist. While the theoretical lines are indicated for all species in the plot, the isobars cannot be distinguished in the measurement.

3.4.2 rf excitation in the isochronous mode

In a first attempt to remove one ion specie from the stored beam without affecting the others, the ring's rf system was used. As already discussed in Sec. 2.2.2, a sinus shaped signal can be applied to a drift inside the ring. Ions passing the tube will experience either a gain or loss in kinetic energy, depending on the phase of the potential's oscillation. In isochronous operation where $\eta = 0$, this change in momentum will have no influence on the particles' revolution frequency inside the device (see Sec. 2.1.3). If a harmonic of one of the species' revolution frequencies is applied to the rf system, these ions will reach the drift tube in the same phase of the oscillation in their next revolution. Consequentially, they will experience the same force, leading to a linear change in kinetic energy, either increase or decrease depending on the phase. This process will continue until the particles reach the energy acceptance of the ring and are lost. If an rf signal is applied that does not match an ion's revolution frequency, or harmonics thereof, the particle will experience a different force each time it passes the drift tube. As a result, the ion's kinetic energy will perform a random walk, which will not result in a loss of the particle on short timescales.

For the test measurement shown in Fig. 3.7, a signal corresponding to the $20th$ harmonic of the revolution frequency of the dominant species in the beam (218 624 Hz

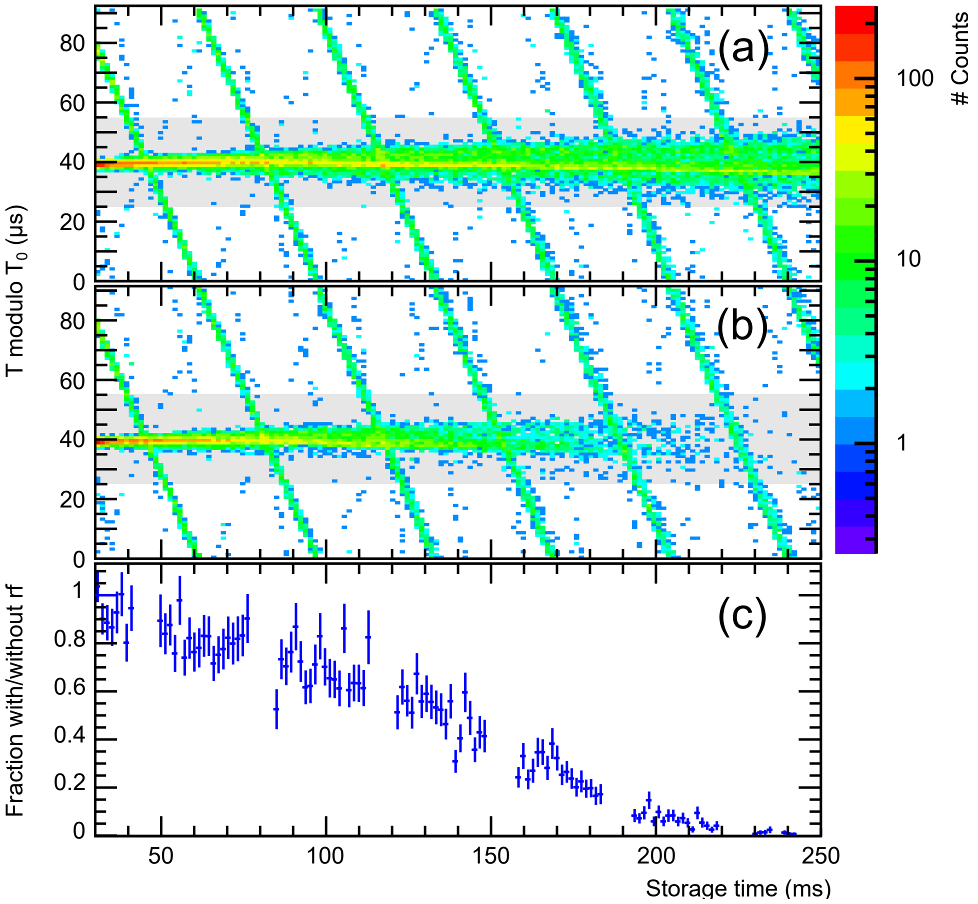

Figure 3.7: Beam cleaning through rf excitation in the isochronous mode: ToF flight plots (a) without rf excitation, (b) with rf excitation on the 20*th* harmonic of the main (horizontal) component; (c) Fraction of counts with and without rf excitation on the main component. The time windows where the most abundant contaminant overlaps with the main component is cut out of the data.

for $m \approx 195.95\,\mathrm{u}$) was applied to the rf system. The high harmonic was necessary, because the rf amplifier operates in a frequency range around $200 - 300\,\mathrm{kHz}$. Sub-figures (a) and (b) show the ToF plots without and with the signal applied, respectively. In the latter, a decrease of the main component signal, marked with a grey box in the plots, is visible. The fraction of the main component signal with and without rf applied versus storage time is shown in panel (c) of Fig. 3.7. Here, the time windows where the dominant contaminant crosses the main component is not plotted to avoid a distortion of the fraction due to fluctuating relative populations of the different species. After $\sim 220\,\mathrm{ms}$ the main component is excited out of the ring's acceptance. The other beam components shown in Fig. 3.7 are not

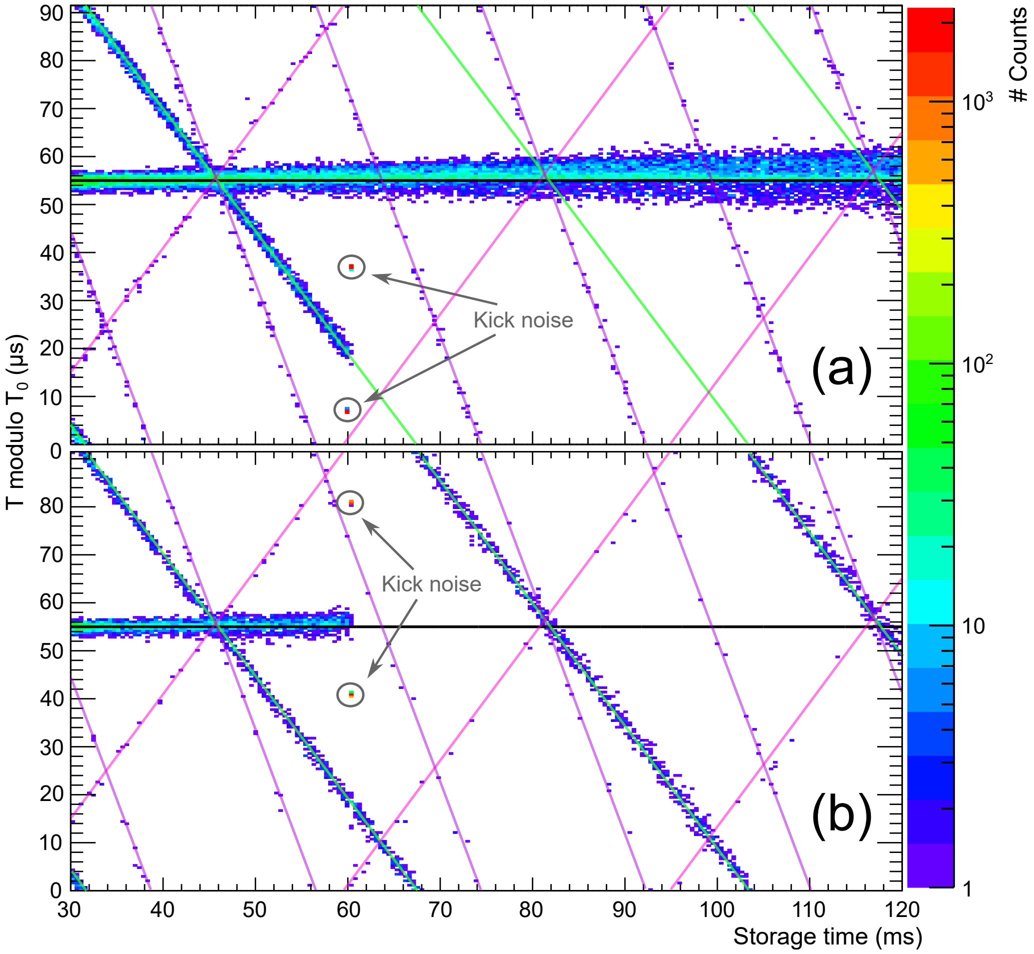

Figure 3.8: Beam cleaning by deflector kick during isochronous mode. Panels (a) and (b) show the deflection of two contaminants (marked in green and pink) and the main component of the beam, respectively.

significantly affected by the applied rf signal.

3.4.3 Deflector kick in the isochronous mode

Another method to selectively remove species tested in the July 2021 test beamtime was the so called "deflector kick". For this purpose, a fast switch was connected to one of the vertical deflectors in corner 3 of the CSR (see Fig. 2.3). With this device, a short pulse can be applied to the deflector. Ions flying in the optical element at that time are deflected off their closed orbit and lost. During the isochronous operation, each ion specie stays together in a pulse on timescales long enough for the different masses to separate completely in the ring. This enables the selective deflection of only one or a subgroup of species.

In Fig. 3.8 two ToF flight plots are shown for measurements where a single deflector kick was employed. In both cases, the procedure is carried out at about 60 ms of storage time. The electronic noise in the signal due to the deflector kick, marking the beginning and the end of the applied pulse, is visible in the ToF plot. The location of this noise in the plot cannot be directly used to infer which components are kicked, since the deflector and the detector are not located exactly at the same position inside the CSR. As a result, mass lines running in between the noise signals are not necessary lost. In panel (a) the pulse on the deflector was timed in such a way that two contaminants were kicked out of the ring's acceptance. These correspond to $m \approx 194.95\,\mathrm{u}$ (green line) and $m \approx 196.97\,\mathrm{u}$ (pink line). In panel (b) the main component ($m \approx 195.95\,\mathrm{u}$, black line) was removed. In both cases, the other components are undisturbed by the kick. This method is much faster than the one introduced in Sec. 3.4.2, however it requires the physical separation of the different ion species in the CSR.

3.4.4 Contaminant removal in non-isochronous operation

In a first step towards cleaning molecular isobar contaminants from the stored beam in non-isochronous operation, initial tests were performed with the WC^- beam. Due to the positive slip factor of the employed mode, the injected ion pulse disperses much faster than in the isochronous mode, as can be seen in the ToF plot in Fig. 3.9(a). Due to the relatively large mass difference of the beam components ($\Delta m \geq 1\,\mathrm{u}$), the separation between the different species is still faster than the increase of the ion pulse width. However, at about 120 ms the different components are mostly indistinguishable (compare to figures in the sections above).

The aim of this test was to remove all contaminants from the beam such that only the main component ($m \approx 195.95\,\mathrm{u}$) is stored. In a first step, the rf system (see Sec. 2.2.2) was employed to only bunch the desired specie. In non-isochronous operation, the kinetic energy change of the ions induced by the changing potential of the drift tube leads to a change of the particles' revolution time. If a harmonic of a specie's revolution frequency is applied to the rf system, these ions get trapped inside a bucket. The number of buckets is given by the harmonic applied. Fig. 3.9(b) shows the ToF plot for a measurement where the $20th$ harmonic of the main component's revolution frequency was applied to the rf system. Here, the rf system is ramped up 2 ms after injection and the ion specie of interest is captured in two buckets out of twenty. This is only possible due to the very narrow injection pulse of $\sim 2\,\mu\mathrm{s}$ employed here. The contaminants are not trapped by the rf and propagate outside the buckets in the ring.

After the successful spacial confinement of the desired ion specie by the rf system, the deflector kick (see Sec. 3.4.3) can be used to remove all other components from the stored beam. A first attempt to do so using one kick can be in Fig. 3.9(c). The duration of the pulse on the deflector was chosen in such a way that only the

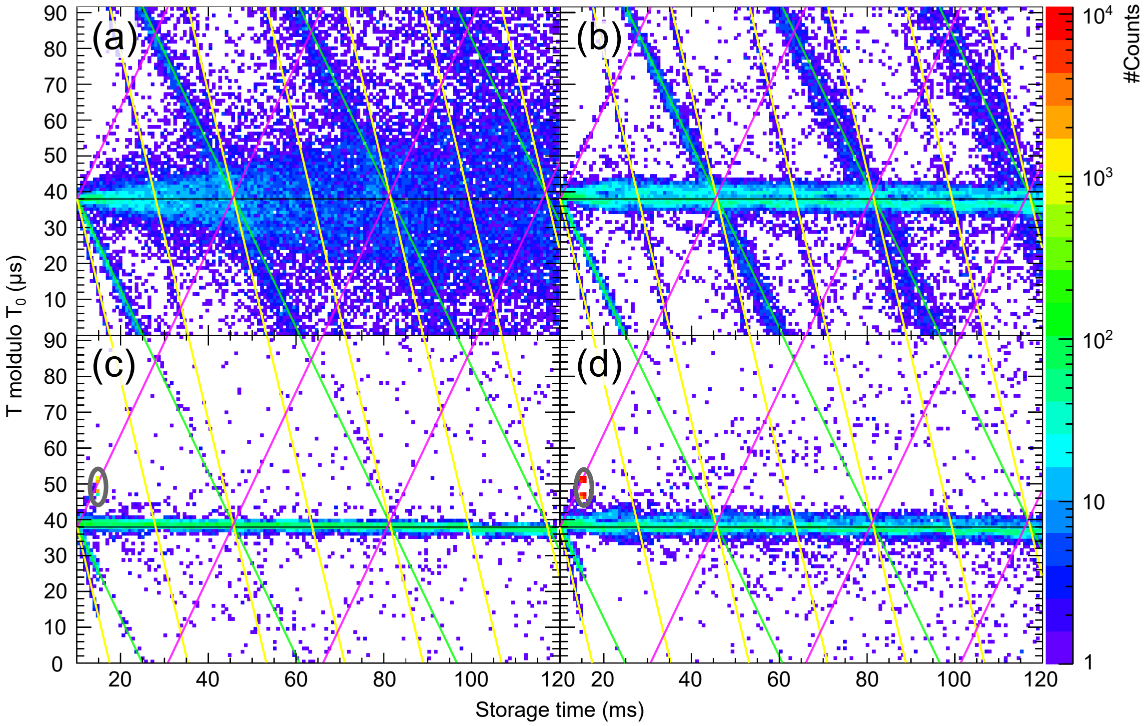

Figure 3.9: ToF plots for non-isochronous operation: (a) No beam manipulation applied, (b)-(d) rf bunching of the main component, (c) additional single deflector kick to remove all contaminants, (d) 10 consecutive deflector kicks to remove all contaminants. Grey ellipses in panels (c) and (d) indicate the noise of the kicks.

two filled buckets were not deflected. When comparing the vertical width of the ion species of interest in Sub-Fig. 3.9 (b) and (c), it becomes clear that one of the filled buckets was at least partially deflected as well, reducing the number of desired ions in the ring. Furthermore, residues of the main contaminant ($m \approx 194.95\,\mathrm{u}$, green line) are still visible after the deflector kick was performed. In order to tackle these two issues, the timing of the kick was adjusted with respect to the buckets and the kick was performed for 10 consecutive revolutions of the species of interest. The resulting ToF plot is shown in Fig. 3.9(d). The structure of both filled buckets is now visible again and no significant accumulation of counts on any of the contamination mass lines can be observed.

The large mass separation of the ion species used for these initial tests is an ideal scenario for the contaminant removal methods. The closer two beam components are in mass, the more difficult it becomes to only manipulate one specie while leaving the other undisturbed. Further tests are still ongoing on the minimum separation in revolution frequencies of two types of particles before the rf system will trap not only the ions of interest but also a significant fraction of the contaminant. Additionally, preliminary tests have been carried out for a different beam cleaning method using the electron cooler.

3.5 Discussion and Outlook

This chapter discussed the implementation of the first isochronous mass measurements in the CSR. Coincidentally, these were also the first isochronous mass measurements in any electrostatic storage ring. They were motivated by the need to reliably identify contaminants, predominantly molecular isobars, in the ion beams stored inside the CSR. To this end, a relative mass precision of $\sim 10^{-5}$ as well as a sensitivity to relative abundances well below 10^{-2} are necessary.

The set-up of the CSR in the isochronous condition was shortly summarized based on the detailed description given in [34]. Afterwards, the two mass measurement methods were discussed. One uses the Schottky pick-up as well as a spectrum analyser to record a frequency spectrum of the stored ions. Here, a relative mass precision of 10^{-5} and below was reached. However, the sensitivity for low abundant contaminants is only about 1% of the total beam. The other method employed the COMPACT detector to record a ToF spectrum. Here, two different detector positions can be employed, the neutral and the halo position. Their advantages and disadvantages were discussed. The overall method was found to have a much higher sensitivity to low abundant species (below 10^{-3}), but the masses of the ions could be determined less precisely than with the frequency method. Furthermore, the ToF procedure offers the possibility for reaction rate specific measurements, which is not possible with the frequency spectrum approach. Therefore, the two measurement procedures can be seen as complementary methods.

For the merged beam experiments at the CSR it is not always sufficient to only know the molecular composition of the ion beam. This is especially true in the case of reaction processes where the rate coefficients of the contaminants are unknown or the rate of interest is much lower than those of the contaminations. First tests for beam cleaning methods have been carried in the course of this thesis. For this purpose both rf-excitation and a fast switch on one of the ring's deflectors were employed. The methods were very effective during the isochronous operation of the CSR. Also first attempts of beam cleaning in non-isochronous operation have been carried out.

The performance of the isochronous operation of the CSR is still being investigated beyond this thesis. One focus is the debunching and rebunching effects at slightly different slip factors around zero and varying numbers of ions in the ring. The influence of this effect on the precision of the measured masses is not fully understood so far. Furthermore, an extraction of a stored beam on a detector, for example in the extraction section of the CSR (see Fig. 2.2 and [28]), is being considered. This would enable measurements with only tens to hundreds of ions stored inside the ring, which is below the detection threshold of the frequency and ToF measurements discussed in Sec. 3.3. At such densities in the beam, the space charge effects become negligible and the mass precision can be improved. Additionally, investigations into more effective beam cleaning techniques during non-isochronous operation are still ongoing. Due to the large momentum acceptance of the ring, it is not always possible to separate different species either in space or in the frequency domain in non-isochronous modes. This makes beam cleaning efforts considerably more complicated. Different options are currently being explored, which would enable the manipulation of the ions' momenta inside the ring. Here, the idea is to use either the electron cooler or the ring's rf system to change the ions' kinetic energy in such a way, that the contaminants' momenta reach the acceptance of the ring. Ideally, this would lead to a significant loss of these species while the ions of interest are still predominantly stored in the CSR.

4 Modelling the decay of highly-excited anionic carbon dimers

Molecular systems offer a multitude of excited states through their different degrees of freedom. The interplay of electronic, vibrational and rotation excitation can result in a variety of coupling mechanisms which allow the decay of excited molecules. This can either happen radiatively via the emittance of photons, through fragmentation, or by the ejection of electrons. At sufficiently high internal excitation, multiple of these channels might be available simultaneously and are in competition with each other. The rates for the different mechanisms then define the decay process of the system. If the rate of one channel is significantly larger than the ones of the other processes, the molecule will predominantly decay through this channel. The population of this state is then depleted by this process and decays through the other channels become negligent. Here, radiative relaxation of high internal excitations stabilises the system and can result in internal excitation below the thresholds of the two destructive mechanisms, fragmentation and electron detachment. On the other hand, these two processes result in the loss of the molecule in its initial configuration. The detailed study of these mechanisms becomes increasingly difficult with increasing complexity of the system, given predominantly by the number of nuclei and electrons available in the molecule.

The anionic carbon dimer C_2^- is as an excellent model system to investigate a number of different decay channels. Its simplicity in structure, due to its diatomic nature, enables the explicit calculation of a wide range of ro-vibronic states with reasonable computational effort. Additionally, despite the low structural complexity, C_2^- is known to have multiple bound states with dipole allowed transitions [12]. In fact, it was the first negative molecule for which bound excited states were discovered [65]. This sets it apart from similar homonuclear anionic dimers, which typically only have one bound electronic state [2]. This distinction is important for the study of radiative de-excitation, which is strongly suppressed in the absence of dipole-allowed electronic transitions due to the lack of a dipole moment in this type of symmetric systems. Over the last decades, a large number of both experimental and theoretical studies have been carried out on C_2^- [12, 13, 14, 15, 16, 17, 19, 65, 66, 67, 68, 69, 70, 71, 72], investigating the different excitation and decay channels of the dimer. Despite their detailed consideration of the system, open questions remain. Perhaps the most prominent example of this is the auto-detachment (AD), the spontaneous emission of the excess electron, of highly-excited anionic carbon dimers on a millisecond

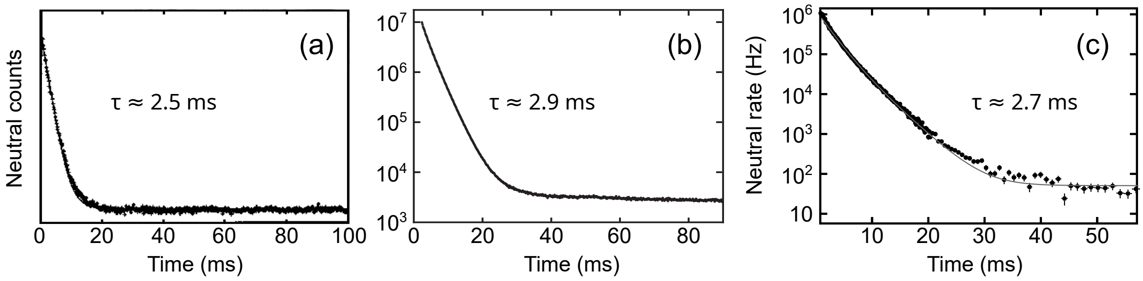

Figure 4.1: Millisecond auto-decay of C_2^- measured at different storage ring facilities. (a) Neutral product yield measured at the ASTRID storage ring in Aarhus, Denmark in 1998. The figure is modified from [16]. No y-scale values were given in the publication. (b) Neutral counts stemming from auto-decay measured at the RICE storage ring in Wako, Japan in 2020. The plot is modified from [19]. (c) Neutral product rate stemming from the auto-decay measured at the CSR in 2015.

timescale.

$$\left(C_2^-\right)^* \rightarrow C_2 + e^- \qquad \text{(AD)} \qquad (4.1)$$

In experiments which observed this signal, C_2^- was produced in a sputter source and injected into a storage ring or an electrostatic trap. A small fraction of the beam decayed by spontaneous detachment without additional excitation, e.g., by laser. In Fig. 4.1 the neutral signals for some of these experiments are shown. Here, the decays were measured at different storage rings over the last three decades. Fig. 4.1(a) shows a measurement from 1998 performed at the ASTRID facility, published in [16]. In sub-figure (b), the data from the RICE storage ring published in 2020 [19] is displayed. Both studies observed a strong signal with an approximately exponential dependence over at least the first $\sim 20\,\text{ms}$ of storage. After this time, the measured signals level off into a horizontal background (see Fig. 4.1(a) and (b)), which is mostly likely caused by collisions of the stored ions with residual gas particles. Fits to the data yielded very similar lifetimes for the nearly-exponential component in the range of $2.5 - 2.9\,\text{ms}$. Additional measurements at other facilities not shown in Fig. 4.1 furthermore report lifetimes of 3 ms [18] or "a few milliseconds" [17]. As will be discussed later in this chapter, the description of this AD signal by a single exponent is a good approximation but does not fully reflect the underlying superposition of many states with very similar lifetimes causing the signal. Therefore, the lifetime obtained by fitting only a single component is also dependent on parameters like the height of the background signal and the time after injection at which the measurement begins. Hence, the slightly varying lifetimes reported for the different storage ring facilities are not necessarily indicative for different processes.

Measurements of the destructive auto-decay of C_2^- were furthermore carried out at the CSR facility. Here, a sputter source was employed as well and the signal of the neutral decay products was recorded. A zoom into the first $\sim 60\,\mathrm{ms}$ of this signal is shown in Fig. 4.1(c). In this time range, the curve displays a nearly exponential dependency with a lifetime of $\sim 2.7\,\mathrm{ms}$. Due to the low residual gas density in the CSR (see Sec. 2.2), the signal does not level off into a horizontal background as was observed at other facilities. Instead, the curve displays a power-law dependency for storage times $\gtrsim 40\,\mathrm{ms}$, which is not visible in the zoom presented in Fig. 4.1(c) and will be discussed in Sec. 4.1. Next to the neutral reaction products, the measurement at the CSR also included a separate data set for the charged fragment (C^-) yield from spontaneous decay of C_2^-. This signal displays the same power-law dependency as was observed in the neutral curve for storage times $\gtrsim 40\,\mathrm{ms}$. The C^- product is created by auto-fragmentation (AF) of highly excited dimer anions.

$$\left(\mathrm{C}_2^-\right)^* \rightarrow \mathrm{C} + \mathrm{C}^- \qquad \text{(AF)} \qquad (4.2)$$

A neutral carbon atom as well as the charged C^- are produced during this process. As a result, this reaction is also visible on the neutral count rate which includes the AD signal. AF is found to be much weaker than AD at the first $\sim 40\,\mathrm{ms}$ but dominants at later storage times. The power-law dependency displayed by the signal has previously been observed for the AF of other anionic homo-nuclear dimer systems [5]. These previous studies were carried out on homo-nuclear diatomic molecules without bound electronically excited states (Cu_2^- and Ag_2^-). In contrast to C_2^-, radiative relaxation was therefore not available as a competing decay channel. Furthermore, no signal AD was observed for these two species.

This chapter is structured as follows: First, the auto-decay measurements carried out at the CSR facility are presented in Sec. 4.1. In the following Secs. 4.2 - 4.5, the decay channels of ro-vibrational excitations in the different electronic states of C_2^- are investigated in order to identify the origin for the observed AF and AD signals. To this end, potential curves for the lowest four anionic and lowest two neutral states of the carbon dimer are presented and discussed in Sec. 4.2. Additionally, the effect of rotational excitation on the potentials is investigated in this section.

Due to the large number of electronic states, radiative decay is possible in almost all ro-vibronic excitations of the dimer. As a result, this channel acts as a competing, stabilising process to the destructive auto-decay channels. For the system at hand, both the dipole-allowed transitions between the three bound doublet states of the system, as well as dipole-forbidden transitions from the fourth electronic state with quartet symmetry to the doublet ground state are investigated in Sec. 4.3. Previous studies discussed in Sec. 4.3.1 have found that levels in the second excited state of the anion, $\mathrm{B}^2\Sigma_u^+$, exhibit lifetimes of tens of nanoseconds and below for the radiative decay (see Sec. 4.3.1). As a result, the levels are not populated long enough to contribute to the signals measured in the experiment. Due to the path from the ion source to the detector, only states with lifetimes larger than roughly $700\,\mu\mathrm{s}$ could be recorded here (see Sec. 4.1). Hence, levels in the $\mathrm{B}^2\Sigma_u^+$ state will not be considered as a possible origin of the measured signals. Therefore, the rate calculation for the AD and AF channel will be limited to the other three anionic states $X^2\Sigma_g^+$, $A^2\Pi_u$ and $C^4\Sigma_u^+$. For these three electronic states internal excitations up to and beyond the dissociation threshold of $\sim 8.4\,\mathrm{eV}$ are considered.

Calculations of the expected auto-fragmentation rates for ro-vibronic levels above the dissociation threshold are presented in Sec. 4.4. The different coupling mechanisms leading to auto-detachment available in C_2^- are described and the resulting rates discussed in Sec. 4.5. Afterwards, the calculated rates of the different decay channels are combined with a model describing the initial internal population of the ions in Sec. 4.6. With this, expected rates on the detector for both destructive decay processes (AF and AD) can be derived and compared to the measured signals. In the end, the results are discussed in Sec. 4.7.

4.1 Auto-decay measurements at the CSR

For this thesis, the auto-decay measurements carried out in the commissioning cryogenic beamtime of the CSR in 2015 will be used to evaluate the agreement with the calculations performed in this chapter. In contrast to the CSR facility status described in Chap. 2, the ring did not yet include the electron cooler and extraction beamline at that time. Then, the residual gas density within the ring was in the order of $120\,\mathrm{particles/cm^3}$ [26]. As a result, the count rate due to collisions with residual gas particles was so small, that it can be neglected for the study discussed here. Furthermore, the fraction of photons from the 300 K room-temperature radiation field was about 5×10^{-3} [26]. The data discussed here was previously considered in two other theses. One was the PhD thesis of Jürgen Göck [73], which focused on the AF signal after 100 ms storage time. In this work, only the ground state of C_2^- was considered to explain the measured signal. The potential of this state was approximated with a Morse potential and the AF rates calculated with the LEVEL16 program [74]. Other decay channels and any excited states of the dimer were neglected. The second work, in which this data is discussed, is my Master thesis [75]. This included the raw-data analysis, which will not be repeated here. Furthermore, first approximations on the radiative decay and AF rates of two the lowest-lying doublet states, $X^2\Sigma_g^+$ and $A^2\Pi_u$, were carried out in [75], as discussed in Sec. 4.3.2 and Sec. 4.4.1, respectively.

For the measurement, a sputter source (MISS) was installed on the large high-voltage ion source platform (called "Ion source platform 1" in Fig. 2.2). A carbon target was used to produced highly-excited C_2^- dimers, which were accelerated to 60 keV. A 35 µs pulse was injected into the ring and roughly 4×10^7 ions were stored in the CSR. Due to the low residual gas density and negligible photon-field, the dimers could spontaneously de-excite or undergo auto-detachment or auto-fragmentation undisturbed by external factors. Reaction products created by the destructive decay

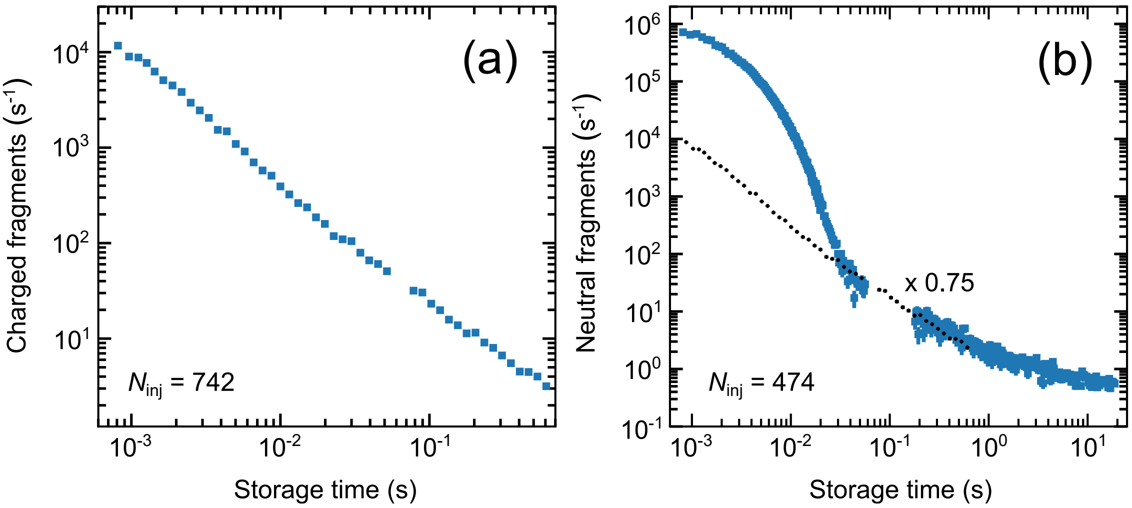

Figure 4.2: Auto-decay signals recorded at the CSR in 2015 with the COMPACT detector. (a) Signal s_c of the charged C^- fragment, averaged over 742 injections. (b) Signal s_n of the neutral fragments C and C_2, averaged over 474 injections. The charged fragment signal, scaled by 0.75, is drawn in black dots.

channels, AD and AF, produced in the straight section (B) which would later host the electron cooler (see Fig. 2.3), were detected by the COMPACT detector (see Sec. 2.2.3). Due to its location behind the first 6° deflector, the detector could be placed to record fragments with two different mass-to-charge ratios. One was at a position corresponding to the same charge but half the mass of the mother beam. Here, the charged carbon atom C^- produced during AF could be collected. At the other position, neutral fragments were recorded. These can either correspond to atomic carbon, produced during AF, or C_2, produced during AD. Consequentially, the signal rate recorded on the neutral position is the sum of both decay channels, while only the AF is visible for the charged fragment position.

Fig. 4.2 shows the signals recorded for the two detector positions. Since COMPACT could only be placed at one position at a time, the two curves were recorded in separate measurements on two consecutive days. Fig. 4.2(a) shows the signal s_c for the charged C^- fragment averaged over 742 injections. It displays a power-law behaviour, visible by the linear slope in the log-log plot. In Fig. 4.2(b), the neutral signal s_n on the detector is displayed in blue. Here, 474 injections were measured. In order to compare the two signals, the charged fragment curve is additionally plotted in this sub-figure with black dots. The signal is scaled by a factor of 0.75, such that the two curves overlap for storage times $\gtrsim 30\,\mathrm{ms}$. The apparent discrepancy between the amplitudes of the two signals is not surprising. The current output of ion sputter sources fluctuates during operation due to changing parameters like the amount of caesium present in the source. Since the measurements were performed on two separate days, the number of ions within an injection pulse of the same duration is not constant.

Both data sets shown in Fig. 4.2 display a gap at roughly 50 ms. This is due to the data acquisition system, which employed two memory banks to record the data. Here, one such memory bank acquired the counts, while simultaneously the data previously recorded on the other was written away into a data file. The alternation between the two banks happened every $\sim 25\,\mathrm{ms}$. In the beginning of the measurement, the count rate was so high, that the read-out time for the first bank exceeded 25 ms. As a result, the acquisition was shortly interrupted to process the data. The effect of this interruption on the measured rate and its uncertainty is analysed in [75].

A second measurement of the auto-decay of C_2^- was carried out in 2017. Before this beamtime, the CSR underwent two major upgrades. These were the implementation of the ring's electron cooler and extraction beamline (see Fig. 2.2). Both newly installed experimental stations include parts which are operated at room-temperature. As a result, the fraction of 300 K radiation of the photon-field inside the CSR increased between the two campaigns, which resulted in a higher residual gas density. Consequentially, the background rate due to residual gas collisions of the measurements performed in 2017 is almost two orders of magnitude higher than the previous measurements from 2015 [75]. Nevertheless, apart from the higher background signal in the later beamtime, the two data sets are compatible and display the same AD and AF curves [75]. However, due to the lower background signal in the early measurement, only the 2015 data set will be used in the following.

By integrating over the average number of events collected at the two detector positions, the fraction of the beam decaying through either AD or AF can be approximated. To this end, the detection efficiency of the produced fragments inside the ring has to be taken into account. The CSR has a circumference of $\sim 35\,\mathrm{m}$, however, only products created in the $\sim 4.5\,\mathrm{m}$ linear section in front of the detector can be collected by COMPACT (see Sec. 2.2.3). Additionally, the detector has a finite horizontal and vertical width, which is smaller than the expansion of the ion beam, resulting in a geometric detection efficiency of ~ 0.3. Furthermore, the electronic detection efficiency of ~ 0.5 [76] has to be taken into account. This yields a value of

$$\epsilon_{\mathrm{det}} \approx 4.5/35 \times 0.5 \times 0.3 = 0.02 \tag{4.3}$$

for the overall detection efficiency. The average number of counts per injection for the two detector positions for the storage time window $0.8\,\mathrm{ms} \geq \ t \ \geq 1\,\mathrm{s}$ are $N_c = 29$ and $N_n = 1567$ for the charged and neutral signal, respectively. These can be employed together with the initial number of ions $N_0 \approx 4 \times 10^7$ and ϵ_{det} from Eq. (4.3) to calculate the fraction of ions contributing to the two decay channels AF and AD

$$\begin{aligned} P_f &= \frac{N_c}{N_0\,\epsilon_{\text{det}}} \approx 3.6 \times 10^{-5}, \\ P_d &= \frac{N_d}{N_0\,\epsilon_{\text{det}}} \approx 1.9 \times 10^{-3}. \end{aligned} \tag{4.4}$$

The ions contributing to the AD signal were estimated by $N_d = N_n - 0.75 \times N_f$. As visible in Fig. 4.2, the AF signal is weaker by almost two orders of magnitude compared to the AD signal. Overall, about 2 per mill and therefore only a small fraction of the stored ions contribute to either of the auto-decay signals.

4.2 Electronic potentials and ro-vibronic states

This section is structured as follows. First, a brief introduction of the nomenclature of electronic states of homo-nuclear dimers is given in Sec. 4.2.1. Afterwards, the *ab initio* potential curves for electronic states in the neutral C_2 as well as the anionic C_2^- calculated by Ass. Prof. Dr. Milan Ončák, Innsbruck University, are discussed in Sec. 4.2.2. In the end, the influence of rotational excitation on the potentials are investigated in Sec. 4.2.3.

4.2.1 Notation of electronic states in homo-nuclear dimers

In contrast to atomic systems, the spherical symmetry is broken in (di-atomic) molecules. As a result, many atomic quantum numbers are no longer "good quantum numbers". However, the projection of the various angular momenta onto the internuclear axis can often be used to describe the system. The nomenclature of electronic states used in this thesis follows the one employed by Bernath [77]. The different relevant quantum numbers and symmetries are shortly listed below.

Spin The vector $\hat{\mathbf{S}}$ describes the spin angular momentum of the electronic state. The magnitude of $\hat{S}$ is given by the scalar $\mathbf{S} = |\hat{S}|$ and is the spin quantum number. The projection of $\hat{S}$ on the internuclear axis is given by the scalar $\mathbf{\Sigma}$, which comes in values of $\Sigma = -S, -S-1, ..., S$.

Electronic orbitals The sum of the angular momenta of the electronic orbitals is given by $\hat{\mathbf{L}}$. However, since the dimer does not have a spherical symmetry, $\hat{L}$ is no longer a conserved quantity and therefore not a good quantum number to describe the system. The projection of $\hat{L}$ onto the internuclear axis, $\mathbf{\Lambda}$, is used to describe the orbital angular momentum of an electronic state. States with $|\Lambda| > 0$ are orbital degenerate with $\Lambda = \pm|\Lambda|$. In contrast to atomic systems, Greek letters are used to describe the different values of Λ, with $|\Lambda| = 0, 1, ...$ corresponding to a Σ, Π, ... state, respectively.

Vibration The vibrational excitation of the system is described by the quantum number $\mathbf{v}$.

Nuclear rotation The nuclear rotation is given by $\hat{\mathbf{R}}$. Since this vector describes the rotation of the two nuclei, it is perpendicular to the internuclear axis. Hence, a value describing the projection of $\hat{R}$ onto the internuclear axis does not make sense.

Angular momentum excluding spin The angular momentum excluding spin is given by $\hat{\mathbf{N}} = \hat{R} + \hat{L}$. The corresponding scalar $\mathbf{N}$ can have values of $N = \Lambda, \Lambda + 1, ...$

Total angular momentum The total angular momentum including spin, described by $\hat{\mathbf{J}} = \hat{R} + \hat{L} + \hat{S}$, is a conserved quantity. Its projection onto the internuclear axis is given by $\mathbf{\Omega}$. Depending on the orientations of $\hat{L}$ and $\hat{S}$, it can have values of $\Omega = (-S - \Lambda), (-S - \Lambda + 1), ..., (S + \Lambda)$. The scalar value of $\hat{J}$ is given by $\mathbf{J}$. Depending on the relative orientation between $\hat{N}$ and $\hat{S}$, it can have values of $J = (N - S), (N - S + 1), ..., (N + S)$. Therefore, for non-singlet ($S > 0$) levels $(\hat{N}, \hat{S})$, $2S + 1$ fine-structure sublevels with different J values exist.

Total parity The total parity describes the symmetry under the inversion of the coordinates of all electrons and nuclei. The reference point for the inversion is the center of mass, which is the middle of the internuclear separation for homo-nuclear dimers. The effect of this inversion operation on the part of the wavefunction describing the electronic orbital is equivalent to inverting the coordinates of the electrons with respect to the molecular plane [77]. For Σ states this application of the inversion operator E^* only yields a single result with

$$E^* \left|\Sigma^\pm\right\rangle = \pm \left|\Sigma^\pm\right\rangle, \tag{4.5}$$

where a subscript of ± gives the corresponding parity with respect to this inversion. For orbitals $\Lambda > 0$, a degenerate pair with ± parity exists.

Gerade/ungerade parity The parity of only the electronic orbitals of a given state is denoted by g (symmetric) or u (antisymmetric).

Rotation(less) parity The total parity of the system is given by the product of its partial parities. The factor due to rotational excitation is given by $(-1)^J$. Consequentially, the total parity of the system alternates for changing J. In order to describe the parity of a state excluding rotational excitations, the labels e and f are used. Here, e/f corresponds to a positive/negative parity for the rotationless states.

Many parameters of the system can be directly read from the name of the occupied electronic state, which is typically given as ${}^{2S+1}\Lambda_{g/u}^{(+/-)}$ for homo-nuclear di-atomic molecules. As explained above, the "±" superscript only applies for Σ states here. Additionally, a letter in the beginning of the name of each electronic state indicates its energetic order with respect to the other states. Here, the ground state is labelled as "X", while excited states are labelled with "A, B, C, ...".

4.2.2 *Ab initio* potentials of the neutral and anionic carbon dimer

Ass. Prof. Dr. Milan Ončák from Innsbruck University carried out the *ab initio* calculations required to calculate the rates of the different decay channels available in the system. In this section, the potential curves will be presented. Further results from these calculations on the electronic transition moment between the anionic $\mathrm{X}^2\Sigma_g^+$ and $\mathrm{A}^2\Pi_u$ states as well as the mixing between the anionic $\mathrm{C}^4\Sigma_u^+$ and $\mathrm{A}^2\Pi_u$ states will be discussed in Sec. 4.3. All calculations were carried out using the state-averaged multi-configuration self-consistent field (MCSCF) approach and the multi-reference configuration interaction (MRCI) method of the MOLPRO package [80]. Here, an active space of 8 and 9 electrons in 8 orbitals was used for C_2 and C_2^-, respectively. The basis set was chosen as the augmented correlation-consistent basis of quadruple-zeta quality, aug-cc-pVQZ [81].

Fig. 4.3 shows the potential curves for the four lowest-lying states of the anionic dimer, $\mathrm{X}^2\Sigma_g^+$, $\mathrm{A}^2\Pi_u$, $\mathrm{B}^2\Sigma_u^+$ and $\mathrm{C}^4\Sigma_u^+$, as well as the two lowest states of the neutral system, $\mathrm{X}^1\Sigma_g^+$, $\mathrm{A}^3\Pi_u$. All potential curves are plotted for no rotational excitation. After the *ab initio* calculations using the MOLPRO package were obtained, it was apparent that part of the third excited anionic state $\mathrm{C}^4\Sigma_u^+$ lies above the lowest neutral curve into which detachment from this states is allowed ($\mathrm{A}^3\Pi_u$). Due to the singlet nature of the neutral ground state ($\mathrm{X}^1\Sigma_g^+$), it is not available for the detachment from the quartet state (see Sec. 4.5.3). Consequentially, the $\mathrm{C}^4\Sigma_u^+$ potential curve is resonant with respect to detachment for internuclear distances $R \lesssim 1.61\,\text{Å}$. The calculations carried out with MOLPRO are best suited for bound states, while R-matrix calculations [82] generate better results for resonances. Past studies employing R-matrix methods on a multitude of resonant states of C_2^- have been carried out and published [78, 79]. Results on the $\mathrm{C}^4\Sigma_u^+$ state discussed in these publications were used to modify the resonant part of the potential curve here.

The inset of Fig. 4.3 shows the results published by Halmová et al. in red squares as well as the *ab initio* (MOLPRO) curve in a grey solid line. A parametrization was carried out to obtain a modified, smooth curve. To this end, for internuclear distances below the crossing point with the neutral $\mathrm{A}^3\Pi_u$ state at $R \approx 1.61\,\text{Å}$ the R-matrix results were considered. For $R \gtrsim 1.61\,\text{Å}$ the MOLPRO calculations were employed. The modified potential obtained by using both these data sets is then

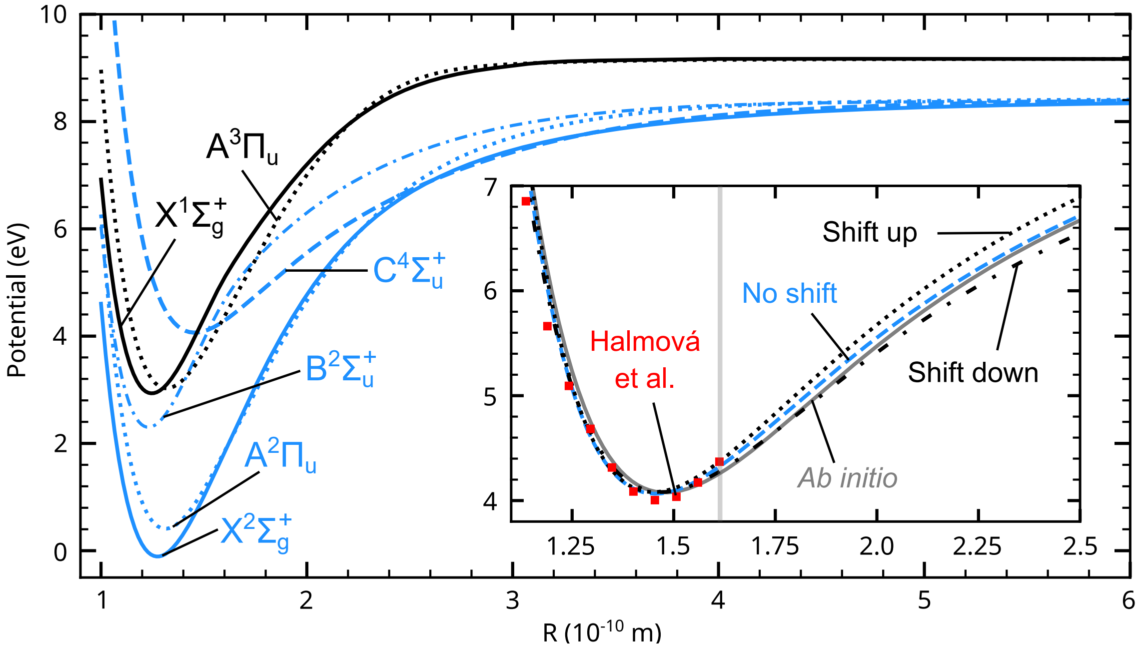

Figure 4.3: Potential curves of the four lowest-lying electronic states of the anionic carbon dimer, $X^2\Sigma_g^+$, $A^2\Pi_u$, $B^2\Sigma_u^+$ and $C^4\Sigma_u^+$ (blue), as well as the lowest two electronic states of the neutral carbon dimer, $X^1\Sigma_g^+$, $A^3\Pi_u$ (black). Inset: Parametrization of the $C^4\Sigma_u^+$ potential. The *ab initio* results employing the MOLPRO package are drawn in a solid grey line. The red squares are from R-matrix calculations carried out by Halmová et al. [78, 79]. A horizontal grey line marks the transition between the resonant and bound part of the potential. The dashed blue line gives the parametrized curve using both data sets. The modified potential curves used to estimate the uncertainty of the auto-detachment rate calculations are drawn in black. The potential derived by shifting the *ab initio* (MOLPRO) curve up/down by 170 meV while leaving the R-matrix values unchanged is drawn in a dotted/dashed-dotted line. The *ab initio* (MOLPRO) calculations were carried out by Ass. Prof. Dr. Milan Ončák, Innsbruck University.

shown in a dashed blue line, which is also the one plotted in the overview of potential curves given in Fig. 4.3. The calculations described in Sec. 4.5.3 concerning the auto-detachment from this state were strongly dependent on the shape of the anionic quartet curve with respect to the neutral triplet potential. In order to estimate this dependence, the rates were calculated for two modified potential curves of the $C^4\Sigma_u^+$ state as well. To this end, the *ab initio* (MOLPRO) curve was shifted up and down by 170 meV, a value which reflects the typical uncertainty of these type of *ab initio* calculations. Afterwards, the parametrization using the unchanged R-matrix values

Table 4.1: Comparison between electronic state parameters of the neutral/charged carbon dimer without rotational excitation used in this work and previous experimental and theoretical studies. T is the temperature with respect to the ground state, R_0 is the equilibrium bond length, ω_e the harmonic vibrational wavenumber, $\omega_e x_e$ the unharmonicity of ω_e and D_0 the dissociation limit.

	T (cm^{-1})	R_0 (Å)	ω_e (cm^{-1})	$\omega_e x_e$ (cm^{-1})	D_0 (eV)
			Anionic dimer		
$\mathbf{X^2\Sigma_g^+}$					
This work	0	1.274	1770	12.4	8.41
Exp. [66]	0	1.2684	1781.202(20)	11.6716(48)	-
Exp. [2]	0	1.2682	1781.04	11.58	8.48
Cal. [12]	0	1.276	1780	12	-
Cal. [67]	0	1.267	1799	-	8.42
Cal. [69]	0	1.2685	1787.40	11.56	7.65
Cal. [15]	0	1.2689	1781.56748	11.5247	-
$\mathbf{A^2\Pi_u}$					
This work	4128	1.313	1657	11.2	7.90
Exp. [66]	4064(91)	1.313	1656(10)	10.80(26)	-
Cal. [12]	3512	1.318	1646	11	-
Cal. [67]	4463	1.307	1694	-	7.87
Cal. [69]	4050.6	1.3066	1679.04	11.61	7.38
Cal. [15]	4004.91162	1.3075	1668.72707	10.79763	-
$\mathbf{B^2\Sigma_u^+}$					
This work	19529	1.230	1964	20.0	5.99
Exp. [66]	18390.723(35)	1.2234	1959.542(84)	15.100(57)	-
Exp. [2]	18390.88	1.2233	1968.73	14.43	-
Cal. [12]	18941	1.231	1983	16	-
Cal. [67]	19783	1.222	2013	-	5.97
Cal. [69]	18763.9	1.2234	1964.72	10.28	6.14
Cal. [15]	18981.3074	1.2238	1976.17619	14.75376	-
$\mathbf{C^4\Sigma_u^+}$					
This work	33430	1.480	1092	10.9	4.27
Cal. [15]	33226.969	1.4641	1128.97168	11.26472	-
			Neutral dimer		
$\mathbf{X^1\Sigma_g^+}$					
This work	0	1.247	1845	14.8	6.12
Exp. [2, 67]	0	1.2425	1854.71	13.34	6.32
Cal. [67]	0	1.242	1864	-	6.29
$\mathbf{A^3\Pi_u}$					
This work	645	1.318	1640	14.3	6.04
Exp. [2, 67]	716	1.3119	1641.35	11.67	6.23
Cal. [67]	885	1.311	1653	-	6.18

Table 4.2: Comparison between the electron affinity derived in this work and previous theoretical and experimental studies. Values are given in eV.

This work	Exp. [70]	Exp. [83]	Cal. [67]	Cal. [84]
3.042	$3.46^{+0.15}_{-0.10}$	3.268(7)	3.17	3.264(43)

was carried out again. Here, care was taken that the resulting curves are smooth and do not display a step at the transition between the two data sets at $R \approx 1.61\,\text{Å}$. The potentials for the shift up and down are shown in a dotted and dashed-dotted line in the inset of Fig. 4.3, respectively.

The spectroscopic parameters of the potential curves shown in Figure 4.3 are listed in Tab. 4.1. In order to approximate the vibrational frequencies ω_e and their unharmonicities $\omega_e x_e$, the first 10 vibrational levels of each electronic state were used. The vibrational levels were identified using the Numerov method [85]. Some of the spectroscopic values deviate notably from previously published data. The largest deviations can be found for the second excited anionic state $\mathrm{B}^2\Sigma_u^+$. However, as will be discussed in the following sections, levels originating from this state do not contribute to the measured signal investigated here due to insufficient lifetimes. A comparison between the electron affinity (EA) derived here and in previous works is given in Tab. 4.2. The value obtained here is lower than the experimental results given in [83] by about 226 meV. For the auto-detachment rates calculated in Sec. 4.5 the neutral curves are shifted upwards at all internuclear distances to match the experimental value of the EA. Otherwise, no corrections were carried out on the potential curves to improve the agreement with previous studies. This was done to maintain consistency for the calculations carried out in the following Sec. 4.3 - 4.5. These use the *ab initio* results to estimate the potential curves at high rotational excitation, where large equilibrium distances R become important. The spectroscopic parameters given in previous publications and listed in Tab. 4.1 only provide an accurate description of the potential shape around the equilibrium distance and are not suited to estimate the curves at large R. Additionally, the unedited potentials are more consistent with respect to the coupling functions used in Sec. 4.3, which were obtained in course of the same *ab initio* calculations.

4.2.3 Rotationally excited potential curves

The approach outlined by Fedor et al. [5] is employed to add rotational excitation to the model and obtain potentials $V_N(R)$, which include rotations. To this end, a centrifugal energy term $E_N(R)$ is added to the *ab initio* curves $V_0(R)$:

$$V_N(R) = V_0(R) + E_N(R) = V_0(R) + \frac{\hbar^2}{2\mu R^2}\left[N(N+1) - \Lambda^2\right]. \tag{4.6}$$

Here, $\hbar$ is the reduced Planck constant and μ the reduced mass of the molecule, in this case $\mu(^{12}\mathrm{C}_2) = 6\,\mathrm{u}$. Λ is the z-component of the angular momentum of the electronic orbital of a given state and N is the total angular momentum excluding spin (see Sec. 4.2.1). For the carbon dimer made up for two ^{12}C atoms, as is the case in this study, not all ro-vibronic states in the system are available. Due to the nuclear spin $I = 0$ of ^{12}C, the system consists of two indistinguishable bosons. Hence, the total wavefunction must be symmetric under the exchange of the two nuclei. Therefore, the product of the total parity of the state, given by $\left(\epsilon_N(-1)^N\right)$ and the electronic inversion parity, labeled as g and u, has to be positive. For ϵ_N the labels of Hund's case (b) basis states are used [86]. This assumption of weak spin-orbit coupling is valid for all excitations in the Σ states (since $\Lambda = 0$), and also for the high rotational excitations in the Π state considered in the following Secs. 4.3.2 and 4.4. For Σ_g/Σ_u states, for which $(\epsilon_N = 1)/(\epsilon_N = -1)$, only even/odd rotational excitations N are possible. For electronic states with $\Lambda > 0$, for which normally degenerate levels with $\epsilon_N = \pm 1$ exist, only one ϵ_N is available for a given N and the levels alternate between the different ϵ_N values. For the Π_u states relevant for this work, even N have $\epsilon_N = -1$ levels while for odd N states only $\epsilon_N = 1$ levels are available.

Figure 4.4 shows the potentials of the lowest-lying electronic states of the neutral and charged carbon dimer for different rotational excitations. In sub-figure (a) the rotationless curves, as shown in Fig. 4.3, are plotted for comparison. The other two sub-figures show the curves for different rotational excitations N. Due to the symmetry restrictions discussed above, it is not possible to apply the same rotational excitations to all potentials, since Σ_g/Σ_u states require even/odd values of N. Here, the even N were chosen to be smaller than the odd values. For the Π states, the larger (odd) rotational excitation was used.

When calculating the potential landscape for an arbitrary value of N, the relative energy difference between two curves at any internuclear distances R remains the same as long as the same rotational excitation is assumed for both potentials. This is due to the independence of the centrifugal energy term on the internal excitation of the system (see Eq. (4.6)). Nevertheless, the addition of the centrifugal energy term has multiple effects on the curves. With increasing N the potential depth decreases as the system becomes less bound. Additionally, the equilibrium distances of the potentials move to larger values. For curves which intersect this leads to a rearrangement of the electronic potentials for rotational excitations above a critical value N_{cr}. Two such rearrangements can be seen in Fig. 4.4, which both have significant effects on the relevant decay rates.

In sub-figure (b), the potential curves for rotational excitation $N = 171$ ($N = 170$ for Σ_g) are plotted. As shown by a zoom in the relevant region in the inset of the sub-figure, the anionic $\mathrm{C}^4\Sigma_u^+$ and the neutral $\mathrm{A}^3\Pi_u$ states have rearranged with the potential minimum of the anionic curve now lying below that of the neutral curve. Starting at rotational excitation $N_{\mathrm{cr}} = 155$, the zero-point-energy (ZPE), the energy

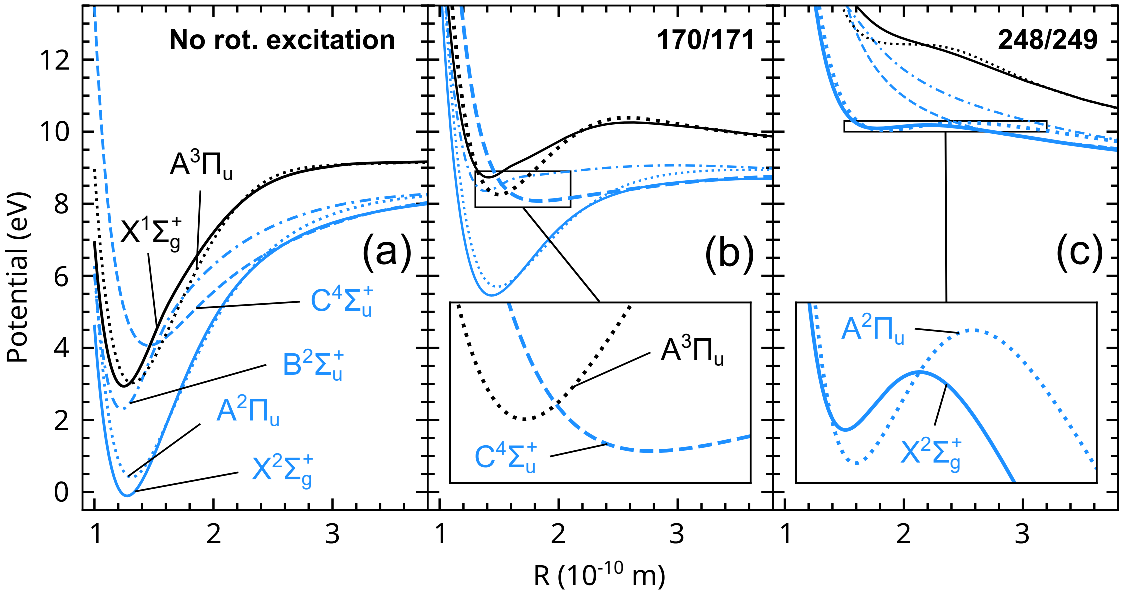

Figure 4.4: Potential curves of electronic states of the neutral (black) and charged (blue) carbon dimer for different rotational excitations N. (a) *Ab initio* curves without rotational excitations as shown in Fig. 4.3. (b) Potential curves for rotational excitation $N = 171$ ($N = 170$ for Σ_g states). The inset shows the potentials for the neutral $A^3\Pi_u$ and the anionic $C^4\Sigma_u^+$ state for the region marked with a black box. The potentials have rearranged with respect to the their rotationless configuration. (c) Potential curves for rotational excitation $N = 249$ ($N = 248$ for Σ_g states). The inset shows the potentials for the anionic $X^2\Sigma_g^+$ and $A^2\Pi_u$ states for the region marked with a black box. The potentials have rearranged with respect to the their rotationless configuration.

of the energetically lowest-lying level in the potential, of the anionic quartet state lies below that of the neutral triplet state. This strongly affects the auto-detachment rates for levels in $C^4\Sigma_u^+$, which is discussed in Sec. 4.5.3.

In Fig. 4.4(c), a rotational excitation of $N = 249$ ($N = 248$ for Σ_g states) is applied. Again, the inset shows a zoom into the relevant region for a rearrangement of potentials, this time between the lowest two anionic curves, $X^2\Sigma_g^+$ and $A^2\Pi_u$. The critical rotational excitation for this rearrangement is $N_{\mathrm{cr}} = 220$. The influence on the radiative lifetimes of levels in both states will be discussed in Sec. 4.3.2. The potentials in the inset of sub-figure 4.4(c) furthermore display another consequence of high rotational excitation. At sufficiently high values of N, a rotational barrier forms behind which metastable levels exist above the dissociation limit ($D_0 \approx 8.41\,\mathrm{eV}$ here), which can decay by tunnelling through the barrier. This auto-fragmentation process is considered in detail in Sec. 4.4.

4.3 Radiative decay rates

Due to the absence of a permanent dipole moment in C_2^-, radiative decay is only possible through transitions between electronic states of the system in the dipole approximation. Ro-vibrational transition within the same electronic state are dipole forbidden. A detailed introduction into electronic transitions with a focus on diatomic molecules can for example be found in the book of Peter F. Bernath [77]. Here, only the results of the theoretical derivations and considerations are shortly summarized.

Dipole-allowed electronic transitions in homo-nuclear dimers are governed by a number of selection rules arising from symmetry considerations and momentum conversation restrictions. Those which influence the available transitions in C_2^- and their implications are shortly discussed below.

Electronic orbital parity Electronic transitions do not change the parity of the electronic orbital under the inversion of the electronic coordinates with respect to the molecular plane (see Sec.4.2.1). Consequentially, while $\Sigma^+ - \Sigma^+$ and $\Sigma^- - \Sigma^-$ transitions are allowed, $\Sigma^+ - \Sigma^-$ transitions are forbidden. For states with $\Lambda > 0$ this selection rule does not apply, since a degenerate $\pm$ pair of sublevels exists.

Nuclei exchange parity Radiative transitions do not change the parity of the total wavefunction under exchange of the nuclei. Notably, in case of the carbon dimer, this selection rule is the reason why the number of final states for the radiative decay from any arbitrary initial state in the system remains the same when applying the nuclear spin restriction. The states with a negative parity under nuclei exchange, which are unavailable for the carbon dimer, would not have participated in radiative transitions involving the remaining states, if they were populated.

$g \leftrightarrow u$ Electronic transitions are only possible between states with different *gerade/ungerade* parities. In the case of C_2^-, the three excited states of u symmetry can only decay into the $X^2\Sigma_g^+$ ground state of the system but not into each other. For the electronic ground state, all three electronic excited states are available for radiative de-excitation, as long as their ZPE lies energetically lower than the vibrational level of interest.

$\Delta S = 0$ For spin-allowed transitions, the spin has to remain unchanged. However, spin-orbit coupling enables weak transitions between states with different spins. One example for this, the transition from the third excited state of C_2^- $C^4\Sigma_u^+$ with $S = \frac{3}{2}$ to the doublet ground state $X^2\Sigma_g^+$ ($S = \frac{1}{2}$) via coupling to the $A^2\Pi_u$ state, is discussed in Sec. 4.3.3.

$\Delta\Sigma = 0, \pm 1$ Due to the relation between Ω and Λ (see Sec. 4.2.1), this rule automatically implies a restriction of $\Delta\Lambda = 0, \pm 1$ for transitions with $\Delta S = 0$. This is given for the spin-allowed $^2\Sigma$ − $^2\Pi$ transition considered here.

The rate of a dipole-allowed electron transition from an initial state a' with parameters $|\gamma', S', \epsilon'_N, J', N', v'\rangle$, where γ is used to describe the electronic state, to a final state b'' with $|\gamma'', S'', \epsilon''_N, J'', N'', v''\rangle$ is given by [87]:

$$A_{a'}^{b''} = C_0 \left(\nu_{a'}^{b''}\right)^3 \frac{S_{a'}^{b''}}{2J' + 1}. \tag{4.7}$$

Here, C_0 is a constant given by $\frac{16\pi^3}{3\epsilon_0 h}$ and $\nu_{a'}^{b''}$ is the energy difference between the initial and final state in wavenumbers. J is the total angular momentum including spin (see Sec. 4.2.1). $S_{a'}^{b''}$ is the line strength of the transition. It can be calculated through the square of the effective dipole matrix element, given by [87]

$$S_{a'}^{b''} = |\langle a'| \mu_{eff} |b''\rangle|^2, \tag{4.8}$$

where μ_{eff} is the electronic transition moment. The parameter $S_{a'}^{b''}$ includes the coupling between the initial and final state. The nature of this coupling differs for the two transition $A^2\Pi_u$ - $X^2\Sigma_g^+$ and $C^4\Sigma_u^+$ - $X^2\Sigma_g^+$, described in Sec. 4.3.2 and Sec. 4.3.3, respectively. Therefore, the specification of $S_{a'}^{b''}$ for the two cases is discussed in the respective sub-sections. The total radiative decay rate of an initial state a' can be derived by summation over the individual decay rates for the transitions to all possible lower-lying final states $\bar{b}$:

$$A_{a'} = \sum_{\bar{b}} A_{a'}^{\bar{b}}. \tag{4.9}$$

The rest of this section is structured in the following way: A short overview of previous theoretical and experimental studies of electronic transitions of C_2^- is given in Sec. 4.3.1. Afterwards, calculations for the radiative decay between the lowest two doublet states of the system, $X^2\Sigma_g^+$ and $A^2\Pi_u$, are presented in Sec. 4.3.2. Afterwards, the spin-forbidden transition from the third excited $C^4\Sigma_u^+$ quartet state to the $X^2\Sigma_g^+$ ground state is discussed in Sec. 4.3.3.

4.3.1 Previous studies on the radiative decay of C_2^-

Multiple theoretical and experimental studies on electronic transitions in C_2^- have been carried out in the past [12, 16, 15, 71]. They focused on the three doublet states $X^2\Sigma_g^+$, $A^2\Pi_u$ and $B^2\Sigma_u^+$ of the system, or a subset of those. No publications concerning the radiative decay of the third excited $C^4\Sigma_u^+$ quartet state of the dimer could be found in the course of this work. Below the findings of the previous studies will be shortly summarized by electronic state.

The energetic separation of the lowest two electronic states, $X^2\Sigma_g^+$ and $A^2\Pi_u$, is small with only $\sim 0.5\,\mathrm{eV}$. As a result, only vibrational levels $v < 3$ of the $X^2\Sigma_g^+$ ground state of the system are stable against radiative decay to the $A^2\Pi_u$ excited state. Theoretical calculations carried out by Rosmus and Werner in 1984 [12] estimated the lifetimes τ_v of vibrations $v = 3 - 10$ assuming no rotational excitation. For the lowest metastable level $v = 3$, they derived a lifetime of 2 s, with a decrease in τ_v of roughly a factor 2 for every additional vibrational quantum. A later experimental study at the ASTRID storage ring in Aarhus [16] used photo-detachment to probe the radiative decay of vibrations $v = 2 - 4$ of the electronic ground state. For ion production, the authors used a sputter source. Consequentially, the dimers populated a wide range of rotational states, which were probed in the experiment. Pedersen et al. [16] could place a lower lifetime limit of 5 s on the $v = 2$ level of the system. The authors pointed out, that they were unable to see any decay of this level during their measurement window ($\lesssim 20\,\mathrm{s}$), which is consistent with the results by Rosmus and Werner [12]. For vibrational level $v = 3$ a lifetime of $0.32 \pm 0.02\,\mathrm{s}$ is given, which is significantly smaller than the previous theoretical value of 2 s [12]. The authors point out that this discrepancy is most likely caused by the rotational excitation of the system. To validate this assumption, Pedersen et al. provided theoretical calculations on the rotational excitation dependence of the lifetime of $v = 3$. Here, they showed that $\tau_{v=3}$ decreases with increasing N. However, they noted that for their calculation to match the experimental lifetime, the rotational population would have to peak at a value larger than $N = 100$, which they considered to be unlikely. For vibrational excitation $v = 4$, Pedersen et al. provided an upper lifetime limit of 100 ms, which is also significantly smaller than the Rosmus and Werner value of 541 ms. An experimental study at the TMU E-ring in Tokyo in 2020 [71] also investigated the radiative lifetimes of low-lying vibrational levels of the electronic ground state through photo-detachment. In order to simulate the recorded depopulation of the vibrational states, the authors used the LEVEL program [74] to first estimate the lifetimes. Here, they derived values which agree with the lifetimes calculated by Rosmus and Werner within 12%. Iida et al. [71] were not able to extract lifetimes from the measured data directly. However, the model they used to simulate the decaying signal had a better agreement with the measured rate for the lifetimes derived in their work than the once measured by Pedersen et al..

For the first excited $A^2\Pi_u$ state of the system, radiative relaxation occurs through the coupling to the $X^2\Sigma_g^+$ ground state. For levels in $A^2\Pi_u$, Rosmus and Werner derived radiative lifetimes starting at 49.9 µs for $v = 0$ and decreasing to 18.8 µs for $v = 10$ [12]. A later theoretical study by Shi et al. [15] used the MOLPRO package [80] also employed for the *ab initio* calculations discussed in Sec. 4.2.2. This presents a much higher level of theory than the previous calculation. The authors gave two different values for the radiative decay of each vibrational level, one with and one without a degeneracy factor included in the calculation. The latter method provides a good agreement with the previous calculations. However, the former (including the initial state's degeneracy) is roughly a factor 2 smaller than the results by Rosmus and Werner. Unfortunately, Shi et al. did not specify the used degeneracy factor and its derivation.

For the second excited $B^2\Sigma_u^+$ state, the theoretical studies yield a much better agreement. The work by Shi et al. again includes two lifetimes for each vibrational level, one with and one without the degeneracy factor. Here, the discrepancy between the two methods is $< 1\%$. Unfortunately, due to the missing description of said factor in the publication, any explanation on why this is the case would only be speculative here. The radiative lifetimes given for the first seven vibrations fluctuate in a range of about $71\,\text{ns} < \tau_v < 73\,\text{ns}$ [15]. This is in reasonably good agreement with the calculation by Rosmus and Werner, where the lifetime range for these vibrations is $75\,\text{ns} < \tau_v < 78\,\text{ns}$ [12]. An experimental study by Leutwyler et al. [88] could measure the lifetimes of the lowest two vibrational levels. To this end, the authors photo-excited the ions from the ground state and measured the fluorescence of the decaying dimers. They give values of $\tau_{v=0} = 77 \pm 8\,\text{ns}$ and $\tau_{v=1} = 73 \pm 7\,\text{ns}$, which agree with both theoretical studies.

4.3.2 Radiative relaxation of doublet states $\mathbf{X^2\Sigma_g^+}$ and $\mathbf{A^2\Pi_u}$

Transitions between the first two electronic states of C_2^- abide by all selection rules listed in the beginning of this Sec. 4.3 and are spin-allowed. The effective dipole matrix element, given by Eq. (4.8), can therefore be written as [77]

$$S_{a'}^{b''} = |\mu_{eff}(a', b'')|^2 \hat{S}_{a'}^{b''}. \tag{4.10}$$

Here, $|\mu_{eff}(a', b'')|^2$ can be calculated using the vibrational wavefunctions $\psi_{a'}(R)$ and $\psi_{b''}(R)$ of the initial and final state, respectively, as well as the internuclear distance dependent electronic transition function $\boldsymbol{\mu}(R)$,

$$|\mu_{eff}(a', b'')|^2 = \left(\int \psi_{a'}^*(\tilde{R}) \boldsymbol{\mu}(\tilde{R}) \psi_{b''}(\tilde{R}) d\tilde{R} \right)^2. \tag{4.11}$$

Hence, this factor is the squared integral of the convolution between the Franck-Condon factor of the initial and final state and the electronic transition moment.

$\boldsymbol{\mu}(R)$ was derived in the course of the *ab initio* calculations by Ass. Prof. Dr. Milan Ončák, Innsbruck University, which are outlined in Sec. 4.2.2. In Fig. 4.5, the electronic transition function is compared to previously published works [12, 15, 69]. Sub-fig. (a) shows the different $\boldsymbol{\mu}(R)$. The transition moment used here is drawn in a blue line. The values derived by Rosmus and Werner [12], Shi et al. [15], and Sedivcova and Spirko [69] are indicated with black crosses, grey diamonds and brown open cycles, respectively. Fig. 4.5(b) shows the relative deviation $\Delta\left(\mu(R)\right)/\mu(R)$ between the $\boldsymbol{\mu}(R)$ used in this work and previous calculations. For the two more recent works, deviations of up to $\sim 8\,\%$ with respect to Shi et al. and up to $\sim 12\,\%$

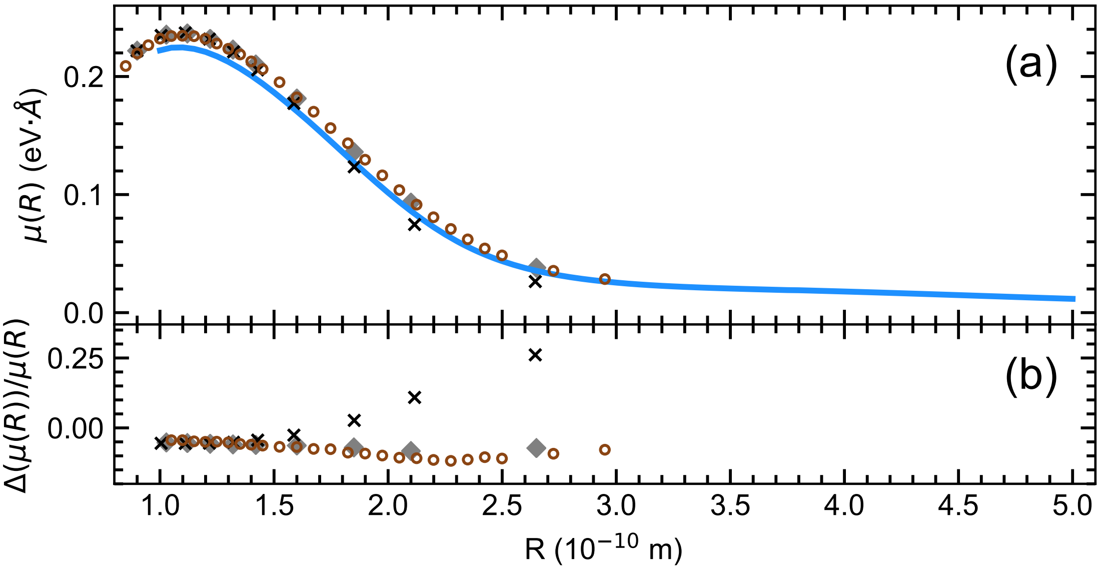

Figure 4.5: Comparison of different *ab intio* $\boldsymbol{\mu}(R)$ for the $X^2\Sigma_g^+$ - $A^2\Pi_u$ transition. (a) Electronic transition moment calculated by Ass. Prof. Dr. Milan Ončák is drawn in blue line. Previous calculations by Rosmus and Werner [12], Shi et al. [15], and Sedivcova and Spirko [69] are shown in black crosses, grey diamonds and brown open circles, respectively. (b) Relative deviation $\Delta\left(\mu(R)\right)/\mu(R)$ between previous calculations and the $\boldsymbol{\mu}(R)$ used here.

with respect to Sedivcova and Spirko could be found, with the transition moment used here lying below the published ones for all values of R. These two publications also include values of $\mu_{eff}(v', v'')$ for a variety of transitions. Those involving the first five vibrational levels in both electronic states ($v' = 0...4$ and $v'' = 0...4 \rightarrow 5 \times 5 = 25$ transitions) were compared to the values calculated in this thesis. The maximum relative deviation between results from Shi et al. and this work is $< 9\,\%$, much lower than for values by Sedivcova and Spirko, which differ by up to almost $65\,\%$. Latter relative deviation roughly matches the maximum discrepancy between the two publications of $\sim 63\,\%$. Based on these comparisons, the parameters used in this work to derive the $\mu_{eff}(v', v'')$ values can be deemed sufficiently accurate to carry out the radiative rate calculations. These parameters are the electronic transition moment $\boldsymbol{\mu}(R)$ as well as the vibrational wavefunctions obtained using the Numerov method [85].

The second factor in Eq. (4.10), $\hat{S}_{a'}^{b''}$, is the Hönl-London factor of the transition, which considers the degeneracy of the initial and final states. For a transition between two multiplet states ($S > 0$), this factor was derived by J. K. G. Watson [86] and will be used here. According to Eqs. (37) and (38) of the publication, in the case of two Hund's case (b) states the Hönl-London factor can be written as [86]

$$\begin{aligned}\hat{S}_{a'}^{b''} &= (2J'+1)(2J''+1)\left\{\begin{array}{ccc} N' & 1 & N'' \\ J'' & S & J' \end{array}\right\}^2 \\ &\times \frac{1}{2}\left[1+\epsilon'_N\epsilon''_N(-1)^{1+N'-N''}\right] \times (1+\delta_{\Lambda'0}+\delta_{\Lambda''0}-2\delta_{\Lambda'0}\delta_{\Lambda''0}) \\ &\times (2N'+1)(2N''+1)\left(\begin{array}{ccc} N' & 1 & N'' \\ -\Lambda' & \Lambda'-\Lambda'' & \Lambda'' \end{array}\right)^2 .\end{aligned} \tag{4.12}$$

The matrices in the round and curly parentheses are $3j$- and $6j$-Wigner symbols [89], respectively. In the case considered here, the coupling between a Σ ($\Lambda = 0$) and a Π ($\Lambda = 1$) state, the second line of the equation gives a value of 2 if the initial and final state have the opposite total parity and 0 otherwise. The total parity of a Hund's case (b) state is given by $(-1)^N \epsilon_N$ (see Eq. (32) in [86]). Since both states considered are categorized as Hund's case (b), it is convenient to define transitions between states of a certain N' and N''. Hence, it is necessary to sum over all possible final values of J''. To this end, the sum rule of the squared $6j$-Wigner symbol, given in Eq. (39) of [86] can be used:

$$\sum_{J''}\left\{\begin{array}{ccc} N' & 1 & N'' \\ J'' & S & J' \end{array}\right\}^2 = \frac{1}{(2J''+1)\,(2N'+1)}. \tag{4.13}$$

Using Eq. (4.13) and the considerations above, Eq. (4.12) can be re-written to

$$\hat{S}_{a'}^{b''} = 2(2J'+1)(2N''+1)\left(\begin{array}{ccc} N' & 1 & N'' \\ -\Lambda' & \Lambda'-\Lambda'' & \Lambda'' \end{array}\right)^2 . \tag{4.14}$$

It is important to remember, that this equation only applies for transition between states with opposite total parity (see Eq. (4.12)). Otherwise $\hat{S}_{a'}^{b''}$ is 0 and the transition is forbidden. Inserting Eq. (4.14) into Eq. (4.10) and applying the result to Eq. (4.7), the radiative rates for transitions between the ground and first excited state of C_2^- can be derived. For a decay from an initial state a' in $X^2\Sigma_g^+$ into a final state b'' in $A^2\Pi_u$, Eq. (4.7) can be written as

$$A_{X,a'}^{A,b''} = 2C_0\left(\nu_{a'}^{b''}\right)^3 |\mu_{eff}(a',b'')|^2(2N''+1)\left(\begin{array}{ccc} N' & 1 & N'' \\ 0 & -1 & 1 \end{array}\right)^2 . \tag{4.15}$$

Analogous, the decay rate from an initial state a' in $A^2\Pi_u$ into a final state b'' in $X^2\Sigma_g^+$ is given by

$$A_{A,a'}^{X,b''} = 2C_0\left(\nu_{a'}^{b''}\right)^3 |\mu_{eff}(a',b'')|^2(2N''+1)\left(\begin{array}{ccc} N' & 1 & N'' \\ -1 & 1 & 0 \end{array}\right)^2 . \tag{4.16}$$

The total radiative decay rate of an initial state a' can then be calculated by summing over all partial decay rates considering all available final states according to Eq. (4.9).

In the rest of this section, results of the calculations concerning the radiative decay of the lowest two doublet states, $\mathrm{X}^2\Sigma_g^+$ and $\mathrm{A}^2\Pi_u$, of C_2^- are presented. First approximations of these rates were already carried out in the course of my Master's thesis [75]. Due to limited knowledge on the Hönl-London factor for doublet states at the time, the degeneracy factor of $\left(\hat{S}_{a'}^{b''} / (2J'+1)\right)$ was set to a value of 1. This led to an overestimation of the derived decay rates. The results discussed here are an extension of these calculations.

Results for the radiative decay from the $\mathbf{X}^2\Sigma_g^+$ state

Only levels with even rotational excitations N are available in the $\mathrm{X}^2\Sigma_g^+$ state of the system. These can decay with $\Delta N = 0, \pm 1$ into levels of the first excited $\mathrm{A}^2\Pi_u$ state. Total radiative decay rates were calculated according to the procedure outlined above employing Eq. (4.15).

The resulting total radiative decay rates A_j for the lowest twenty vibrational levels of the $\mathrm{X}^2\Sigma_g^+$ state are plotted versus N in Fig. 4.6. Rates belonging to the same vibrational levels are connected with a thin line in the plot. In sub-figure (a), vibrational levels $v = 0 - 4$ are highlighted in blue. At low rotational excitations, the three lowest-lying vibrational levels are radiatively stable. This is caused by the energetic position of the levels below the ZPE not only of the $\mathrm{A}^2\Pi_u$ state with the same rotational excitation but also for $\Delta N = -1$. However, as the two electronic states rearrange at high N, see Sec. 4.2.3, this decay channel opens even for the lowest-lying vibrational levels of the ground state. The minimum rotational excitation at which radiative decay is possible of $v = 0, 1, 2$ was found to be $N_{\mathrm{min}} = 204, 162, 82$, respectively. The corresponding decay rates for these channel openings are given together with A_j of the first six vibrational levels for a few exemplary values of N in Tab. 4.3.

As visible both in the table as well as in Fig. 4.6, radiative decay rates increase with increasing rotational excitation, an observation in agreement with previous studies [16]. This dependency also applies to higher-lying vibrational levels, as visible in Fig. 4.6(b). Here, the focus is placed on the region of total radiative decay rates corresponding to levels with $4 < v < 20$, which are highlighted in blue. The N-dependence can be explained by the rearrangement of the two electronic states. As the rotational excitation increases, the final $\mathrm{A}^2\Pi_u$ state moves energetically lower with respect to the ground state. As a result, more final vibrational excitations in the potentials corresponding to $\Delta N = 0, \pm 1$ of $\mathrm{A}^2\Pi_u$ are available to decay to. Furthermore, the energetic separation between a fixed set of initial and final vibrational levels increases, which enters the radiative decay rate calculation to the third power (see Eq. 4.15). At very high values of N, the dependency of A_j reverses and the rates decrease again. This can be explained by the decreasing availability of final

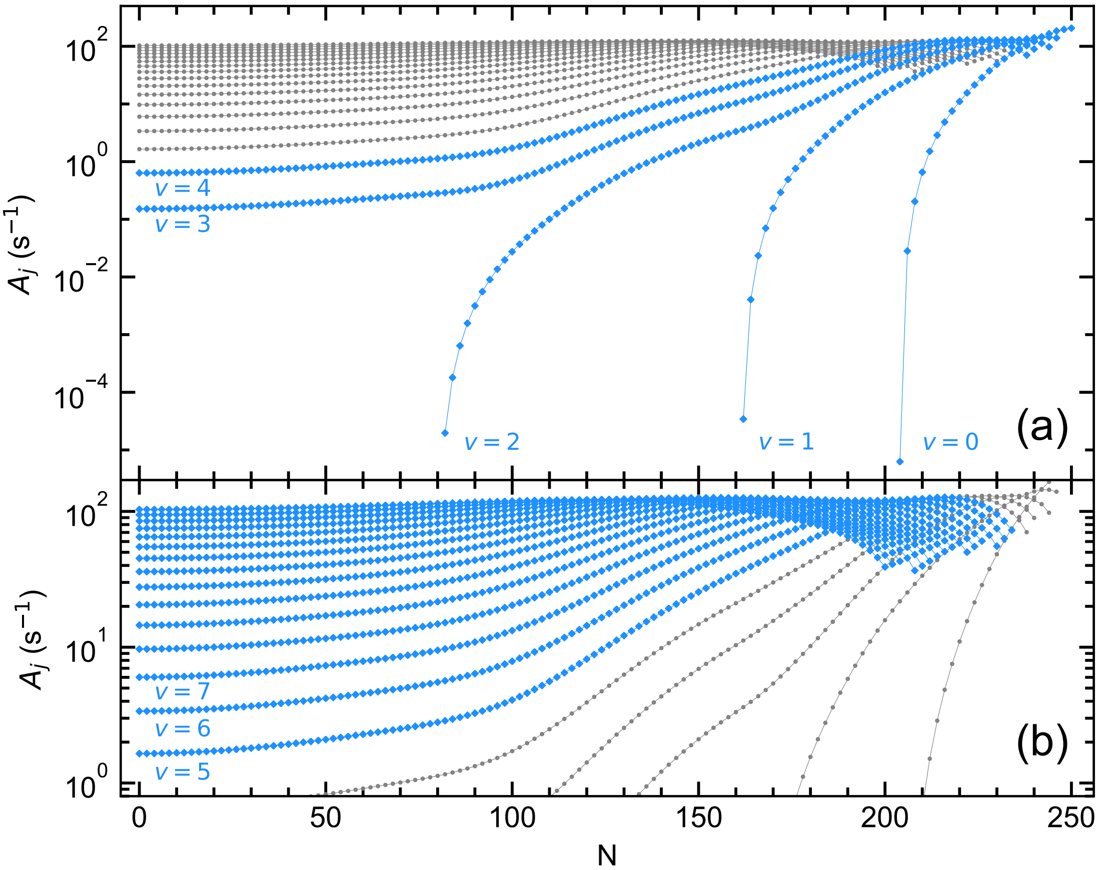

Figure 4.6: Radiative decay rates for the first 20 vibrational levels in the $X^2\Sigma_g^+$ state plotted versus the rotational excitation N. (a) Focus on the first five vibrational states, (b) Zoom into levels with $v > 4$. Unlabelled lines correspond to continuously increasing vibrational excitations from $v = 8$ to $v = 19$.

levels. The addition of rotational excitation to the potential curves creates a more shallow potential, reducing the number of bound vibrational levels (see Fig. 4.4). This effect occurs in both electronic states simultaneously. Here, the reduction of levels in the $A^2\Pi_u$ state leads to lower A_j at high N. Meanwhile, a lower number of bound vibrational levels in the $X^2\Sigma_g^+$ state is visible through the decreasing number of A_j rates at high rotational excitations in Fig. 4.6. For $N > 252$, no more vibrational levels are available.

The radiative decay rates for vibrational excitations $v = 3 - 10$ at $N = 0$ are compared to the previous calculation by Rosmus and Werner [12] in Tab. 4.4. The A_j derived in this work are smaller than the previous values by an average factor of ~ 3.1. A closer look into the results presented in [12] reveal that the authors

Table 4.3: Selection of radiative decay rates for the first 5 vibrational levels in the $X^2\Sigma_g^+$ state at different values of N in s^{-1}. Rates marked with a "*" represent the opening of the radiative decay channel for the specific v.

$N \backslash v$	0	1	2	3	4	5
0	-	-	-	1.5×10^{-1}	6.3×10^{-1}	1.6
50	-	-	-	2.0×10^{-1}	8.3×10^{-1}	2.1
82	-	-	2.0×10^{-5}*	2.9×10^{-1}	1.2	2.9
100	-	-	2.7×10^{-2}	4.8×10^{-1}	1.7	4.1
150	-	-	2.1	6.9	1.5×10^{1}	2.6×10^{1}
162	-	3.4×10^{-5}*	3.6	1.1×10^{1}	2.3×10^{1}	3.7×10^{1}
204	6.3×10^{-6}*	2.2×10^{1}	4.9×10^{1}	7.6×10^{1}	9.8×10^{1}	1.1×10^{2}
230	1.1×10^{2}	1.3×10^{2}	1.3×10^{2}	1.0×10^{2}	7.0×10^{1}	-

Table 4.4: Comparison of the radiative decay rates of vibrational levels $v = 3 - 10$ in the $X^2\Sigma_g^+$ state with no rotational excitation derived in this work with results by Rosmus and Werner [12]. In the last row, the rates from [12] are scaled to compensate the underestimated excitation energy, for details see text. Values are given in s^{-1}.

$\backslash v$	3	4	5	6	7	8	9	10
This work	0.15	0.63	1.6	3.4	6.0	9.7	1.5×10^{1}	2.1×10^{1}
[12]	0.5	1.8	4.9	1.0×10^{1}	1.8×10^{1}	2.9×10^{1}	4.3×10^{1}	6.3×10^{1}
[12] scaled	0.12	0.64	2.0	4.8	9.2	1.6×10^{1}	2.4×10^{1}	3.9×10^{1}

underestimated the excitation energy of the first excited state $A^2\Pi_u$. This is also evident in Tab. 4.1, where this value calculated by Rosmus and Werner is significantly smaller than those given in other publications. The energetic separation between the initial and final state of the radiative transition enters to the third power into the rate calculations (see Eq. (4.7)). Due to the small ν in the transitions considered here, the discrepancy in excitation energy strongly influences the rate calculations. To estimate this effect, the results by Rosmus and Werner are scaled in the last row of Tab. 4.4. To this end, the explicit values of the energetic separation ($\tilde{\nu}_{a'}^{b''}$) for all partial decays of an initial level a' to all possible final levels b'' were calculated. This calculation was once carried out for the potentials employed in this work and once using the spectroscopic parameters given in [12] (see Tab. 4.1) for the Rosmus and Werner calculations. Afterwards, the ratio between $\tilde{\nu}_{a'}^{b''}$ derived for the Rosmus and Werner results and the energy difference derived in this work were calculated and

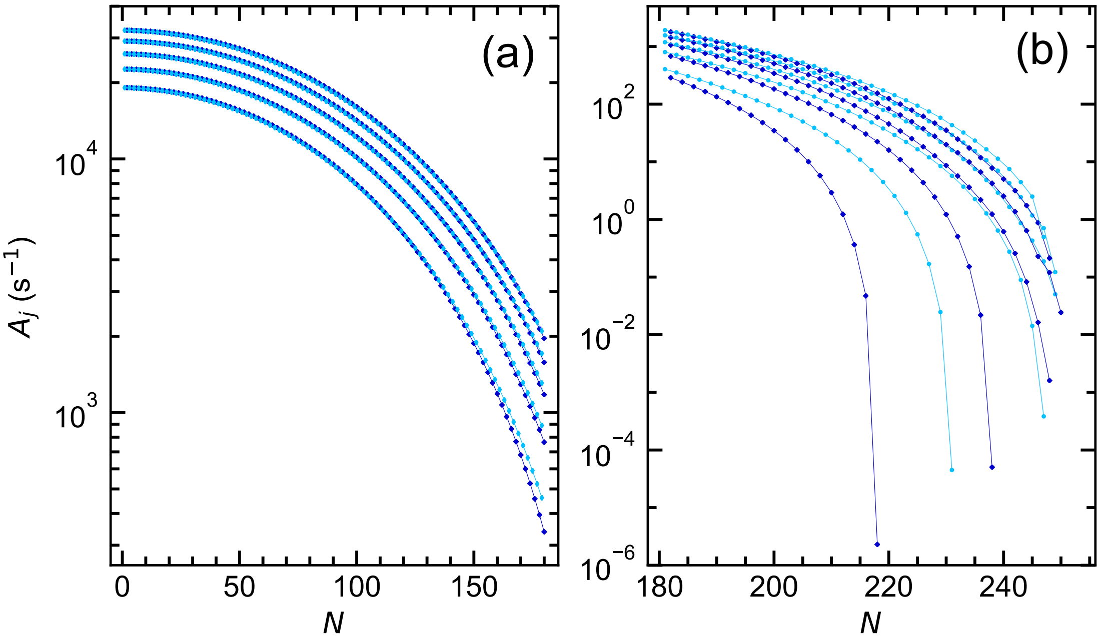

Figure 4.7: Radiative decay rates for the first five vibrational levels in the $\mathrm{A}^2\Pi_u$ state are plotted versus the rotational excitation N. Here, increasing vibrational excitations have larger A_j. Rates corresponding to levels with $\epsilon_N = -1/\epsilon_N = +1$ have an even/odd rotational excitation and are drawn in dark/light blue. Levels with the same v and ϵ_N values are connected with a thin line. The figure is split into two N regions with sub-figure (a)/(b) showing rates with $N \leq 180/N > 180$.

an average scaling factor for each initial state a' was derived. The rates given in [12] were then scaled by this factor to the third power in accordance with Eq. (4.7). The resulting values are given in the bottom row of Tab. 4.4. The average factor between these rates and the ones derived in this work reduced to ~ 1.4 with this simple approximation. Since no partial decay rates were given in [12], a more precise scaling procedure of the radiative decay rates was not possible. The residual difference between the rates given in [12] and the ones calculated here can furthermore be explained by potentially differing vibrational overlaps between initial and final states as well as the slightly different $\boldsymbol{\mu}(R)$ (see Fig. 4.5).

Results for the radiative decay from the $\mathrm{A}^2\Pi_\mathrm{u}$ state

The first excited $\mathrm{A}^2\Pi_u$ state of C_2^- supports both even and odd rotational excitations. Due to the Pauli principle, these exclusively correspond to $\epsilon_N = -1$ and $\epsilon_N = 1$, respectively (see Sec. 4.2.3). Vibrational levels in this state can decay radiatively to

Table 4.5: Total radiative decay rates for the first 5 vibrational levels in the $A^2\Pi_u$ state at selected values of N in s^{-1}. Rates for even/odd values of N correspond to states with $\epsilon_N = -1/\epsilon_N = +1$.

$N \backslash v$	0	1	2	3	4	5
1	1.9×10^4	2.3×10^4	2.6×10^4	2.9×10^4	3.2×10^4	3.5×10^4
2	1.9×10^4	2.3×10^4	2.6×10^4	2.9×10^4	3.2×10^4	3.5×10^4
49	1.6×10^4	1.9×10^4	2.2×10^4	2.5×10^4	2.8×10^4	3.0×10^4
50	1.6×10^4	1.9×10^4	2.2×10^4	2.5×10^4	2.7×10^4	3.0×10^4
99	8.3×10^3	1.1×10^4	1.3×10^4	1.5×10^4	1.7×10^4	1.8×10^4
100	8.0×10^3	1.0×10^4	1.2×10^4	1.4×10^4	1.6×10^4	1.8×10^4
149	2.2×10^3	3.3×10^3	4.3×10^3	5.2×10^3	6.1×10^3	7.0×10^3
150	1.9×10^3	2.9×10^3	3.9×10^3	4.8×10^3	5.7×10^3	6.5×10^3
199	1.2×10^2	3.0×10^2	4.9×10^2	6.8×10^2	8.7×10^2	1.1×10^3
200	3.5×10^1	1.8×10^2	3.4×10^2	5.1×10^2	6.7×10^2	8.3×10^2
239	-	1.3	4.8	1.1×10^1	1.6×10^1	2.1×10^1
240	-	-	6.2×10^{-1}	2.5	5.0	7.1

lower-lying levels in the ground state of the system, where only even N are populated. Consequentially, levels in $A^2\Pi_u$ with even rotational excitation ($\epsilon_N = -1$) can decay by $\Delta N = 0$ only. Meanwhile, levels with odd rotational excitation ($\epsilon_N = 1$) decay with $\Delta N = \pm 1$. As a result, $\epsilon_N = 1$ levels have twice as many final states available for the radiative decay than $\epsilon_N = -1$ levels, neglecting the rotational dependence of the number of lower-lying vibrational levels at high N. However, the degeneracy factor in Eq. (4.16) is approximately twice as large for transitions with $\Delta N = 0$ than those with $\Delta N = \pm 1$. Therefore, at low rotational excitations, where the addition of the centrifugal energy to the potential (see Eq. 4.6) only negligibly changes the energies of the vibrational levels, A_j values for consecutive even and odd rotational excitations are approximately equal.

The total radiative decay rates for levels in the $A^2\Pi_u$ state were calculated according to the procedure outlined in the beginning of this Sec. 4.3.2 and employing Eq. (4.16). Results for the first five vibrational levels are plotted versus N in Fig. 4.7. Rates corresponding to even/odd rotational excitations are drawn in dark/light blue. The figure is split into two sub-figures, corresponding to rotational excitation ranges $N \leq 180$ and $N > 180$ to provide a better overview. Values of A_j for $v < 6$ and a selection of N are listed in Tab. 4.5. General trends of A_j with increasing rotational excitations displayed both in Fig. 4.7 and Tab. 4.5 are caused by the effects of the centrifugal energy term on the potential curves. As discussed in Sec. 4.2.3, the ZPE of the $A^2\Pi_u$ state moves closer to and eventually below the ZPE of the $X^2\Sigma_g^+$ state with increasing N. Here, the ZPE is defined as the energy of the lowest vibrational

Table 4.6: Comparison of radiative decay rates the first ten vibrational levels in the $A^2\Pi_u$ state for no rotational excitation derived in this work with literature values [12, 15]. For the results by Shi et al. [15], two rates are given one with and one without a degeneracy factor. In the row marked with a "*", rates including this factor are listed. Values are given in s^{-1}.

$\backslash v$	0	1	2	3	4	5
This work	1.9×10^4	2.3×10^4	2.6×10^4	2.9×10^4	3.2×10^4	3.5×10^4
[12]	2.0×10^4	2.5×10^4	2.9×10^4	3.3×10^4	3.6×10^4	4.0×10^4
[15]	1.9×10^4	2.3×10^4	2.6×10^4	3.0×10^4	3.3×10^4	3.6×10^4
[15]*	3.7×10^4	4.5×10^4	5.3×10^4	6.0×10^4	6.7×10^4	7.3×10^4

level ($v = 0$) in the rotating potential $V_N(R)$ (see Eq. (4.6)). For the transitions considered here, this leads to a decrease of A_j with rotational excitations due to two effects. One is the decrease in energetic separation between initial and final level of the radiative transition which enters the rate calculations to the third power (see Eq. (4.7)). The other is the reduction of available final levels to decay to as the two electronic states start to rearrange. Latter effect also leads to the eventual radiative stability of the lowest three vibrational levels at sufficiently high N. Higher vibrations are no longer bound in the increasingly shallow potential at high rotational excitations at the point where they would become radiatively stable.

The rotational excitations in Tab. 4.5 are chosen such that pairs of consecutive even/odd N are given. Differences in rates within such pairs are negligibly small for low rotational excitations (see discussion at the beginning of this sub-section). However, the differences increase with increasing N. Notably, A_j values corresponding to $\epsilon_N = -1$ levels are smaller than their $\epsilon_N = 1$ counterparts. This can be explained by the availability of only even N in the $X^2\Sigma_g^+$ state. At high rotational excitation the potentials corresponding to N and $N+1$ differ significantly in energy. Consequentially, transition with $\Delta N = -1$, available only for levels with $\epsilon_N = 1$, have higher rates than those with $\Delta N = 0$ accessible for $\epsilon_N = -1$ levels. The resulting separation of A_j corresponding to odd or even rotational excitations becomes more pronounced as N increases. This is also visible in Fig. 4.7. Furthermore, the energetic rearrangement with the $X^2\Sigma_g^+$ state happens at larger N values for transitions with $\Delta N = -1$. Therefore, $\epsilon_N = 1$ levels become radiatively stable at higher rotational excitations then $\epsilon_N = -1$ levels of the same vibrational excitation.

The radiative decay rates of the first six vibrational levels without rotational excitation are compared to literature values in Tab. 4.6. Here, the agreement with the results of Rosmus and Werner [12] are much better than for the $X^2\Sigma_g^+$ state. A_j of vibrational levels v' in the $A^2\Pi_u$ state are dominated by the partial rates corresponding to final levels $v'' \approx v'$. This is different to the decay of levels in the

$X^2\Sigma_g^+$ state, which are dominated by the decay into the highest vibrational final level available [71, 19]. Consequentially, the relevant energy separation between initial and final state for transitions from $A^2\Pi_u$ to $X^2\Sigma_g^+$ are larger and therefore less sensitive to the excitation energy deviation in the calculations presented in [12]. This leads to a better agreement with the rates derived in this work. Tab. 4.6 furthermore lists the A_j values given by Shi et al. [15], once including and once excluding a degeneracy factor in the calculations (see discussion in Sec. 4.3.1). The rates excluding the degeneracy factor are in an even better agreement with the ones calculated here than the those by Rosmus and Werner. On the other hand, the values derived with the degeneracy factor differ by at least a factor of 1.8 from the other calculations.

4.3.3 Radiative relaxation of the $C^4\Sigma_u^+$ quartet state

According to the selection rules outlined in the beginning of this Sec. 4.3, the spin-allowed radiative decay of the $C^4\Sigma_u^+$ state of C_2^- requires the presence of a lower-lying quartet state of *gerade* symmetry. However, while calculations by Shi et al. [15] did identify a $^4\Sigma_g$ state in the system, the authors found its position to lie multiple eV above the state considered here. Hence, the spin-allowed decay of the lowest-lying quartet state of C_2^- is not possible.

In the absence of adequate quartet states to decay into, the $C^4\Sigma_u^+$ state only has the three lower-lying doublet states available for radiative relaxation. Out of these only one, the $X^2\Sigma_g^+$ ground state, has the required *gerade* symmetry. Due to the different spins ($S = 3/4$ for $C^4\Sigma_u^+$ and $S = 1/2$ for $X^2\Sigma_g^+$), the coupling between the initial and final state is enabled through spin-orbit (SO) coupling alone. As the name suggests, this effect is caused by the coupling between the electron spin $\hat{S}$ and the angular momentum of the electronic orbit $\hat{L}$. The moving electronic charges, in form of the electrons' motion inside the orbital, result in a current which in turn induces a magnetic field. This field influences the orientation of the electrons' magnetic moment which encodes the spin state of the system. This coupling between $\hat{L}$ and $\hat{S}$ is described by the spin-orbit operator $\hat{H}_{so}$ [77]. Due to this effect, neither the spin nor the orbital angular momentum are conserved in the system and therefore are no longer "good" quantum numbers. Merely quantities including the sum of both, the total angular momentum $\hat{J} = \hat{L} + \hat{S} + \hat{R}$, its scalar J and its projection onto the internuclear axis Ω, are conserved. SO coupling only influences the angular momenta of the system but not its overall parities (see Sec. 4.2.1).

For levels a' in the $C^4\Sigma_u^+$ state, SO coupling is only possible to levels $\bar{c}$ in other *ungerade* states. These must additionally meet the requirements $J' = \bar{J}$ and $\Omega' = \bar{\Omega}$, where $\Omega = \Sigma + \Lambda$ (see Sec. 4.2.1), since both J and Ω are conserved quantities. Consequentially, SO coupling is only possible with the $A^2\Pi_u$ state. This small admixture of a state with a spin-allowed transition to the $X^2\Sigma_g^+$ ground state (see Sec. 4.3.2) enables the radiative relaxation of the $C^4\Sigma_u^+$ state. The mathematical

Table 4.7: Overview of the quantum numbers of the $C^4\Sigma_u^+$, $A^2\Pi_u$, and $X^2\Sigma_g^+$ states relevant for the calculation of the spin-forbidden decay of $C^4\Sigma_u^+$.

	$C^4\Sigma_u^+$ ($\|a'\rangle$)	$A^2\Pi_u$ ($\|\bar{c}\rangle$)	$X^2\Sigma_g^+$ ($\|b''\rangle$)
S	3/2	1/2	1/2
Σ	±1/2, ± 3/2	± 1/2	±1/2
Λ	0	±1	0
$\Omega(=\Lambda+\Sigma)$	±1/2, ± 3/2	±1/2, ± 3/2	±1/2

derivation and calculation of this decay process were carried out by Apl. Prof. Dr. Andreas Wolf, Max-Planck-Institut für Kernphysik. They are given in detail in Appendix B2 in [90] and will be summarized below.

Based on the considerations outlined above, levels a' in the $C^4\Sigma_u^+$ state radiatively decay to levels b'' in the $X^2\Sigma_g^+$ ground state by coupling to levels $\bar{c}$ in the $A^2\Pi_u$ state. Therefore, Eq. (4.8), which describes the coupling between initial state a' and final state b' can be rewritten to

$$\sqrt{S_{a'}^{b''}} = \langle a'|\,\mu_{eff}\,|b''\rangle = \sum_{\bar{c}} \frac{\langle a'|\,\hat{H}_{so}\,|\bar{c}\rangle}{E_{a'} - E_{\bar{c}}} \times \langle \bar{c}|\,\mu_{eff}\,|b''\rangle\,. \tag{4.17}$$

Here, the first term in the sum describes the perturbation of initial state a' by $\bar{c}$, with $E_{a'}$ and $E_{\bar{c}}$ the respective energies of the states. The coupling operator $\hat{H}_{so}$ describes the spin-orbit coupling. The second term describes the decay of $\bar{c}$ into the final state b''. Here, the coupling operator μ_{eff} is the one shown in Fig. 4.5 describing the coupling between $X^2\Sigma_g^+$ and $A^2\Pi_u$. Since there can be a number of intermediate state $\bar{c}$, it is necessary to sum over all these to describe the decay from a' to b''.

The electronic states involved here can all be classified as Hund's case (b) states $|Nv\Lambda J\rangle$. Even though this indicates that the SO coupling is weak, it is still relevant for the decay of levels in $C^4\Sigma_u^+$ due to the absence of other available channels. In the case of the $A^2\Pi_u$ state, where a spin-allowed transition is available for de-excitation, SO coupling has a negligible influence on the total radiative lifetime. While the states are all categorized as Hund's case (b), it is advantageous to expand these in the basis set of Hund's case (a) states $|Nv\Lambda\Omega\rangle$ to describe SO coupling. To this end, Eq. (29) in [86] can be used:

$$|Nv\Lambda J\rangle = \sum_{\Sigma\Lambda} \sqrt{(2N+1)}(-1)^{J+\Omega} \begin{pmatrix} S & N & J \\ \Omega-\Lambda & \Lambda & -\Omega \end{pmatrix} |Nv\Lambda\Omega\rangle\,, \tag{4.18}$$

where the matrix in the brackets is a 3j-Wigner symbol [89]. In order to enable a more concise writing of the following equations, the pre-factor in Eq. (4.18) will be summarized from here on as

$$r_{N\Omega}^{\Lambda JS} = \sqrt{(2N+1)}(-1)^{J+\Omega}\begin{pmatrix} S & N & J \\ \Omega-\Lambda & \Lambda & -\Omega \end{pmatrix}. \tag{4.19}$$

For the three states considered for this decay, $C^4\Sigma_u^+$, $A^2\Pi_u$, and $X^2\Sigma_g^+$, the values in Tab. 4.7 can be used to expand the states according to Eqs. (4.18) and (4.19) as follows:

$$\begin{aligned} |N'v'0J'\rangle &= \sum_{\Omega'=\pm\frac{1}{2},\pm\frac{3}{2}} r_{N'\Omega'}^{0J'\frac{3}{2}} |N'v'0\Omega'\rangle, && C^4\Sigma_u^+ \\ |\bar{N}\bar{v}\bar{\Lambda}\bar{J}\rangle &= \sum_{\substack{\bar{\Omega}=\pm\frac{1}{2},\pm\frac{3}{2} \\ \bar{\Lambda}=\pm 1}} r_{\bar{N}\bar{\Omega}}^{\bar{\Lambda}\bar{J}\frac{1}{2}} |\bar{N}\bar{v}\bar{\Lambda}\bar{\Omega}\rangle, && A^2\Pi_u \\ |N''v''0J''\rangle &= \sum_{\Omega''=\pm\frac{1}{2}} r_{N''\Omega''}^{0J''\frac{1}{2}} |N''v''0\Omega''\rangle. && X^2\Sigma_g^+ \end{aligned} \tag{4.20}$$

The first term in the sum of Eq. (4.17) can then be expanded to

$$\frac{\langle a'|\,\hat{H}_{so}\,|\bar{c}\rangle}{E_{a'}-E_{\bar{c}}} = \sum_{\substack{\Omega'=\pm\frac{1}{2},\pm\frac{3}{2} \\ \bar{\Lambda}=\pm 1}} r_{N'\Omega'}^{0J'\frac{3}{2}} r_{\bar{N}\Omega'}^{\bar{\Lambda}J'\frac{1}{2}} \frac{\langle N'v'0\Omega'|\,\hat{H}_{so}\,|\bar{N}\bar{v}\bar{\Lambda}\Omega'\rangle}{E_{a'}-E_{\bar{c}}}, \tag{4.21}$$

taking into account that $\langle a'|\,\hat{H}_{so}\,|\bar{c}\rangle = 0$ for $\Omega' \neq \bar{\Omega}$ and $J' \neq \bar{J}$. The spin-orbit matrix element can be calculated analogous to the dipole matrix element of the spin-allowed transition described by Eq. (4.11) by integrating over the convolution of the initial and final vibrational wavefunctions with the corresponding coupling function over R. It will from now on be written as

$$\hat{A}_{\Omega'}^{ac}(N',v',\bar{N},\bar{v}) \equiv \langle N'v'0\Omega'|\,\hat{H}_{so}\,|\bar{N}\bar{v}\bar{\Lambda}\Omega'\rangle = \int \psi_{a'}(R)^*\hat{A}_{\Omega'}^{ac}(R)\psi_{\bar{c}}(R)dR. \tag{4.22}$$

The four SO coupling functions $\hat{A}_{\Omega'}^{ac}(R)$ with $\Omega' \in \left\{-\frac{3}{2},-\frac{1}{2},\frac{1}{2},\frac{3}{2}\right\}$ were calculated using the results of the *ab initio* calculations carried out by Ass. Prof. Dr. Milan Ončák, Innsbruck University (see Eqs. (25) - (27) in [90]). These were found to fulfil the following relations:

$$\begin{aligned} \hat{A}_{-\Omega'}^{ac}(R) &= -\hat{A}_{\Omega'}^{ac}(R), \\ \hat{A}_{1/2}^{ac}(R) &= \frac{1}{\sqrt{3}}\hat{A}_{3/2}^{ac}(R). \end{aligned} \tag{4.23}$$

The SO coupling function $\hat{A}_{3/2}^{ac}(R)$ ($\Omega' = 3/2$) is plotted exemplarily in Fig. 4.8.

The second term in Eq. (4.17) describes the spin-allowed transition $A^2\Pi_u$ - $X^2\Sigma_g^+$. Here, the selection rule of $\bar{\Sigma} = \Sigma''$ applies. Taking into account the relation between

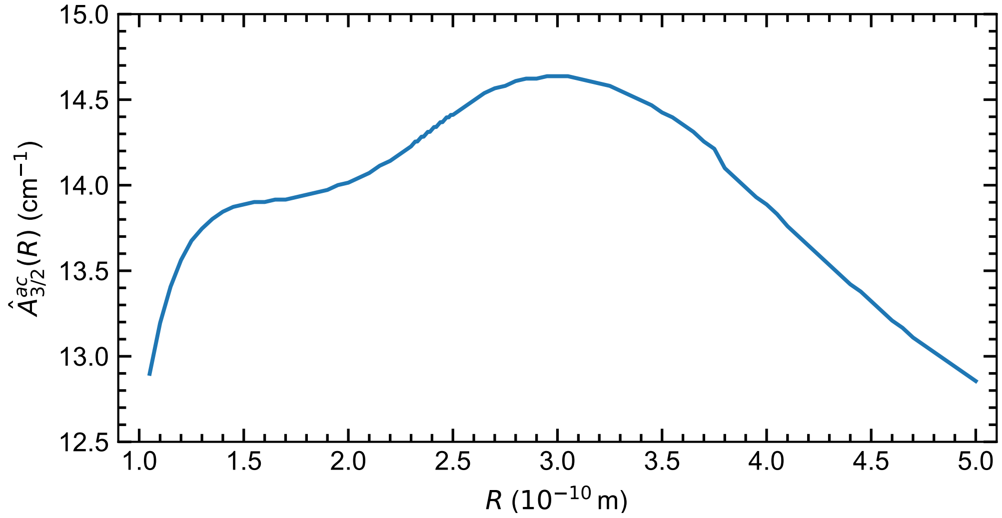

Figure 4.8: Spin-orbit coupling function $\hat{A}^{ac}_{3/2}(R)$ between the $C^4\Sigma_u^+$ and $A^2\Pi_u$ states of C_2^- for $\Omega' = 3/2$.

Ω and Σ as well as the quantum numbers of the respective states (see Tab. 4.7) and the condition $\bar{\Omega} = \Omega'$ from the SO coupling, this directly results in the condition

$$\Omega' = \Omega'' + \bar{\Lambda}. \tag{4.24}$$

Considering this, the second term in Eq. (4.17) can also be expanded using Eq. (4.20) above as well as Eq. (13) in [87] to

$$\begin{aligned}\langle \bar{c}|\, \mu_{eff}\, |b''\rangle = \sum_{\substack{\Omega''=\pm\frac{1}{2}\\ \bar{\Lambda}=\pm 1}} \sqrt{(2J'+1)(2J''+1)}(-1)^{J'-\Omega''-\bar{\Lambda}} \begin{pmatrix} J' & 1 & J'' \\ -\Omega''-\bar{\Lambda} & \bar{\Lambda} & \Omega'' \end{pmatrix} \\ \times\, r^{\bar{\Lambda}J'\frac{1}{2}}_{\bar{N}(\Omega''+\bar{\Lambda})}\, r^{0J''\frac{1}{2}}_{N''\Omega''}\, \mu^{\bar{c}b''}_{\bar{\Lambda}}(\bar{N},\bar{v},N'',v''),\end{aligned} \tag{4.25}$$

with the conditions $\Omega' = \bar{\Omega}$ and $J' = \bar{J}$ of the SO coupling included. The pre-factor in the first line of Eq. (4.25) will be substituted by

$$s^{J'J''}_{\Omega''\bar{\Lambda}} = \sqrt{(2J'+1)(2J''+1)}(-1)^{J'-\Omega''-\bar{\Lambda}} \begin{pmatrix} J' & 1 & J'' \\ -\Omega''-\bar{\Lambda} & \bar{\Lambda} & \Omega'' \end{pmatrix}, \tag{4.26}$$

from here on.

Inserting Eqs. (4.21), (4.22), (4.25), and (4.26) into Eq. (4.17), the line strength from an initial state a' in $C^4\Sigma_u^+$ to a final state b'' in $X^2\Sigma_g^+$ through SO coupling with pertubator levels $\bar{c}$ in $\mathrm{A}^2\Pi_u$ can be written as

$$\begin{aligned} S_{N'v'J'}^{N''v''J''} = |\,\langle a'|\,\mu_{eff}\,|b''\rangle\,|^2 = \Bigg[& \sum_{\substack{\Omega''=\pm\frac{1}{2} \\ \bar{\Lambda}=\pm 1}} r^{0J'\frac{3}{2}}_{N'(\Omega''+\bar{\Lambda})}\, r^{0J''\frac{1}{2}}_{N''\Omega''}\, s^{J'J''}_{\Omega''\bar{\Lambda}} \sum_{\bar{N}\bar{v}} \left(r^{\bar{\Lambda}J'\frac{1}{2}}_{\bar{N}(\Omega''+\bar{\Lambda})} \right)^2 \\ & \times \frac{\hat{A}^{ac}_{\Omega''+\bar{\Lambda}}(N',v',\bar{N},\bar{v})}{E_{a'}-E_{\bar{c}}}\;\mu^{\bar{c}b''}_{\bar{\Lambda}}(\bar{N},\bar{v},N'',v'') \Bigg]^2 \end{aligned} \tag{4.27}$$

To obtain the total radiative decay rate $A_{N'v'J'}$ of an initial state $|N'v'J'\rangle$ in $\mathrm{C}^4\Sigma_u^+$, Eq. (4.27) can be inserted into Eq. (4.7) and the sum over all possible final states can be derived according to Eq. (4.9).

Results for the radiative decay from the $\mathrm{C}^4\Sigma_\mathrm{u}^+$ state

The radiative decay rates for levels in the $\mathrm{C}^4\Sigma_u^+$ state were calculated by Apl. Prof. Dr. Andreas Wolf, Max-Planck-Institut für Kernphysik. The results are shown in Fig. 4.9. The four pannels show the fine-structure sublevels F1 ($J' = N' + \frac{3}{2}$), F2 ($J' = N' + \frac{1}{2}$), F3 ($J' = N' - \frac{1}{2}$), F4 ($J' = N' - \frac{3}{2}$). Solid, dashed and dotted lines connect rates corresponding to vibrational excitations $v = 0, 5, 10$, respectively. Only levels with large N values are shown, since those with small rotational excitation exhibit insufficient auto-detachment lifetimes to contribute to the signals measured in the experiment (see Sec. 4.5.3).

The calculated rates span over more than five orders of magnitude and fluctuate strongly between different rotational and vibrational excitations. This effect can be understood by taking a closer look at the SO coupling. It was found that the perturbation of levels in $\mathrm{C}^4\Sigma_u^+$ is dominated by the coupling to the energetically closest-lying level in the $\mathrm{A}^2\Pi_u$ state. This leads to small energy differences $E_{a'} - E_{\bar{c}}$ in the denominator in Eq. (4.27). Consequentially, the decay rates are very sensitive to variations in the energetic separation between the initials levels and their closest perturbator states, which vary for different initial excitations $N'v'$. Furthermore, a smaller effect on the rate variations are the different coupling strengths of the pertubator states to the $\mathrm{X}^2\Sigma_g^+$ ground state. As a result, the radiative decay rates show neither clear rotational nor vibrational excitation-dependent trends.

Additionally, decay rates for the fine-structure sub-levels can differ by multiple orders of magnitude for the same ro-vibrational excitation (N', v'), see Fig. 4.9. As discussed in the beginning of this Sec. 4.3.3, SO coupling is only possible between states with the same Ω and J. Due to the different spins S and angular orbitals Λ of the initial $\mathrm{C}^4\Sigma_u^+$ and pertubator $\mathrm{A}^2\Pi_u$ states, the four fine-structure sub-levels in the quartet state couple to different rotational excitations $\bar{N}$ in the $\mathrm{A}^2\Pi_u$. Consequentially, different perturbator states enable the radiative decay for the four sub-levels, which then have strongly differing A_j. This is significant, because only a small number of ro-vibrational excitations (N', v') in the $\mathrm{C}^4\Sigma_u^+$ state have sufficiently long AD

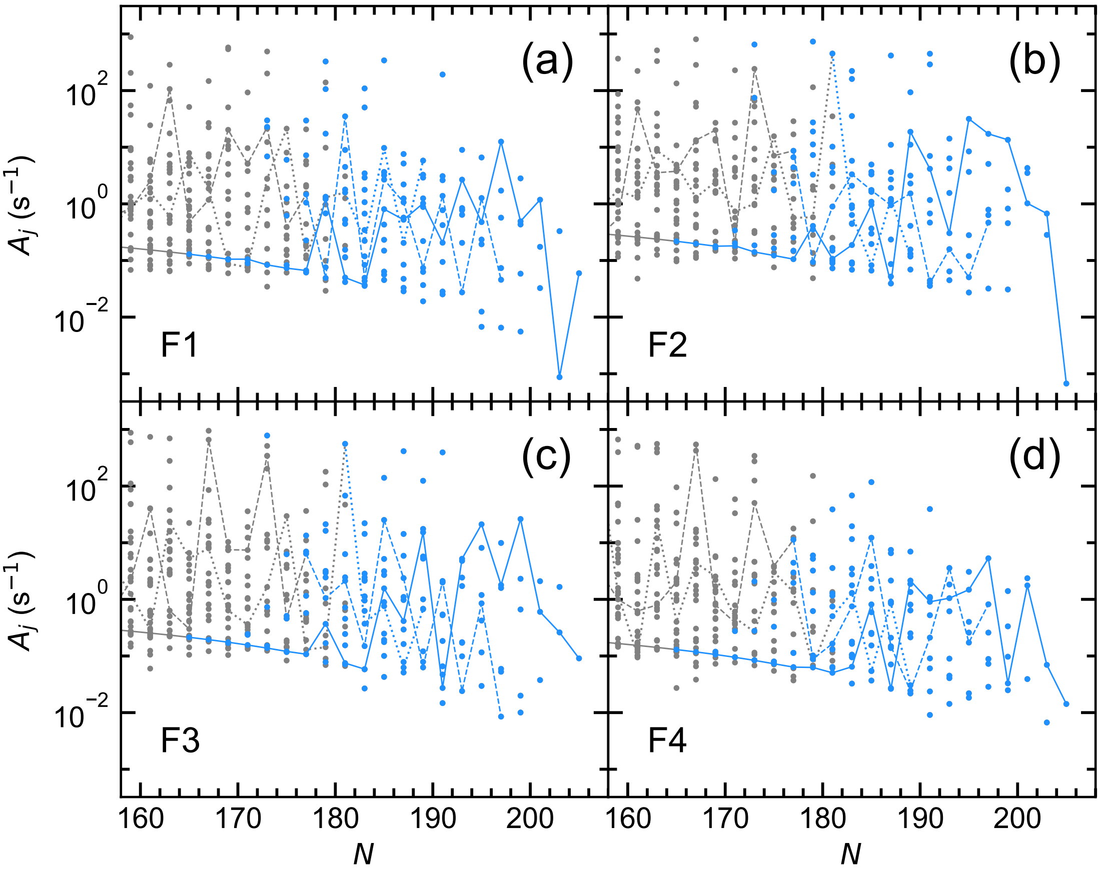

Figure 4.9: Radiative decay rates for levels in the $C^4\Sigma_u^+$ state. The four subfigures correspond to the fine-structure sublevels (a) F1 ($J' = N' + 3/2$), (b) F2 ($J' = N' + 1/2$), (c) F3 ($J' = N' - 1/2$), (d) F4 ($J' = N' - 3/2$). Solid, dashed, and dotted lines connect selected vibrational levels with $v = 0, 5, 10$, respectively. Rates drawn in grey can auto-detach to the neutral $A^3\Pi_u$ state with a change of rotational excitation of $\Delta N \leq 4$. For rates drawn in blue, only AD with $\Delta N > 4$ is available.

lifetimes to contribute to the measured signals (see Sec. 4.5.3). Due to the strong fluctuation of A_j, even a set of sub-levels typically exhibits very different total decay rates (combined decay of the level considering all available channels). These rates in turn define the contribution of the levels to the measured AD and AF signals.

The rates displayed in Fig. 4.9 are colour-coded according to their stability with respect to auto-detachment. Here, grey dots correspond to levels for which a detachment channel into the neutral $A^3\Pi_u$ state with a maximum change in rotational excitation of $(\Delta N)_{\max} = 4$ is available. For those drawn in blue, AD is only possible with $\Delta N > 4$. As will be discussed in more detail in Sec. 4.5.3, merely latter lev-

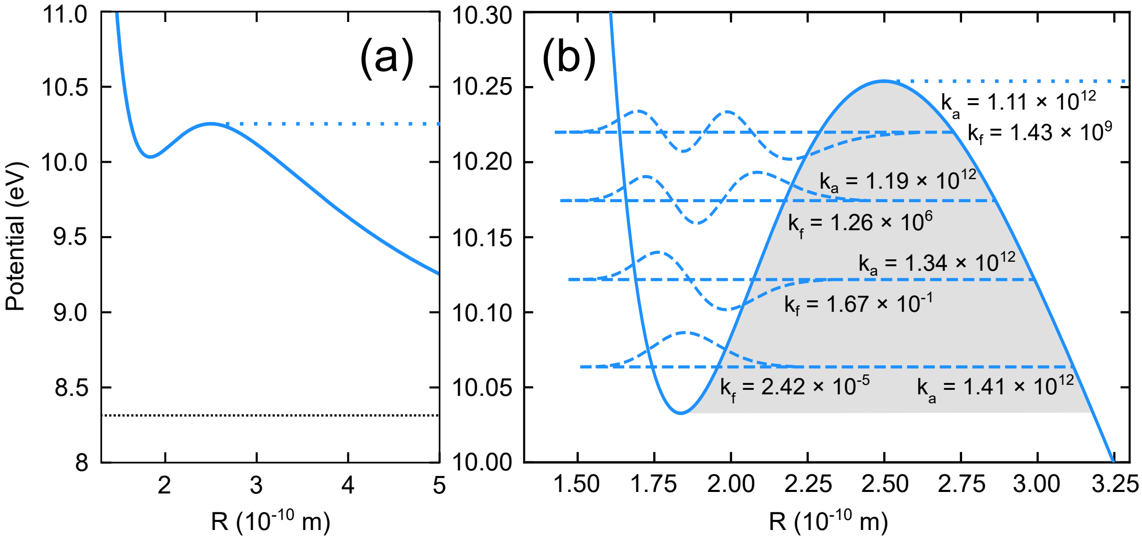

Figure 4.10: AF in vibrational levels in the $A^2\Pi_u$ state of C_2^- for rotational excitation $N = 249$. (a) Potential curve shown in blue with the dissociation threshold of C_2^- at 8.41 eV indicated with a black horizontal dotted line. (b) Zoom into the region of the fragmentation resonances. Four metastable vibrational levels and their wavefunctions are drawn in dashed lines. Their attempt frequencies k_a and dissociation rates k_f are given. A blue horizontal dotted line indicates the modified potential with $E(R \geq R_{\mathrm{cb,max}}) = E_{\mathrm{cb,max}}$ to calculate the energy of high-lying vibrational levels.

els are relevant for the description of the experimental signal presented in Sec. 4.1. The lowest energetic vibrational level meeting this criteria is $v = 0$ for rotational excitations $N = 165$. For $N > 181$, all vibrational levels are stable against AD with $\Delta N \leq 4$. The number of plotted A_j deceases with increasing N due to the reduction of vibrational levels at high rotational excitations due to the increasingly shallow potential. In contrast to the radiative rates derived in Sec. 4.3.2, no published values are available for the A_j shown in Fig. 4.9. Therefore, a comparison with literature is not possible here.

4.4 Auto-fragmentation rates

Auto-fragmentation (AF) of homo-nuclear anionic dimers has been observed and described for other systems, most notably by Fedor et al. for Cu_2^- and Ag_2^- [5]. The theoretical considerations to estimate the AF rates used in this publication is the basis for the calculations presented in this section and will be shortly summarized below.

As briefly mentioned in Sec. 4.2.3, the addition of the centrifugal energy term to the rotationless *ab initio* potential curves causes the formation of a rotational barrier at sufficiently high values of N. An example of this can be seen in the inset of Fig. 4.4(c) for the lowest two electronic states of the system at $N = 248/249$. Fig. 4.10 shows the potential curve for rotational excitation $N = 249$ of the $\mathrm{A}^2\Pi_u$ state. The dashed, black horizontal line in subfigure (a) marks the dissociation threshold at $D_0 = 8.41\,\mathrm{eV}$. In the plotted R-range, the potential lies more than 1 eV above the threshold for any internuclear distance. Additionally, the equilibrium distance has moved to a value of about 1.84 Å compared to 1.31 Å for $N = 0$ (see Tab. 4.1). In Fig. 4.10(b) the potential region which supports metastable vibrational states is shown. Four such fragmentation resonances are present in the exemplary case shown here. Their dissociation rates k_f are calculated via the product of their tunnelling probability P_t through the rotational barrier and the corresponding attempt frequency k_a [5]

$$k_f = k_a P_t. \tag{4.28}$$

In accordance with the calculations performed by Fedor et al., P_t is approximated using the Wentzel-Brillouin-Kramers (WKB) approximation

$$P_t = \exp\left(-\frac{\sqrt{8\mu}}{\hbar}\int_{R_1}^{R_2}\sqrt{V_N(R) - D_0}\,dR\right). \tag{4.29}$$

Here, $V_N(R)$ is the potential curve for rotational excitation N (see Eq. (4.6)), D_0 is the dissociation threshold and R_1 and R_2 are the barrier's classical turning points. The attempt frequency k_a is approximated by using the average energy difference with respect to the vibrational levels directly below and above the level of interest. In the case, where the highest metastable vibrational level in the potential is considered, only the energy difference to the level below is used.

As described in previous Secs. 4.2 and 4.3, the vibrational levels are identified using the Numerov method [85]. This approach solves the Schrödinger equation for different excitation energies to find the eigenvalues ψ of the system. For each energy value, an integration region $R_{\mathrm{min}} - R_{\mathrm{max}}$ has to be defined. The end points R_{min} and R_{max} have to be chosen sufficiently far away from the classical turning points of the potential in order to approximate the boundary conditions of $\psi(R_{\mathrm{min}}) \approx \psi(-\infty) = 0$ and $\psi(R_{\mathrm{max}}) \approx \psi(\infty) = 0$. For the identification of fragmentation resonances it is additionally important to chose R_{max} such that is still inside the centrifugal barrier. As a result, vibrational levels situated right below the top of the centrifugal barrier, e.g., $v = 3$ of the $\mathrm{A}^2\Pi_u$ state at $N = 249$ shown in Fig. 4.10(b), can have insufficiently large values of R_{max}. For the identification of these levels, it is advantageous to use a modified potential for the Numerov algorithm. Here, the energy value $E_{\mathrm{cb,max}}$ at the highest point of the centrifugal barrier at internuclear distance $R_{\mathrm{cb,max}}$ is determined. The curve is then modified in such a way that for $R \geq R_{\mathrm{cb,max}}$ the potential is fixed as $E_{\mathrm{cb,max}}$, while for $R < R_{\mathrm{cb,max}}$ the values of $V_N(R)$ are used [90]. The modified potential for the example in Fig. 4.10 is indicated with a dotted blue line. This alteration results in a change of the identified vibrational level's excitation energy typically in the order of per mille. Consequentially, also the width and height of the potential barrier through which the level tunnels changes slightly. Due to the exponential dependence in Eq. (4.29), this typically leads to a deviation of the dissociation rate k_f by roughly $10\,\%$.

In the example shown in Fig. 4.10, general trends for the dissociation rates and attempt frequencies for vibrational levels within a potential can be observed. One is the decrease of k_a with increasing vibrational excitation. This is caused by the decreasing energy spacing of the levels with increasing v due to the unharmonicity of the potential. This effect, which in the example shown in Fig. 4.10 is about 20% between $v = 0$ and $v = 3$, is small compared to the change in k_f between the vibrational levels. Due to the exponential dependence of the dissociation rate on the integral of the centrifugal barrier (see Eqs. (4.28) and (4.29)), k_f increases by multiple orders of magnitude between the vibrational excitations, spanning over a range of $10^{-5}\,\mathrm{s}^{-1}$ - $10^{9}\,\mathrm{s}^{-1}$ in the example in Fig. 4.10.

4.4.1 Results for AF rates of states $\mathrm{X}^2\Sigma_g^+$, $\mathrm{A}^2\Pi_u$, and $\mathrm{C}^4\Sigma_u^+$

In the course of this thesis, AF rates for three electronic states of C_2^-, $\mathrm{X}^2\Sigma_g^+$, $\mathrm{A}^2\Pi_u$, and $\mathrm{C}^4\Sigma_u^+$, and a wide range of rotational excitations N were calculated. In the case of the two doublet states of the system, first approximations for k_f were already carried out in my Master's thesis [75]. However, here the attempt frequency k_a was set as the harmonic frequency of the electronic state at $N = 0$ and the potential modification for the more accurate identification of vibrational levels close to the maximum of the centrifugal barrier were not undertaken. Dissociation rates for the quartet state $\mathrm{C}^4\Sigma_u^+$ were not calculated before.

AF in the $\mathrm{X}^2\Sigma_g^+$ ground state

Fig. 4.11 shows an overview for the levels in the $\mathrm{X}^2\Sigma_g^+$ state able to undergo AF. In sub-figure (a), the region in which such vibrational levels exist is marked by the two blue lines, representing the ZPE and the maximum of the centrifugal barrier $E_{\mathrm{cb,max}}$ of the potential, plotted versus N. Here, the ZPE is defined as the energy of the energetically lowest-lying level ($v = 0$) for the rotating potential $V_N(R)$ (see Eq. (4.6)). The lower y-axis limit in Fig. 4.11 is chosen as the dissociation limit $D_0 = 8.41\,\mathrm{eV}$ of the system. Above a rotational excitation of $N = 248$, the potential does not support vibrational excitations anymore. This can also be observed in sub-figure (b), where the number of vibrational levels v_{max} is plotted versus N. With increasing rotational excitation, the potential becomes more shallow resulting in a lower number of levels. Two additional grey lines in Fig. 4.11(a), one solid and one

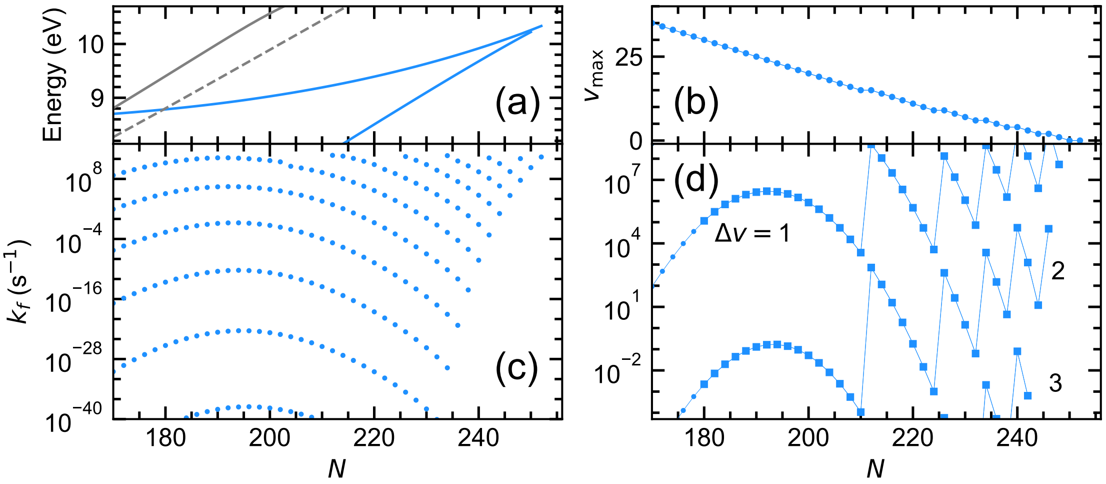

Figure 4.11: Auto-fragmentation of levels in the $X^2\Sigma_g^+$ state. (a) Maximum energy of the centrifugal barrier $E_{\text{bc,max}}$ and ZPE of the $X^2\Sigma_g^+$ state are represented by the upper and lower blue line, respectively, for different N. The solid/dashed grey lines mark the ZPE of the $X^1\Sigma_g^+/A^3\Pi_u$ state of the neutral dimer. (b) Highest vibrational excitation $v_{\max}$ for a given N. (c) Dissociation rate k_f plotted versus the rotational excitation. (d) Zoom into sub-figure (c), lines connect vibrational levels v with the same $\Delta v = v_{\max} - v$ for the range $\Delta v = 1, 2, 3$. Rates drawn in small circles/large squares lie above/below the ZPE of the lowest-lying neutral state with the same N.

dashed, present the ZPE of the neutral ground $X^1\Sigma_g^+$ and first excited $A^3\Pi_u$ state, respectively. As was already visible in Fig. 4.4, these two states have also rearranged their energetic order at these high rotational excitations. Anionic levels lying above those lines are able to undergo auto-detachment. This process will be discussed in more detail in Sec. 4.5.2. For vibrational levels lying in the region enclosed by the two blue lines in sub-fig. (a), dissociation rates were calculated according to the procedure described in the beginning of this Sec. 4.4. The resulting k_f are plotted in sub-figure 4.11(c). The rates span over ~ 70 orders of magnitude, only ~ 50 are shown in the figure to provide a clearer overview. Due to nuclear symmetry restrictions, only even N dissociation rates are plotted. Fig. 4.11(d) shows a zoom into a smaller range of k_f. Here, rates which correspond to vibrational levels v with the same $\Delta v = v_{\max} - v$ are connected with a line. Three sets of Δv with values $1, 2, 3$ are visible in the plot. Notably, levels within the same set have similar dissociation rates (within a few orders of magnitude). This can be intuitively understood when considering that the value of Δv is an indicator for a level's placement with respect to the maximum of the centrifugal barrier. The larger Δv, the deeper the vibration's

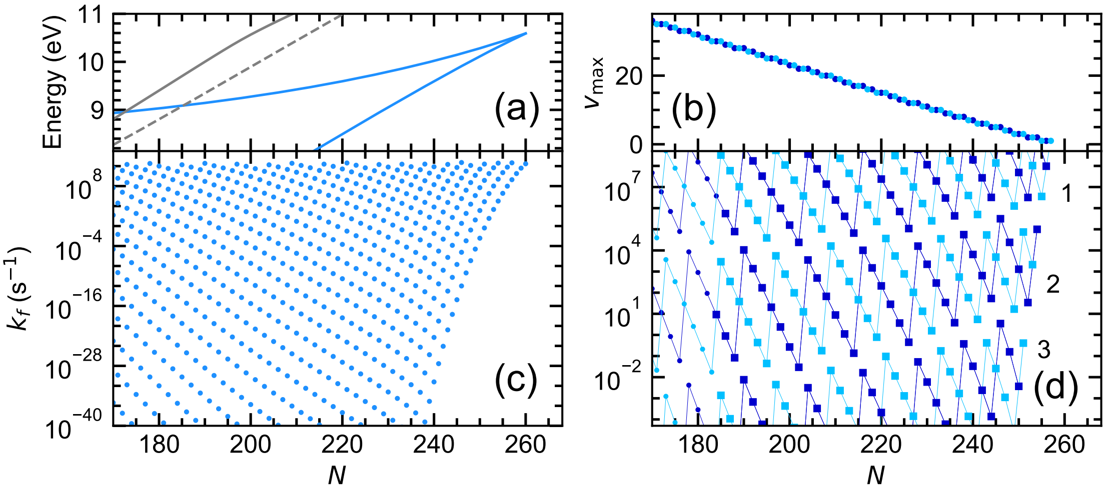

Figure 4.12: Auto-fragmentation of levels in the $A^2\Pi_u$ state. (a) Maximum energy of the centrifugal barrier $E_{\mathrm{bc,max}}$ and ZPE of the $A^2\Pi_u$ state are represented by the upper and lower blue line, respectively, for different N. The solid/dashed grey lines mark the ZPE of the $X^1\Sigma_g^+/A^3\Pi_u$ state of the neutral dimer. (b) Highest vibrational excitation v_{max} in the potential. Values belonging to even/odd rotational excitation are plotted in dark/light blue, respectively. (c) Dissociation rate k_f plotted versus the rotational excitation. (d) Zoom into sub-figure (c), lines connect vibrational levels v with the same $\Delta v = v_{\mathrm{max}} - v$ for the range $\Delta v = 1, 2, 3$. Rates drawn in small circles/large squares lie above/below the ZPE of the lowest-lying neutral state with the same N. Values belonging to even/odd rotational excitation are plotted in dark/light blue, respectively.

position inside the potential and the longer the respective barrier depth to tunnel through. The dissociating levels plotted in Fig. 4.11(d) are furthermore split into two classes indicated by the two different markers. Levels, which lie below the ZPE energy of the two neutral curves at the same rotational excitation (grey lines in subfig. (a)) are plotted in smaller circles. For these levels, the competing AD channel is available. In contrast, levels which are stable with respect to this channel are plotted in large squares.

AF in the first excited $A^2\Pi_u$ state

Analogous to Fig. 4.11, Fig. 4.12 shows an overview of levels in the first excited $A^2\Pi_u$ state of C_2^- with the ability to undergo AF. In sub-fig. (a), the blue lines, corresponding to the ZPE and $E_{\mathrm{bc,max}}$, again mark the region were dissociating vibrational levels exist. The solid/dashed grey line marks the ZPE of the $X^1\Sigma_g^+/A^3\Pi_u$ state of the neutral dimer. Fig. 4.12(b) shows the number of vibrational levels in the potential versus N. The maximum rotational excitation which still supports vibrations is $N = 260$ for this electronic state. It is important to note, that in contrast to the $X^2\Sigma_g^+$ state (see Fig. 4.11), both even and odd values of N are possible here. In sub-fig. (b) and (d), the two cases of even and odd rotational excitations are distinguished by dark and light blue, respectively. Fig. 4.12(c) shows an overview over the calculated dissociation rates, which spanned over more than 130 orders of magnitude. Again only ~ 50 orders of magnitude are shown here. Compared to the anionic ground state (see Fig. 4.11(c)) the dissociation rate density for the $A^2\Pi_u$ state is much higher. This is due to both the availability of both even and odd rotational excitations in $A^2\Pi_u$ as well as the slightly shallower potential of the excited state (compare ω_e and $\omega_e x_e$ in Tab. 4.1), which results in a larger density of vibrational levels. Fig. 4.12(d) shows a zoom into a smaller region of dissociation rates. Just as in Fig. 4.11(d), the levels are again grouped by Δv. However, here an additional distinction according to even/odd N in dark/light blue is carried out. The same trend of similar k_f for levels with the same Δv as discussed for Fig. 4.11 is visible here. Again, the stable/metastable levels with respect to auto-detachment are plotted in large squares/small circles in the figure.

AF in the third excited $C^4\Sigma_u^+$ state

For dissociating levels in the third excited $C^4\Sigma_u^+$ state of C_2^- an overview is given in Fig. 4.13. In sub-fig. (a) the energetic region which hosts these relevant levels is again marked with two blue lines, representing the ZPE and $E_{\mathrm{bc,max}}$ for different rotational excitations of the potential. The dashed grey line represents the ZPE of the lowest-lying triple state of the neutral carbon dimer $A^3\Pi_u$ with the same rotational excitation N as the anionic system. The dotted grey line corresponds to the ZPE of this neutral state for rotational excitation $N_n = N - 4$. As discussed in detail in Sec. 4.5.3, only anionic levels which lie below this second (dotted) line have sufficiently long AD lifetimes to be relevant for the experimental data presented in Sec. 4.1. Fig. 4.13(b) shows the number of vibrational levels v_{max} supported by the potential for different N. Due to nuclear symmetry considerations, only odd rotational excitations are populated for this electronic state. Potentials with $N > 205$ no longer support vibrational levels. In sub-fig. (c) an overview of the calculated k_f is given. The rates span over almost 70 orders of magnitude, out of which ~ 50 orders are shown in the plot. A zoom into a smaller rate range is displayed in Fig. 4.13(d). Vibrational levels with the same $\Delta v = v_{\mathrm{max}} - v$ are connected with lines and display similar dissociation rates. In contrast to Figs. 4.11 and 4.12, where levels were considered stable against AD, if they lay above the ZPE of the neutral state with the same N, the distinction here is with respect to the dotted line in Fig. 4.13(a). Levels which can undergo AD with a change of

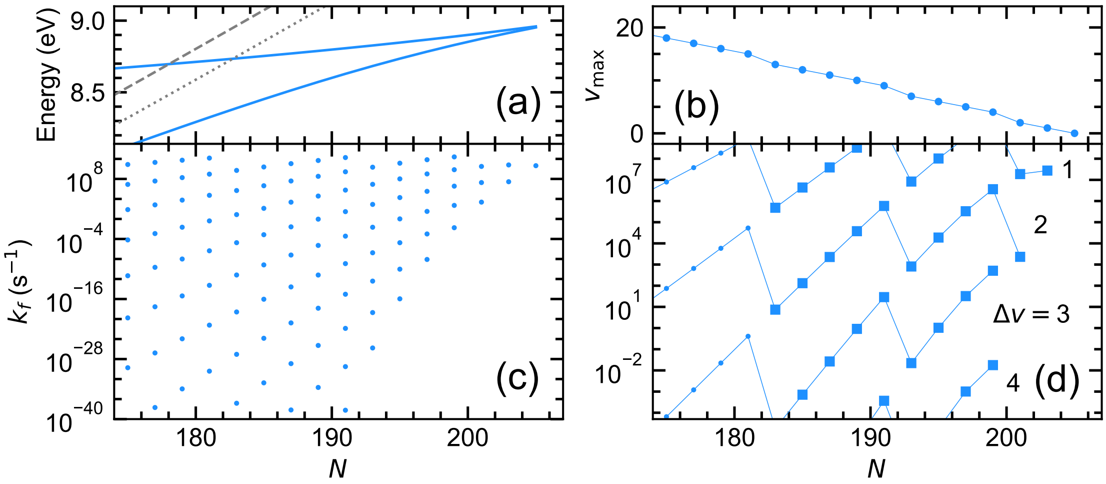

Figure 4.13: Auto-fragmentation of levels in the $C^4\Sigma_u^+$ state. (a) Maximum energy of the centrifugal barrier $E_{\mathrm{bc,max}}$ and ZPE of the $C^4\Sigma_u^+$ state are represented by the upper and lower blue line, respectively, for different N. The dashed grey line marks the ZPE of the neutral $A^3\Pi_u$ state at the same rotational excitation as the anionic state. The dotted grey line corresponds to the ZPE of the neutral $A^3\Pi_u$ for rotation $N_n = N - 4$. (b) Highest vibrational excitation v_{max} in the potential. (c) Dissociation rate k_f plotted versus the rotational excitation. (d) Zoom into sub-figure (c), a line is drawn through vibrational levels v with the same $\Delta v = v_{\mathrm{max}} - v$ for the range $\Delta v = 1, 2, 3, 4$. Rates drawn in small circles/large squares lie above/below the ZPE of the neutral $A^3\Pi_u$ state with rotational excitation $N_n = N - 4$.

rotational excitation of more then four ($\Delta N > 4$) are marked with larger squares while the rest are plotted in smaller circles.

Concluding remarks about AF in C_2^-

In this section, the dissociation rates of levels in three electronic states of C_2^-, $X^2\Sigma_g^+$, $A^2\Pi_u$, and $C^4\Sigma_u^+$, were calculated. In all cases, a large number of dissociating levels were found with the corresponding rates spanning over many orders of magnitude. Only a small fraction of levels were found to have AF rates, which are relevant for the experimental data discussed in Sec. 4.1 ($1 \lesssim k_f \lesssim 10^4$). Dissociating levels can be grouped together according to their relative vibrational excitation with respect to the number of vibrations in the potential Δv. The dissociation rates within these groups are similar and for $\Delta v = 1, 2, 3$ they lie roughly in the measurement window of the experiment used as a reference in this work ($0.8\,\mathrm{ms} \lesssim t \lesssim 800\,\mathrm{ms}$). Due to the bosonic nature of the ^{12}C atoms, only half of the rotational excitations in the Σ states are populated, which results in a lower number of dissociation rates for these states in comparison to the $\mathrm{A}^2\Pi_u$ state. Furthermore, the rotational excitation range for which dissociating levels with sufficient stability with respect to AD occur, differs between the states. While $N_{\min} \approx 180$ is similar for all states, the two doublet states support vibrational levels up to much higher rotational excitations ($N_{\max} = 248$ for $\mathrm{X}^2\Sigma_g^+$ and $N_{\max} = 260$ for $\mathrm{A}^2\Pi_u$) than the quartet state ($N_{\max} = 205$).

4.5 Auto-detachment rates

This section discusses the auto-detachment (AD) from different electronic states of C_2^-. This process is enabled by the non-adiabatic coupling of an initial anionic state to a final combined state which consists of a neutral state of the molecular system and the detached electron in the continuum. Here, the coupling mechanisms in question are the electronic-vibrational and electronic-rotational coupling. Both are mechanisms which are not considered in the Born-Oppenheimer approximation. The probability for an anion in initial state $|i\rangle$ to auto-detach into a final combined state $|f\rangle$ can be calculated using Fermi's golden rule [91]:

$$k_e = \frac{2\pi}{\hbar} \left| \langle f | \hat{\Lambda}_{fi} | i \rangle \right|^2 \rho(E_f). \tag{4.30}$$

Here, $\hat{\Lambda}_{fi}$ describes the coupling between the initial and final state and $\rho(E_f)$ the density of final states after electron ejection. The combined state $|f\rangle$ describes both the final state of the neutral dimer Γ as well as the electron in the continuum with symmetry γ and angular momentum l

$$|f\rangle \equiv |\Gamma\gamma l\rangle \,. \tag{4.31}$$

Here, it is important to note that the dependence of the coupling operator $\hat{\Lambda}_{fi} \equiv \hat{\Lambda}_{(\Gamma\gamma l)i}$ on the final state of the electron also includes the kinetic energy of this particle. Therefore, $\Lambda_{(\Gamma\gamma l)i}(R)$ varies with the energy of the ejected electron, e.g., shown in Fig. 7 of [91].

The rest of this section focuses on different auto-detachment mechanisms available in the anionic carbon dimer. First, an overview of previous AD studies of the carbon dimer, mainly concentrating on the second excited $\mathrm{B}^2\Sigma_u^+$ state, is given in Sec. 4.5.1. These works were not able to explain the millisecond AD signal observed at multiple ion storage facilities (see Fig. 4.1 and discussion in text). Afterwards, theoretical calculations carried out by Dr. Roman Čurík, Heyrovský Institute of Physical Chemistry, Prague, are presented. These investigate two different AD processes. Both focus on strongly non-adiabatic coupling mechanisms, which considerably decreases their corresponding detachment rates with respect to the previous studies discussed in Sec. 4.5.1. One is the coupling of high-lying vibrations in $X^2\Sigma_g^+$ to low vibrational excitations in the two lowest neutral states $X^1\Sigma_g^+$ and $A^3\Pi_u$, discussed in Sec. 4.5.2. The other process involves the AD of highly rotationally excited levels in the $C^4\Sigma_u^+$ quartet state detaching into the $A^3\Pi_u$ neutral state. Remarkably, for high enough values of N, the ejected electron carries away multiple quanta of rotational momentum, which strongly suppresses the corresponding auto-detachment rate. This process of rotationally-assisted AD is discussed in Sec. 4.5.3.

4.5.1 Previous studies on the auto-detachment of C_2^-

A detailed experimental study has been carried out by Hefter et al. [13] to investigate AD from the second excited electronic state of C_2^-. To this end, the authors employed absorption spectroscopy. The dimers were excited from the electronic ground state to the second excited $B^2\Sigma_u^+$ state. Here, vibrational levels with $v > 4$ lie above the zero-point energy (ZPE) of the ground state of the neutral dimer $X^1\Sigma_g^+$, into which detachment is possible. Additionally, starting at $v = 6$ in $B^2\Sigma_u^+$, the first excited state of the neutral dimer $A^3\Pi_u$ becomes energetically available for AD. By measuring the resonance width of the photo-absorption process, Hefter et al. were able to estimate the lifetimes of resonant vibrational levels up to $v = 10$. The measured rates vary over multiple orders of magnitude for the six considered vibrational excitations. The study also included different rotational excitations in the system. Here, a rotational dependence of the AD rates could be observed with a rise proportional to $N(N + 1)$.

For $v = 5$, Hefter et al. could only give an upper limit of $1\times10^7\,\mathrm{s}^{-1}$ [13]. However, later studies performed by Jones et al. [70] could further restrict this value by giving a lower limit of $1\times10^6\,\mathrm{s}^{-1}$. For vibrational levels $v > 5$, the AD rates are considerably higher starting at $3.8 \times 10^8\,\mathrm{s}^{-1}$ for $v = 6$ and going beyond $3 \times 10^{10}\,\mathrm{s}^{-1}$ for $v = 10$. The authors attribute this sharp rise to the opening of the AD channel into the neutral excited $A^3\Pi_u$ state of the dimer. However, a later experimental study by Ervin and Lineberger contested this assumption [83]. More recent calculations by Dr. Roman Čurík, Heyrovský Institute of Physical Chemistry, instead identified a peak in the non-adiabatic coupling function as the likely cause for the sharp rate rise at $v = 6$ [92, 90]. The overlap between this feature and the final wavefunction was found to strongly increase between the final vibrational levels $v = 0$ and $v = 1$, latter of which is only accessible for initial vibrational levels $v > 5$.

Hefter et al. also investigated AD lifetimes of high-lying vibrational levels ($v > 15$) of the first excited anionic state $A^2\Pi_u$. This proved experimentally more challenging than for the second excited $B^2\Sigma_u^+$ state. Due to the unfavourable Frank-Condon overlap between these high vibrational excitations and the vibronic ground state of the system, photo-excitation was not efficient for these transitions. However, auto-detaching vibrational levels in the two *ungerade* states $A^2\Pi_u$ and $B^2\Sigma_u^+$ lie in close energetic proximity. As a result, these levels can couple leading to small

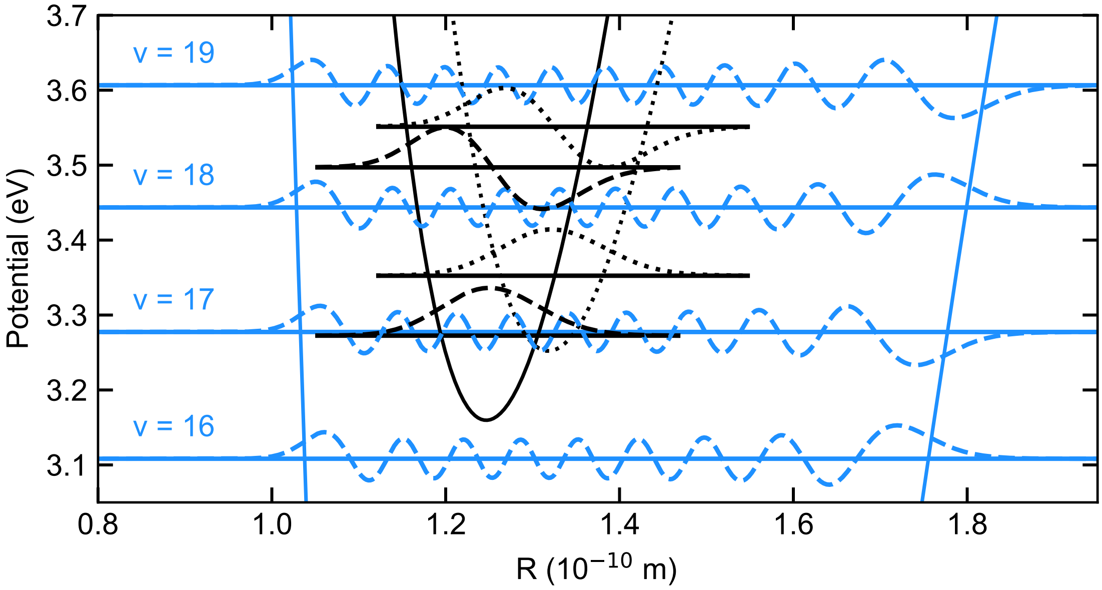

Figure 4.14: Zoom into the overlap region of the potential curves of the anionic $X^2\Sigma_g^+$ state, drawn in blue, and the neutral $X^1\Sigma_g^+$ and $A^3\Pi_u$ states drawn in solid and dotted black lines, respectively. Vibrations and the corresponding wavefunctions in this energy window are drawn for all three electronic states. For levels in the $X^2\Sigma_g^+$ state, the vibrational excitation are labelled.

perturbations in both states. Through this effect, Hefter et al. were able to observe AD resonances which displayed features of both Σ- and Π-state characteristics. From these they could extract an upper AD rate limit of $1 \times 10^8\,\mathrm{s}^{-1}$.

The authors in [13, 70] were not able to observe any AD rates in the range of milliseconds. Levels in the $B^2\Sigma_u^+$ state were found to detach with at least $1 \times 10^6\,\mathrm{s}^{-1}$ [70] and therefore too fast for the observed AD signal on millisecond timescales [16, 17, 19, 18]. In contrast, only an upper rate limit of $1 \times 10^8\,\mathrm{s}^{-1}$ could be established for high-lying levels in the $A^2\Pi_u$ state ($v \geq 16$). However, in the course of the radiative decay rate calculations in Sec. 4.3.2 it became apparent, that these high vibrations do not live sufficiently long to be the origin of a process with millisecond lifetimes. Therefore, both doublet excited states of C_2^-, $A^2\Pi_u$ and $B^2\Sigma_u^+$, can be ruled out as the source of the AD signal shown in Fig. 4.1.

4.5.2 Auto-detachment from high vibrations of the $X^2\Sigma_g^+$ state

One of the AD processes calculated by Dr. Roman Čurík, Heyrovský Institute of Physical Chemistry, focuses on highly-excited vibrational levels in the $X^2\Sigma_g^+$ ground

Table 4.8: Symmetries of the initial and final state of the dimer as well as the ejected electron for levels in $X^2\Sigma_g^+$ undergoing AD.

Anionic state	Neutral state	Ejected electron	Lowest partial wave
$^2\Sigma_g^+$	$^1\Sigma_g^+$	$^2\Sigma_u^+$	p
	$^3\Pi_u$	$^2\Pi_g$	d

state of C_2^-. These can auto-detach by coupling to low-lying vibrations in the first two neutral states of the system. This type of strongly non-adiabatic coupling between vibrational and electronic excitations has been both experimental observed and theoretically described for other systems [91, 11, 93]. The *ab initio* curves ($N = 0$) for the anionic ground state and the lowest two neutral states of the system are shown in Fig. 4.14. The neutral curves are shifted up by 226 meV to match the measured electron affinity (EA) of Ervin and Lineberger [83] (see Tab. 4.2). This was necessary due to the dependency of the non-adiabatic coupling function on the energy of the ejected electron as mentioned in the beginning of this Sec. 4.5.2. *Ab initio* calculations only provide an accuracy of typically a few 100 meV for the EA, which is much larger than the uncertainty of the measured value. As visible in Fig. 4.14, vibrational levels $v \geq 17$ in $X^2\Sigma_g^+$ lie above the ZPE of the neutral ground state $X^1\Sigma_g^+$ and can therefore undergo AD. Furthermore, for levels $v > 17$ the first excited neutral state $A^3\Pi_u$ becomes available for auto-detachment. Tab. 4.8 lists the symmetries of the initial anionic state and the final state, consisting of the neutral dimer and the ejected electron as well as the lowest partial wave the electron can be detached in.

The AD rate calculations for high vibrations in the $X^2\Sigma_g^+$ state are described in [90] and will be summarized below. Dr. Roman Čurík followed the approach published in [91]. Here, the matrix element in Eq. (4.30) was calculated by integrating over the convolution of the final vibrational wavefunction $\psi_{\Gamma\gamma l}$, the derivative of the initial vibrational wavefunction $\frac{\partial}{\partial R}\psi_i$ and the non-adiabatic coupling function $\Lambda_{\Gamma\gamma l,i}(R)$ [91]

$$\langle\Gamma\gamma l|\,\hat{\Lambda}_{\Gamma\gamma l,i}\,|i\rangle = \frac{\hbar^2}{\mu}\int \psi^*_{\Gamma\gamma l}(R)\Lambda_{\Gamma\gamma l,i}(R)\frac{\partial}{\partial R}\psi_i(R)dR. \tag{4.32}$$

The coupling function can be computed in first order by using the initial and final electronic states $\Psi_{i,\Gamma\gamma l}$ [91]

$$\Lambda_{\Gamma\gamma l,i}(R) = \int \Psi^*_{\Gamma\gamma l}(\vec{r},R)\frac{\partial}{\partial R}\Psi_i(\vec{r},R)d\vec{r}, \tag{4.33}$$

where $\vec{r}$ represents all electronic coordinates. For the results presented here, Eq. (4.33) and the MRCI method of the MOLPRO package [80] with the aug-pVTZ basis set [81] were used to derive $\Lambda_{\Gamma\gamma l,i}(R)$ for different energies of the ejected

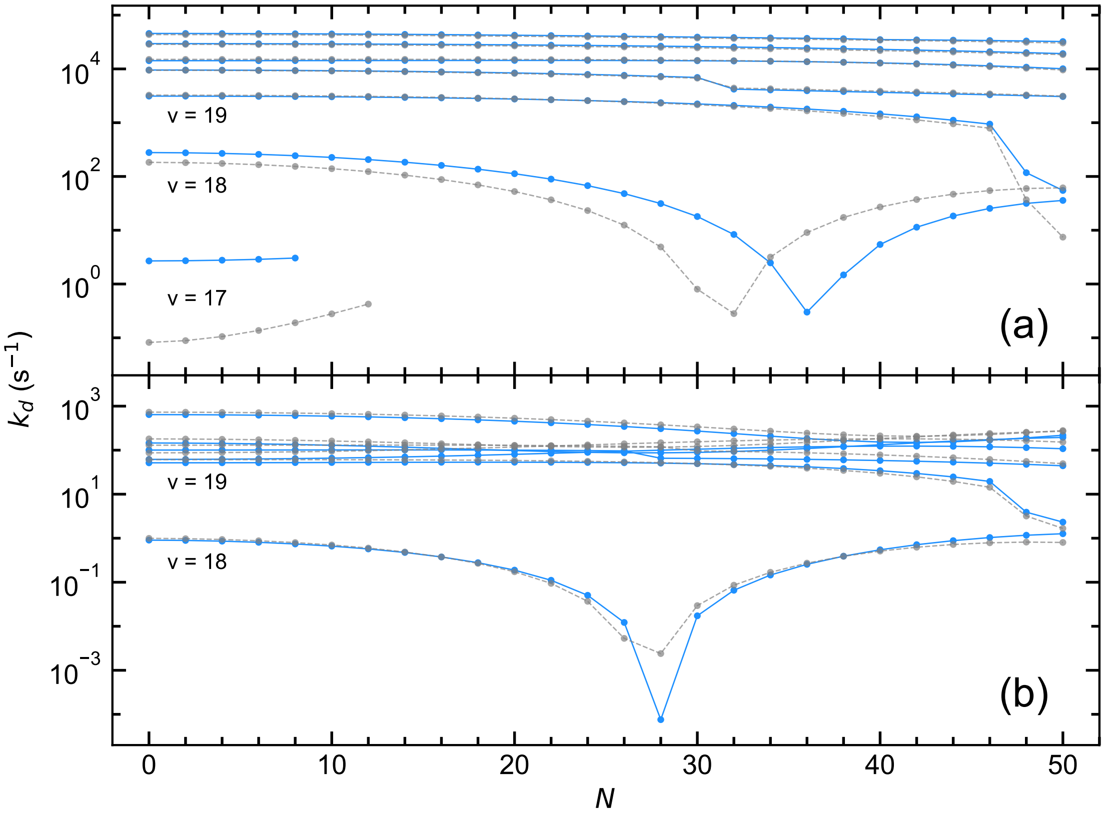

Figure 4.15: Auto-detachment rates k_d of high-lying vibrational levels in the $X^2\Sigma_g^+$ state. Levels with the same vibrational excitation are connected with a line. Vibrations $v = 17, 18, 19$ are labelled in the plot. Unlabelled lines correspond to the continuously increasing $19 < v < 24$ levels. (a) Total AD rates including both the decay to the neutral $X^1\Sigma_g^+$ ground, as well as the first excited $A^3\Pi_u$ state. Rates drawn in blue/grey were derived using the *ab initio*/spectroscopic neutral curves. (b) Partial AD rates only for the channel to the excited $A^3\Pi_u$ neutral state.

electron. For the representation of the electron in the continuum, the approach presented in [91] was employed. The auto-detachment rates were then derived according to Eq. (4.30).

Results of the AD rate calculations for vibrations $v = 17-23$ in the $X^2\Sigma_g^+$ anionic ground state are shown in Fig. 4.15 for rotational excitations $N \leq 50$. Due to the Pauli principle, only even rotational excitations are populated. The plot is split into two sub-figures. Panel (a) shows the total auto-detachment rates of the vibrational levels consisting both of the decay into the neutral $X^1\Sigma_g^+$ ground as well as the first excited $A^3\Pi_u$ state. The AD rates only into the $A^3\Pi_u$ state are displayed separately

Table 4.9: Auto-detachment of vibrational levels $v = 17 - 20$ in the anionic $X^2\Sigma_g^+$ state into the lowest two neutral states $X^1\Sigma_g^+$ and $A^3\Pi_u$. Rates are given for three rotational excitations $N = 0, 28, 50$ and two different sets of neutral potentials, one applying the spectroscopic values published in [83] and one using the results from the *ab initio* calculations presented in Sec. 4.2.2.

	Spectroscopic		***ab initio***	
Vibration	$X^1\Sigma_g^+$	$A^2\Pi_u$	$X^1\Sigma_g^+$	$A^2\Pi_u$
		N = 0		
17	8.20×10^{-2}	-	2.69	-
18	1.82×10^{2}	9.93×10^{-1}	2.77×10^{2}	9.05×10^{-1}
19	3.19×10^{3}	6.10×10^{1}	3.69×10^{3}	5.16×10^{1}
20	9.30×10^{3}	1.30×10^{2}	9.44×10^{3}	1.01×10^{2}
		N = 28		
18	4.88	2.40×10^{-3}	3.13×10^{1}	7.57×10^{-5}
19	2.25×10^{3}	5.20×10^{1}	2.31×10^{3}	5.08×10^{1}
20	7.00×10^{3}	1.19×10^{2}	7.20×10^{3}	6.55×10^{1}
		N = 50		
18	6.06×10^{1}	8.02×10^{-1}	3.46×10^{1}	1.27
19	5.76	1.67	5.26×10^{1}	2.32
20	3.07×10^{3}	4.93×10^{1}	3.02×10^{3}	4.42×10^{1}

in panel (b). These were found to always lie at least one order of magnitude below the corresponding AD rates into the $X^1\Sigma_g^+$ state. This is also visible in Tab. 4.9, where a selection of rates are listed.

In order to estimate the sensitivity of the calculations on the shape of the electronic curves, AD rates k_d were derived for two different sets of potentials. For one, the *ab initio* results (see Sec. 4.2.2) were used to calculate the neutral potentials. For the other, the neutral curves were estimated using a Morse potential and the values given by Ervin and Lineberger [83]. In both cases, the EA was fixed to the experimental value given in [83]. Additionally, the *ab initio* potential of the $X^2\Sigma_g^+$ anionic ground state was employed in both cases. This decision was made, because of the high vibrational excitations $v \geq 17$ considered in the anionic state. Spectroscopic values describe electronic potentials well around the equilibrium distance, where the low vibrations are situated. These are of relevance for the final neutral states in the process discussed here (see Fig. 4.14). Therefore, it is feasible to describe the neutral potential using the spectroscopic data. However, for the high vibrations in the anionic ground state considered here, the *ab initio* results provide a more precise description of the potential.

The calculated rates for the two different sets of potentials are shown for the *ab initio*/spectroscopic neutral curves in blue/grey in Fig. 4.15. Furthermore, a selection of both is given in Tab. 4.9. Some of the rates lie in the millisecond range and could therefore potentially cause the measured AD signal. Hence, high-lying vibrations of the $X^2\Sigma_g^+$ will be considered in the following Sec. 4.6, where a decay model is used to compare the measured signal to the theoretical calculations. For levels $v \geq 20$, the agreement between the rates derived using the different neutral potentials is very good. For the lowest three vibrations, significant relative differences are visible if $k_d \lesssim 5 \times 10^2\,\mathrm{s}^{-1}$. Here, the rate is very sensitive to the small differences between the two sets of neutral potentials. However, both sets of k_d cover the same rate region spanning over more than five orders of magnitude. Therefore, a decay model considering the convolutions of each set, as discussed in detail in Sec. 4.6, is not expected to produce vastly different results.

4.5.3 Rotationally assisted auto-detachment from the $\mathbf{C^4\Sigma_u^+}$ state

This sub-section focuses on the auto-detachment of levels in the anionic quartet state $C^4\Sigma_u^+$. Due to the spin of this state, $S = 3/2$, detachment is only possible into neutral states with $S = 1$ or 2 (since the spin of the ejected electron is 1/2). Therefore, out of the two neutral states in the carbon dimer considered in this work so far, $X^1\Sigma_g^+$ and $A^3\Pi_u$, only latter can serve as a final state for AD here. The neutral dimer furthermore has an additional excited bound state, $B^3\Sigma_g^-$, which also has the required spin of 1 [67]. This state is known from previous studies to lie almost 2 eV above the first excited $A^3\Pi_u$ triplet state [67]. Consequentially, it is positioned energetically above the ZPE of the lowest-lying quartet state of C_2^- (see Tabs. 4.1 and 4.2). Furthermore, based on the spectroscopic parameters given in [67], the potential of this neutral state $B^3\Sigma_g^-$ does not intersect with that of the anionic $C^4\Sigma_u^+$ curve at any internuclear distance R. This was also confirmed by *ab initio* calculations carried out by Ass. Prof. Dr. Milan Ončák, Innsbruck University [94]. He additionally found that the two excited neutral bound states, $A^3\Pi_u$ and $B^3\Sigma_g^-$, only intersect with each other at $R \sim 2\,\text{Å}$. From the excitation energy and the shape of the $B^3\Sigma_g^-$ neutral state, its significance for the AD of levels in $C^4\Sigma_u^+$ can be estimated. In the rotational excitation range considered here, this state will not energetically rearrange with either the anionic $C^4\Sigma_u^+$ nor the neutral $A^3\Pi_u$ state. The rearrangement with the latter (neutral) state is not observable due to the large internuclear distance of the intersection point at $R \sim 2\,\text{Å}$ (compare to the intersections investigated in Fig. 4.4). As a result, the rotational excitation required for re-arrangment lies above the N-region relevant here. Therefore, any levels in the anionic quartet state for which the AD channel into $B^3\Sigma_g^-$ is available can also decay into energetically lower-lying levels in the $A^3\Pi_u$ state. It can therefore be expected, that the resulting decay rate will always be predominantly given by the detachment into the $A^3\Pi_u$ state. Therefore, AD into the second excited neutral state will be neglected here.

For AD into the first excited neutral state $A^3\Pi_u$ the symmetries of the involved neutral ($^3\Pi_u$) and anionic ($^4\Sigma_u$) states result in the detaching electron's ejection in a Π_g wave. This corresponds to an angular momentum of the electron of predominantly $l = 2$. For a given anionic rotation N and angular momentum of the ejected electron l, the neutral dimer can have a rotational excitation N_n in the range of

$$N - l \leq N_n \leq N + l. \tag{4.34}$$

This restriction is given by angular momentum conservation (see the 3j-Wigner symbol in Eq. (3) of [95]). For $l = 2$, this results in a maximum change of rotational excitation $\Delta N_{\max} = N - N_n = 2$.

For moderate rotational excitation of the system ($N < 155$), the anionic $C^4\Sigma_u^+$ state lies energetically above the neutral $A^3\Pi_u$ state (see Fig. 4.3). At these N, the anionic curve has resonant character and all levels can detach by ejecting an electron with angular momentum $l = 2$. The corresponding rates are on atomic timescales. This has already been reported in the works of Halmová et al. [78, 79]. Calculations by Dr. Roman Čurík, Heyrovský Institute of Physical Chemistry, put the corresponding lifetimes for this resonant AD process at femto- to picoseconds [95]. For the calculations the modified quartet curve described in Sec. 4.2 was employed. It combines the *ab initio* (MOLPRO) results obtained by Ass. Prof. Dr. Milan Ončák, Innsbruck University, with the R-matrix calculations published by Halmová [79]. For the neutral $A^3\Pi_u$ state, the employed *ab initio* potential was energetically shifted by 226 meV to match the measured EA of Ervin and Lineberger [83]. The calculations show that levels, which can decay by ejecting an electron with $l = 2$ do not live sufficiently long to contribute to either of the measured signals.

At high rotational excitation ($N \gtrsim 155$), the potential landscape differs strongly from that corresponding to the low to moderate N range (see Fig. 4.4). This significantly influences the AD rates for levels in the $C^4\Sigma_u^+$ state. A similar rotational effect on the auto-detachment rates has already been observed for different isotopologues of the anionic hydrogen dimer [96, 97]. Here, the rotational excitation modifies the neutral and anionic potentials such that the amplitudes of the vibrational wavefunctions decrease in the AD region. This is the internuclear distance range, in which the neutral and anionic wavefunctions overlap. For the systems studied previously (H_2^-, D_2^- and HD^-) this potential modification resulted in an AD rate decrease by roughly four orders of magnitude for rotational excitations $N \approx 20 - 40$ in comparison to the rotationless case [96, 97].

The rotational effect on the AD of the $C^4\Sigma_u^+$ in C_2^- differs from the previous study in two ways. First, the system is much heavier than the heaviest hydrogen dimer isotopologue studied before (D_2^-). Consequentially, the rotational excitations

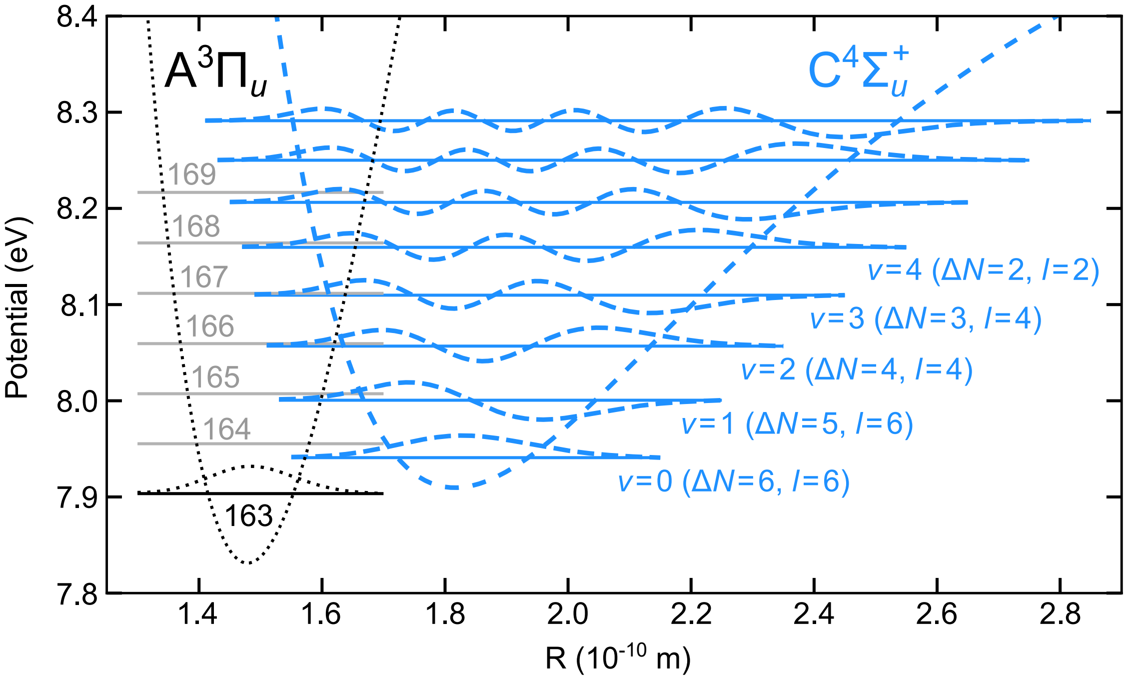

Figure 4.16: Auto-detachment of levels in the anionic $C^4\Sigma_u^+$ state, drawn in blue, for $N = 169$. Excitation energies and vibrational wavefunctions are indicated in the figure. The potential of the $A^3\Pi_u$ neutral state with rotational excitation $N_n = 163$ is plotted in a dotted black line. The ZPE and the corresponding vibrational wavefunction are also drawn in black. Grey horizontal lines indicate the ZPE energy of this neutral state for higher N_n up to $N_n = N = 169$. Low-lying levels of the anionic curve are labelled according to their vibrational excitation, the required change in rotational excitation to undergo AD, ΔN, as well as the minimum angular momentum l the electron can be ejected in.

required to see significant changes of the potentials are higher for the carbon dimer. This is caused by the dependence of the centrifugal energy on the inverse of the reduced mass (see Eq. (4.6)). Second, and more importantly, the modification of the anionic quartet $C^4\Sigma_u^+$ potential and the neutral $A^3\Pi_u$ potential leads to the energetic rearrangement of the two curves for $N \gtrsim 155$ (see Sec. 4.2.3). At these rotations (N) vibrational levels exist, which lie not only below the ZPE of the neutral $A^3\Pi_u$ state with the same rotation ($N_n = N$) but also below the ZPE corresponding to the neutral potential for rotational excitation $N_n = N - 2$. This sort of rearrangement was not observed in the hydrogen systems, where the anionic potential lies energetically above the neutral curve for all N.

The energetic rearrangement at high N for the quartet state of C_2^- results in anionic levels in $C^4\Sigma_u^+$, which can no longer decay by ejecting an electron with $l = 2$

due to their position below the ZPE of the neutral curve for $N_n = N - 2$. However, the detachment into neutral levels with lower rotation excitation $N_n < N - 2$ is still energetically available. This is exemplarily shown in Fig. 4.16 for the lowest vibrations in the $\mathrm{C}^4\Sigma_u^+$ state at $N = 169$. Here, the ZPE of the $\mathrm{A}^3\Pi_u$ state is indicated for different rotational excitations. Multiple anionic levels, drawn in blue, lie below the ZPE corresponding to $N_n = N - 2 = 167$. These levels can only undergo AD when allowing the simultaneous reduction of the rotational excitation of the system by up to six quanta (for $v = 0$) for the example displayed in the figure. These additional rotational quanta have to be carried away by the ejected electron in order to preserve angular momentum conservation. As discussed above, the ejected electron for the AD process from a ${}^4\Sigma_u^+$ to a ${}^3\Pi_u$ state has a Π_g character. Therefore, the angular momentum of the electron has to be even and at least 2 ($l = 2m$ with $m = 1, 2, 3, ...$). Using Eq. (4.34), the minimal values of l for an AD process which requires a change of rotation ΔN can be calculated. For the exemplary case of $N = 169$, these are given in Fig. 4.16 for the lowest five vibrations.

This AD channel, which is only possible if the electron carries away additional quanta of rotational excitation, has not been theoretically described or experimentally assigned to any system before. The scientists involved in the project presented in this Chap. 4 propose the name "rotationally assisted auto-detachment" for this process. The theoretical description was derived and the AD rate calculations were carried out by Dr. Roman Čurík, Heyrovský Institute of Physical Chemistry. The theoretical description necessary to calculate the rates for rotationally assisted AD presents an extension of the works by Čížek et al. [96, 97, 98]. These focus mainly on a non-local resonance model, which can be used to describe the detachment of low-energy electrons. The extension for the process of relevance here is the incorporation of the rotational degrees of freedom into the model [98]. This allows for the calculation of rates for AD including a change in rotational excitation. The theoretical derivation is described in detail in [95] and will not be repeated here. The results of the rate calculations are summarized below.

AD rates k_d for rotationally highly-excited levels in the $\mathrm{C}^4\Sigma_u^+$ state of C_2^- are drawn versus N in Fig. 4.17. Panel (a) shows an overview of the a range of rotational and vibrational excitations for the unshifted quartet potential (see Fig. 4.3). The AD rates span over many orders of magnitude, even within the same rotational excitation. The rates can be grouped into sets which have similar values on a logarithmic scale. Between these sets, there are a multiple orders of magnitude gaps without any rates. A closer inspection of the calculation results reveals, that all levels corresponding to a rate-set share the same minimum angular momentum l the electron can be ejected in. The different sets in Fig. 4.17(a) are labelled according to this minimum l. The strong AD rate suppression for increasing l of the ejected electron has two reasons. The first is given by the overlap of the initial (anionic) and final (neutral) vibrational wavefunctions. As the required ΔN increases, this value decreases as the wavefunction amplitudes decrease in the overlap region (see

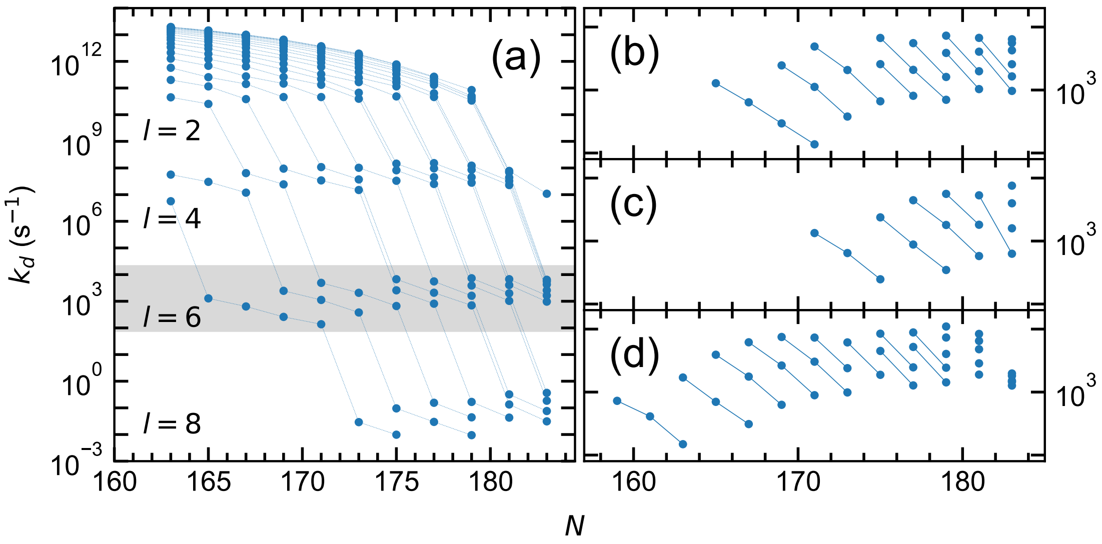

Figure 4.17: Auto-detachment rates k_d for levels in the $C^4\Sigma_u^+$ state of C_2^-. (a) Overview of AD rates for different angular momenta of the ejected electron l using the unshifted anionic potential. Rates corresponding to the same vibrational excitation are connected with a thin line. The region corresponding to the AD rates dominated by the ejection of an electron with $l = 6$ is shaded in grey. Panels (b) - (d) show a zoom into this region ($l = 6$) for the unshifted, upwards shifted and downwards shifted anionic potential, respectively. Here, rates corresponding to the same vibration up to $v_{\max} = 9, 4, 10$ are connected with lines, respectively.

for example Fig. 4.16). The same effect is also responsible for the AD rate decrease in rotationally excited hydrogen dimer isotopologues [96, 97]. The second reason is the rate at which electrons with higher angular momentum l can be ejected. This is given by the partial width Γ_l, which decreases by multiple orders of magnitude between $\Gamma_{l'}$ and $\Gamma_{l'+2}$ (see Supplement Material of [95]). As a result, the AD rate is always dominated by the decay channel corresponding to the smallest possible value of l.

AD rates corresponding to the ejection of an electron with $l < 6$ ($\Delta N \leq 4$) are too large to contribute to the measured signal ($0.8\,\mathrm{ms} \leq t \leq 800\,\mathrm{ms}$). On the other hand, levels which decay with $l = 8$ have very small AD rates in the order of $\sim 10^{-2}\,\mathrm{s}^{-1}$. As a result, these levels predominantly decay through one of the other channels (AF or radiative relaxation). Especially those, which lie above the dissociation threshold typically display large AF rates, due to their energetic position close to the maximum of the centrifugal barrier. Levels, which predominantly decay by ejecting an electron with $l = 6$ have AD rates which are similar to the main decay component

Table 4.10: AD rates for levels in the $C^4\Sigma_u^+$ state decaying with $l = 6$ calculated for the three anionic quartet potentials.

Unshifted			**Shift up**			**Shift down**		
N	v	k_d	N	v	k_d	N	v	k_d
165	0	1.28×10^3	171	0	1.34×10^3	159	0	7.26×10^2
167	0	6.38×10^2	173	0	6.45×10^2	161	0	4.11×10^2
169	0	2.59×10^2	175	0	2.47×10^2	163	0	1.49×10^2
169	1	2.46×10^3	175	1	2.38×10^3	163	1	1.70×10^3
171	0	1.37×10^3	177	1	8.81×10^2	165	1	7.00×10^2
171	1	1.12×10^3	177	2	4.45×10^3	165	2	3.92×10^3
171	2	4.90×10^3	179	1	3.47×10^2	167	1	3.10×10^2
173	1	3.79×10^2	179	2	1.81×10^3	167	2	1.76×10^3
173	2	2.08×10^3	179	3	5.32×10^3	167	3	6.17×10^3
175	2	6.63×10^2	181	2	5.78×10^2	169	2	6.28×10^2
175	3	2.58×10^3	181	3	1.82×10^3	169	3	2.64×10^3
175	4	6.71×10^3	181	4	5.32×10^3	169	4	7.50×10^3
177	3	8.10×10^2	183	4	6.29×10^2	171	3	8.92×10^2
177	4	2.09×10^3	183	5	1.59×10^3	171	4	3.04×10^3
177	5	5.55×10^3	183	6	3.98×10^3	171	5	7.34×10^3
179	4	7.00×10^2	183	7	7.57×10^3	173	4	9.87×10^2
179	5	1.61×10^3				173	5	2.40×10^3
179	6	3.88×10^3				173	6	6.15×10^3
179	7	7.30×10^3				175	6	1.88×10^3
181	6	1.03×10^3				175	7	4.50×10^3
181	7	1.99×10^3				175	8	8.46×10^3
181	8	4.06×10^3				177	7	1.28×10^3
181	9	6.73×10^3				177	8	2.47×10^3
183	8	9.68×10^2				177	9	5.21×10^3
183	9	1.65×10^3				177	10	8.85×10^3
183	10	2.57×10^3				179	9	1.43×10^3
183	11	4.27×10^3				179	10	2.44×10^3
183	12	5.60×10^3				179	11	4.03×10^3
183	13	3.40×10^3				179	12	7.35×10^3
						179	13	1.10×10^4
						181	12	1.90×10^3
						181	13	2.86×10^3
						181	14	4.79×10^3
						181	15	6.49×10^3
						181	16	8.39×10^3
						183	17	1.46×10^3
						183	18	1.82×10^3
						183	19	1.97×10^3
						183	20	1.27×10^3
						183	21	1.51×10^3

($k_\mathrm{ex} \sim 300\,\mathrm{s}^{-1}$) measured at multiple ion storage facilities (see Fig. 4.1). They can be found in the rotational excitation range $163 \leq N \leq 183$ for the unshifted quartet potential. Here, the lower limit is given by the minimal rotation required for the anionic curve to rearrange with the neutral potential corresponding to $N_n < N - 4$. For $N > 183$, the energetic rearrangement between the anionic and neutral curves is so strong, that AD is only possible with $\Delta N > 6$ for all levels in the potential. The decay region corresponding to the $l = 6$ rate-set is grey-shaded in Fig. 4.17(a).

Levels which auto-detach with $l = 6$ present a potential origin for the measured signal. Therefore, the uncertainty of the AD rate calculations of these levels was estimated. It was found, that the rates strongly depend on the energetic position of the anionic $\mathrm{C}^4\Sigma_u^+$ curve with respect to the neutral $\mathrm{A}^3\Pi_u$ curve. Therefore, the AD rate calculations were carried out three times. Once for the unshifted anionic potential using the curve given by the combination of the *ab initio* (MOLPRO) calculations and the R-matrix results from [79] (see Sec. 4.2.2). These results are shown in panels (a) and (b) of Fig. 4.17, where latter presents a zoom into the region of k_d for $l = 6$. The *ab initio* part of the anionic curve was then once shifted up and once down by 170 meV. This is a typical value for the uncertainty of the underlying *ab initio* (MOLPRO) calculations. The potential was then again constructed using the shifted *ab initio* (MOLPRO) data and the R-matrix results from [79] (see Fig. 4.3). The resulting rates for levels which decay with $l = 6$ are shown in panels (c) and (d) of Fig. 4.17, respectively. They are also listed together with the rates for the unshifted potential in Tab. 4.10. The energetic shift up/down of the *ab initio* part of anionic potential causes the decrease/increase of the N range which hosts vibrations that decay with $l = 6$. The larger/smaller energetic separation of the anionic and neutral states require larger/smaller rotational excitation in order to reach a situation were levels are stable against AD for $\Delta N \leq 4$. Additionally, the k_d range for levels decaying with $l = 6$ slightly decreases/increases for the upwards/downwards shifted potential. However, the three sets of k_d rates (for the unshifted, upwards and downwards shifted potential) have the same overall features. All display the distinctive separation of AD rates according to their lowest l value observable in Fig. 4.17(a). Furthermore, these subsets for a specific value of l lie in the same rate range for all three anionic potential scenarios.

4.6 Comparing the measurement to a decay model

The total decay of a single state j can be described through the sum of rates for the different decay channels. In the system discussed here, these are A_j, $k_{f,j}$, and $k_{d,j}$ for electronic transitions, AF and AD, respectively. The overall decay of this state is then given by the rate k'_j with

$$k'_j = A_j + k_{f,j} + k_{d,j}. \tag{4.35}$$

The contribution of level j to one of the auto-decay signals s_x^j, with $x = \{f, d\}$, measured on the detector in the experiment can be calculated with

$$s_x^j(t) = \epsilon_{\mathrm{det}}\, N_0\, P_j(t)\, k_{x,j}\, e^{-k'_j t}. \tag{4.36}$$

Here, N_0 gives the initial number of ions, $\sim 4 \times 10^7$ for the measurement at hand, and $P_j(t)$ is the probability for an ion to be in state j at storage time t. The detection efficiency ϵ_{det} is given by Eq. (4.3). The overall decay signal for channel x on the detector is then given by the sum over all levels contributing to this decay channel,

$$s_x(t) = \epsilon_{\mathrm{det}}\, N_0 \sum_j P_j(t)\, k_{x,j}\, e^{-k'_j t}. \tag{4.37}$$

The overall number of ions in j contributing to the signal, S_x^j, in a storage time window $t_1 \leq t \leq t_2$ can be calculated by integrating Eq. (4.36). It is approximately given by

$$S_x^j = \int_{t_1}^{t_2} s_x^j(t)\, dt \approx \int_{t_1}^{\infty} s_x^j(t)\, dt \approx N_j^0\, Y_{x,j}. \tag{4.38}$$

The factor $Y_{x,j}$ describes the yield of state j to the signal s_x,

$$Y_{x,j} = e^{-t_1 k'_j}\, \frac{k_{x,j}}{k'_j}. \tag{4.39}$$

The exponential factor in Eq. (4.39) accounts for the probability of the ions to decay on the way to the storage ring, with $t_1 = 0.8\,\mathrm{ms}$ here (see Fig. 4.2). Two assumptions are made in Eq. (4.38). First: t_2 is sufficiently large such that the ions have decayed after this time with a high probability ($k'_j \gg t_2^{-1}$). In this case, the upper bound of the integral can be approximated with $t_2 \approx \infty$. For the measurement discussed here, the upper storage time limit is given by $t_2 = 800\,\mathrm{ms}$ (see Fig. 4.2). The applicability of this assumption will be discussed in Sec. 4.6.1. Second: The number of ions decaying from state j into either of the auto-decay channels is roughly given by the initial population of this state N_j^0. Hence, repopulation through radiative de-excitation from higher-lying levels is negligible. This will be discussed in more detail in Sec. 4.6.2.

The rest of this section is structured as follows. First, the yields for levels originating from the different electronic states for either of the two destructive decay channels, AF and AD, are presented in Sec. 4.6.1. Afterwards, the evolution of the internal population of the ions is discussed in Sec. 4.6.2. Here, also two initial populations and the possibility of repopulation through radiative decay from higher-lying levels are considered. The resulting decay model is compared to the measurements in Sec. 4.6.3.

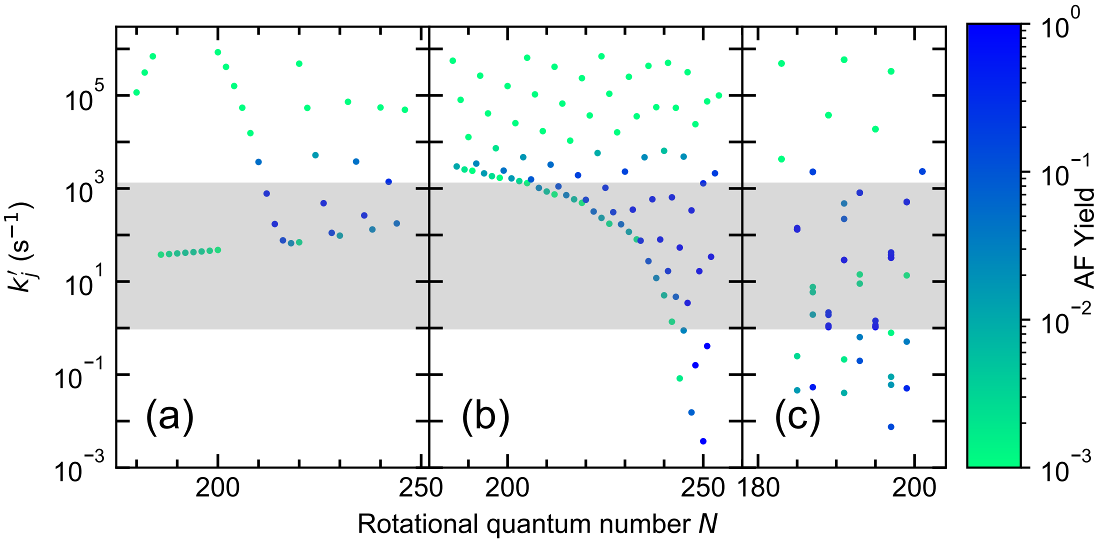

Figure 4.18: Levels in the anionic states (a) $X^2\Sigma_g^+$, (b) $A^2\Pi_u$, and (c) $C^4\Sigma_u^+$ undergoing AF. The total decay rates k'_j are plotted versus N and colour-coded according to their respective yields indicating their contribution to the measured AF signal. The grey-shaded area marks the measurement window in the experiment. Only rates with a yield of at least 10^{-3} are shown.

4.6.1 AD and AF yields

The yields for levels contribution to the measured AF signal are calculated using Eq. (4.39) and shown in Fig. 4.18. Here, the total decay rates k'_j are plotted versus the rotational quantum number N and colour-coded according to $Y_{f,j}$. Levels in states $X^2\Sigma_g^+$, $A^2\Pi_u$, and $C^4\Sigma_u^+$ are shown in panels (a), (b), and (c), respectively. The partial decay rates necessary to calculate k'_j (see Eq. (4.35)) were taken from the previous Secs. 4.3 - 4.5. A grey-shaded area in Fig. 4.18 marks the measurement window. The majority of rates lie either inside or above this area. This suggests, that the upper-bound approximation carried out in Eq. (4.38) is acceptable. For levels with $k'_j \gg t_1^{-1}$, the yield is strongly suppressed due to the exponential factor in Eq. (4.39). Higher-lying vibrational levels in the two doublet states $X^2\Sigma_g^+$ and $A^2\Pi_u$ have fast radiative decay rates (see Sec. 4.5.2), which limit the overall lifetime of these levels. As a result, $k'_j > 10\,\text{s}^{-1}$ for all levels in the $X^2\Sigma_g^+$ state and only very few display a strong yield for the AF signal. For excitations in the $A^2\Pi_u$, the total decay rates reach much lower values at high N due to the energetic rearrangement with the anionic ground state and the consequential longer radiative lifetimes (see Sec. 4.3.2). Here, the number of levels contributing significantly to the AF signal is higher than in $X^2\Sigma_g^+$. Due to the irregular scattering of radiative decay rates in

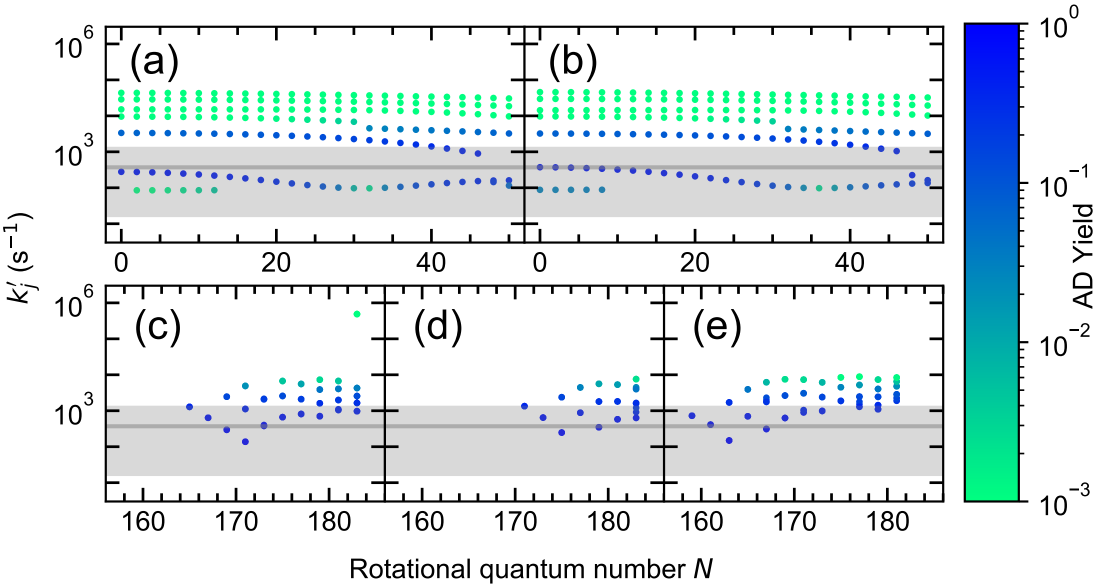

Figure 4.19: Yields for levels in C_2^- contributing to the AD signal. Panels (a) and (b) show levels in the $X^2\Sigma_g^+$ state using the neutral potentials from spectroscopic parameters or *ab initio* calculations to determine k_d, respectively. Panels (c), (d), and (e) display the AD rates for levels in the $C^4\Sigma_u^+$ state using the anionic potential which is unshifted, shifted up or shifted down, respectively. The grey-shaded area marks the measurement window in the experiment. The dark grey line indicates the main lifetime component of 2.7 ms (see Fig. 4.1). Only rates with a yield of at least 10^{-3} are shown.

the $C^4\Sigma_u^+$ state (see Sec. 4.3.3), no trends are visible for these levels in Fig. 4.18(c). Notably, even though the rotational excitation window with relevant levels for the AF signal is smaller than the doublet states, there are more k'_j with $Y_{f,j} \geq 0.1$ in the $C^4\Sigma_u^+$ state (39 rates) then in the other two combined (30 rates). This can be explained by the large scattering and often small values of the radiative decay rates for the spin-forbidden transition (see Sec. 4.3.3).

The yields for levels contribution to the measured AD signal are shown in Fig. 4.19. Again, the total decay rates and yields were calculated using the results from Secs. 4.3 - 4.5. A grey-shaded area marks the measurement window, while a dark grey line indicates the main AD component measured in the experiment of 2.7 ms (see Fig. 4.1). In panels (a) and (b), levels originating in the $X^2\Sigma_g^+$ ground state are shown. Here, AD rates were calculated using the spectroscopic or *ab initio* neutral potentials (see Sec. 4.5.2), respectively. In both cases, the majority of total decay rates lie above the measurement window and therefore do not contribute to the signal significantly. Levels with a good AD yield can be found for total decay rates spanning from $10^2 \lesssim k'_j \lesssim 5\times10^3$, with a large fraction lying below the dark grey line marking the main decay component measured in the experiments. Figs. 4.19(c) - (e) show AD levels in the $C^4\Sigma_u^+$ state using the unshifted, upwards and downwards shifted anionic potentials, respectively (see Sec. 4.5.3). The radiative and AF decay rates for levels relevant for the AD signal in the two shifted potentials were calculated explicitly for the modified curves in order to obtain more precise values of their yields. In contrast to the doublet AD rates, the total decay rates lie almost exclusively above the main decay component measured in the experiment. Typically, only one smaller k'_j value is present per potential, with this outlier closed to the dark grey line for the upwards shifted anionic curve. Overall, the total decay rates of levels from the $C^4\Sigma_u^+$ contributing to the AD signal display a smaller k'_j range and are fewer in number compared to those originating in the $X^2\Sigma_g^+$ ground state.

4.6.2 Internal population of the ions

A description of the internal population of the ions at any storage time is necessary to model the expected decay signal on the detector according to Eq. (4.37). To estimate this, multiple aspects will be considered in this sub-section. First, an appropriate initial population of the ions after production in the MISS source has to be chosen. Below, two different scenarios are discussed, one including and one excluding the production of ions in the $C^4\Sigma_u^+$ quartet state. Second, the evolution of the internal population with storage time has to be described mathematically. Here, the focus lies on levels, which can contribute to the measured decay signals (see Sec. 4.6.1). Third, the significance of repopulation of these levels from higher-lying levels has to be examined. Below, these three aspects are discussed separately.

Initial population

The processes leading to the creation of molecules in sputter sources remain somewhat elusive despite multiple approaches to describe underlying formation mechanisms [37, 99]. Nevertheless, the internal population distributions arising from this source environment have been studies for different system. Wucher [100] used experimental data available at the time to simulate the internal energy distribution of different sized neutral silver clusters. Here, he could find general features, which he again observed in a later collaborative study with Garrison [38]. One observation was, that the majority of the population can be approximated by a Boltzmann-distribution. However, a small fraction of the particles appear to have a non-thermal population with much higher energies then the quasi-thermal part. This non-thermal behaviour was also described in a study by Snowden et al. on neutral systems [37]. The second observation was the thermal decoupling of the different excitation modes. Here, only vibrational and rotational temperatures, T_v

and T_N, were studies, while electronic excitations were not considered. Both studies found, that vibrational and rotational distributions have different temperatures of a few thousand K with $T_v < T_N$.

The transfer of these studies on neutral molecules discussed above to anionic systems is not obvious. Due to the extraction potential applied in the sputter source, anionic species are accelerated out of the source instantly after ionization. In the subsequent experimental chambers, the pressure is typically much lower and the ions do not have the possibility to efficiently equilibrate their internal temperature through collisions. Apart from the works on neutral systems discussed above, only two studies on negative systems could be found in the course of this work, which tried to estimate the internal population of the anions after creation in a caesium sputter source. One looked at the auto-detachment of highly-excited SF_6^- [9]. Here, depending on the operation parameters of the source, temperatures of $T_v \approx 1000\,\mathrm{K}...3000\,\mathrm{K}$ and $T_N \approx 1000\,\mathrm{K}...4000\,\mathrm{K}$ were found. Due to the nature of the studied process (AD), this work focused on ions which can be expected to predominantly lie in the high-energy tail of the population distribution. However, it is important to note, that the EA of SF_6^- is about 1 eV [9] and therefore considerably smaller than for C_2^-. This could potentially lead to lower temperatures of the high-energy tail due to the reduced stability of the system. Another study [36] probed inner-shell excitations of C_2^- and was able to model the resulting spectrum well, assuming internal temperatures of $T_v \approx T_N \approx 1100\,\mathrm{K}$. In contrast to the SF_6^- study, it can be expected that predominantly ions in the quasi-thermal part of the population were probed here. Furthermore, Schipper et al. [36] observed that the electronic excitation does not follow a thermal distribution and the population is equally shared between the two states investigated in the experiments, the lowest-lying doublet states $X^2\Sigma_g^+$ and $A^2\Pi_u$ of C_2^-.

Considering the previous studies on internal populations of ion assembles produced in a sputter source described above, the initial population distribution used in this work is outlined below. The probability P_j to be in state j with electronic, rotational and vibrational excitation $j = (\gamma, N, v)$ is factorized into separate probabilities describing the different excitation types,

$$P_{\gamma,N,v} = P_\gamma \, P_N(\gamma) \, P_v(\gamma N). \tag{4.40}$$

The probability to be in electronic state γ, is given by a number $0 \leq P_\gamma \leq 1$. The probabilities to be in a specific rotational and vibrational excitation, $P_N(\gamma)$ and $P_v(\gamma N)$, are then dependent either on the electronic or the ro-electronic excitation of the system, respectively. Both are described by a two-component distribution, with one component accounting for the quasi-thermal, core part of the population with temperature T_i^c and one for the high-energy tail with temperature T_i^t,

$$P_i(m) = (1 - \alpha_i)p_i(m, T_i^c) + \alpha_i p_i(m, T_i^t). \tag{4.41}$$

Here, α_i is the fraction of ions in the high-energy tail, $i = v, N$, and $m = \gamma, \gamma N$. The thermal distribution p_i for $i = N$ and $m = \gamma$ is given by a Boltzmann distribution

$$p_N(\gamma, T) = \frac{(2N+1)e^{-E_N(\gamma)/k_BT}}{\sum_{N'}(2N'+1)e^{-E_{N'}(\gamma)/k_BT}}. \tag{4.42}$$

The denominator in Eq. (4.42) sums over all rotational excitations N' for which (quasi-)bound vibrational levels were calculated. The rotational excitation energy $E_N(\gamma)$ in electronic state γ can be calculated according to

$$E_N(\gamma) = E_{\gamma,N,v=0} - E_{\gamma,0,v=0}. \tag{4.43}$$

The thermal distribution of the vibrational levels ($i = v$, $m = \gamma N$) is given by

$$p_v(\gamma N, T) = \frac{e^{-E_v(\gamma N)/k_BT}}{\sum_{v'} e^{-E_{v'}(\gamma N)/k_BT}}. \tag{4.44}$$

The vibrational excitation energy $E_v(\gamma N)$ in electronic state γ with rotational excitation N is calculated with

$$E_v(\gamma N) = E_{\gamma,N,v} - E_{\gamma,N,v=0}. \tag{4.45}$$

The denominator in Eq. (4.44) accounts for the normalization. Here, the sum extends over all (quasi-)bound vibrational levels v' in electronic state γ for rotational excitation N. For Eq. (4.42), which describes the corresponding calculation for rotational excitation, all relevant ro-vibrational eigenvalues were calculated with the Numerov method [85]. However, the excitation energy of very high-lying vibrations ($v > 23$) at low rotational excitations were only estimated here. These levels are of no relevance to either of the measured decay signals due to fast AD and radiative decay rates. Additionally, they are very weakly populated due to their large vibrational excitation. Hence, it is sufficient to approximate their energetic position for the normalization in Eq. (4.44). This approximation was carried out by Apl. Prof. Dr. Andreas Wolf, Max-Planck-Institut für Kernphysik, and is detailed in the Supplement Material of [90]. It only had a noticeable effect for vibrational temperatures in excess of 10 000 K. Levels shown in the later Fig. 4.20, which displays two population models, are only those calculated with the Numerov method.

Two initial population scenarios were derived in the course of this work and are given in Tab. 4.11 and displayed in Fig 4.20. For both the available parameters (P_γ, T_i and α_i) were adjusted to optimize the agreement between a decay model and the measured data (see Sec. 4.6.3). Scenario 1 includes a small fraction (0.006) of the ions in the $\mathrm{C}^4\Sigma_u^+$ state of the system with the rest of the ions equally distributed between the lowest two doublet states $\mathrm{X}^2\Sigma_g^+$ and $\mathrm{A}^2\Pi_u$. As discussed in Sec. 4.5.3, only levels in the $\mathrm{C}^4\Sigma_u^+$ state with rotational excitation N which lie below the ZPE of the $\mathrm{A}^3\Pi_u$ state with $N_n = N-4$ have sufficient AD lifetimes to reach the CSR. Therefore, only

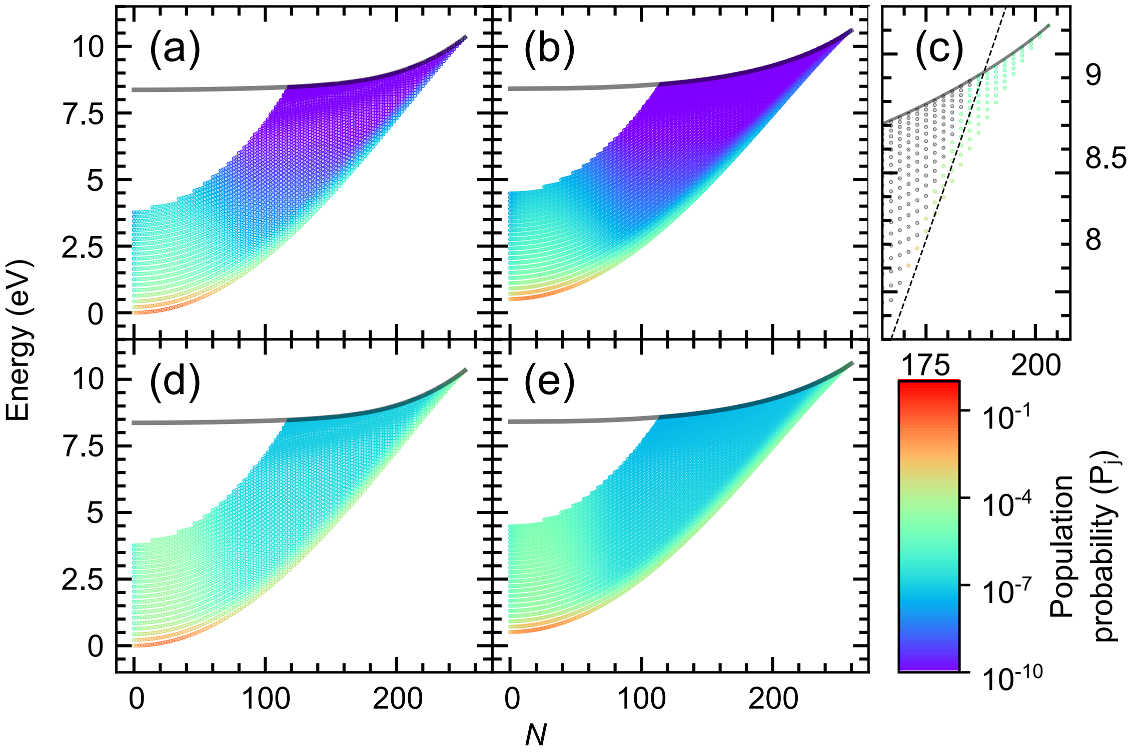

Figure 4.20: Populations of ro-vibronic levels for scenario 1 in panels (a) - (c) and scenario 2 panels (d) - (e). The levels are plotted according to their excitation with respect for the ZPE of the ground state at $N = 0$ versus the rotational excitation and colour-coded according to their population. A black semi-transparent line marks the maximum of the rotational barrier for the respective electronic state at rotational excitation N. Levels in the $X^2\Sigma_g^+$ ground state are shown in panels (a) and (d), while levels in the $A^2\Pi_u$ state are shown in panels (b) and (e). For scenario 1, levels in the upwards shifted potential of $C^4\Sigma_u^+$ are shown in panel (c). Those which can undergo AD only by ejecting an electron with $l \geq 6$ are considered in the model. Levels which detach with $l < 6$ are indicated in grey and not considered from here on. Relevant levels in the $C^4\Sigma_u^+$ state lying above the thin dashed line, which marks the ZPE for the $A^3\Pi_u$ state with $N_n = N - 6$, undergo AD with $l = 6$.

these levels are considered in the calculation of the population fraction in the $C^4\Sigma_u^+$ state. Furthermore, in scenario 1, the temperatures and fractions of the high-energy tails were chosen such that they are not in contradiction with previous studies on internal populations arising from sputter sources.

Scenario 2 only allows the population of the two doublet states in equal measures and no population of the lowest quartet state. The temperatures and tail fractions

Table 4.11: Description of the two initial population scenarios, one with and one without a small fraction of the ions in the $C^4\Sigma_u^+$ state of the system. Parameters given here can be used together with the equations given in the text to calculate the respective population distributions.

	P_γ	T_N^c (K)	T_v^c (K)	α_N	T_N^t (K)	α_v	T_v^t (K)
	Scenario 1						
$X^2\Sigma_g^+$ and $A^2\Pi_u$	0.497	2100	1200	0.01	8000	0.01	8000
$C^4\Sigma_u^+$	0.006	2100	1200	0	-	0	-
	Scenario 2						
$X^2\Sigma_g^+$ and $A^2\Pi_u$	0.5	2100	1200	0.035	30 000	0.05	30 000
$C^4\Sigma_u^+$	0	-	-	-	-	-	-

(see Eq. (4.41)) were then adjusted in such a way, that the modelled AD and AF curves reproduce the measured signal as good as possible when employing the decay rates calculated in Secs. 4.3 - 4.5. This will be discussed in more detail in Sec. 4.6.3. Here, forbidding a small population in the quartet state led to the necessity of increasing both the tail fractions and temperatures of the high-energy tails in a way, which is no longer supported by previous studies on internal populations created in sputter source environments discussed above. Nevertheless, this scenario will be employed as well to fit the measured data in Sec. 4.6.3 to illustrate the importance of including the $C^4\Sigma_u^+$ state into the model.

Storage time evolution of the population

Having defined the initial population of the ions above, the evolution of this population with storage time t will be approximated here. Considering an arbitrary state j, its relative population P_j changes according to

$$\frac{dP_j}{dt} = -k_j' P_j, \tag{4.46}$$

if repopulation through radiative decay by higher-lying levels is neglected. The total decay rate k_j' is calculated according to Eq. (4.35). Assuming an initial relative population P_j^0, the time-dependent relative population of j, $P_j(t)$, is given by the integral of Eq. (4.46)

$$P_j(t) = P_j^0 e^{-k_j' t}. \tag{4.47}$$

The two different initial population scenarios for P_j^0 employed here are given above.

In order to estimate the effect of repopulation from higher-lying states, it is necessary to expand Eq. (4.46) to

$$\frac{dP_j}{dt} = -k'_j P_j + \sum_i A^i_j P_i. \tag{4.48}$$

Here, the first term describes the depopulation of j through any of the three decay channels (see Eq. (4.35)). The second term considers the repopulation from all higher-lying states i with population P_i. The corresponding rates A^i_j are the partial radiative decay rates of i into j (see Sec. 4.3). From here on, only a single repopulation step into j will be considered and the possible repopulation of the feeding levels i will be neglected. As discussed later in this Sec. 4.6.2, this approximation is sufficient due to the very small overall repopulation effect for levels contributing to the measured signals. With this simplification, P_i in Eq. (4.48) can be rewritten using Eq. (4.47),

$$\frac{dP_j}{dt} = -k'_j P_j + \sum_i A^i_j \, P^0_i \, e^{-k'_i t}. \tag{4.49}$$

Eq. (4.49) is a linear first-order differential equation of the form

$$\frac{df(t)}{dt} = f(t)g(t) + h(t), \tag{4.50}$$

for which the integral is given by

$$f(t) = c_0 e^{G(t)} + e^{G(t)} \int e^{-G(\tilde{t})} \, h(\tilde{t}) \, d\tilde{t}. \tag{4.51}$$

Here, c_0 is a constant and $G(t)$ the integral of $g(t)$ over t. For Eq. (4.49), $G(t)$ is given by

$$G(t) = \int g(t)dt = \int -k'_j \, dt = -k'_j \, t. \tag{4.52}$$

Substituting also the other two functions $f(t) = P_j(t)$ and $h(t) = \sum_i A^i_j P^0_i e^{-k'_i t}$ and choosing $c_0 = P^0_j$, Eq. (4.51) can be employed to solve Eq. (4.49):

$$\begin{aligned} P_j(t) &= P^0_j e^{-k'_j t} + e^{-k_j t} \left(\sum_i \int e^{k'_j \tilde{t}} \, A^i_j \, P^0_i \, e^{-k'_i \tilde{t}} \, d\tilde{t} \right) \\ &= \left[P^0_j + \sum_i A^i_j \, P^0_i \int e^{-(k'_i - k'_j)\tilde{t}} d\tilde{t} \right] e^{-k'_j t}. \end{aligned} \tag{4.53}$$

Integrating $\tilde{t}$ from 0 to t and after carefully examination of the contributing total decay rates k'_j and k'_i to ensure that $\left| k'_i - k'_j \right| > 0$ to avoid divergence, the population function of a state j allowing a single repopulation step can be written as

$$P_j(t) = \left[P^0_j + \sum_i A^i_j \, P^0_i \, \frac{1 - e^{-(k'_i - k'_j)t}}{k'_i - k'_j} \right] e^{-k'_j t}. \tag{4.54}$$

Discussion on repopulation

In contrast to the two destructive decay channels, AD and AF, radiative de-excitation does not lead to ion loss in the experiment. Instead, these ions populate a different excited state after the decay, which could in principle contribute to the measured signal. Therefore, the effect of repopulation through the "feeding" from energetically higher-lying levels into levels relevant for the two signals measured in the experiment will be considered here.

For the $\mathrm{C}^4\Sigma_u^+$ state, it is quite intuitive to see, that repopulation from higher-lying levels is not relevant in the measurement window studied here. Spin-allowed radiative transitions would only be possible from higher-lying quartet states. While these have been predicted in calculations [15, 79], they are thought to lie multiple eV above the $\mathrm{C}^4\Sigma_u^+$ state and are therefore not expected to loose their resonant character at high rotational excitations. As a result, ions in these states undergo resonant AD before leaving the sputter source. Consequentially, only the $\mathrm{X}^2\Sigma_g^+$ doublet ground state remains as a possible feeding source for repopulation. However, for levels in this state the spin-allowed radiative transition to the $\mathrm{A}^2\Pi_u$ state is also available and multiple orders of magnitude stronger than the spin-forbidden decay into the quartet state. Therefore, repopulation can be neglected for levels in $\mathrm{C}^4\Sigma_u^+$.

For levels in the two doublet states, $\mathrm{X}^2\Sigma_g^+$ and $\mathrm{A}^2\Pi_u$, the relevance of repopulation for the decay signals is much less obvious. The spin-allowed decay between the two states potentially offers an efficient feeding channel. However, the situation is different for the two decay processes. In the case of AD from high vibrations with moderate rotational excitation in the $\mathrm{X}^2\Sigma_g^+$ state, see Sec. 4.5.2, feeding is not relevant for the measurement window considered here. These levels can only be populated by higher-lying vibrations in the $\mathrm{A}^2\Pi_u$ or $\mathrm{B}^2\Sigma_u^+$ states, which both exhibit radiative lifetimes much shorter than the start of the measurement window at $\sim 0.8\,\mathrm{ms}$ (see Secs. 4.3.1 and 4.3.2). Therefore, the repopulation could only change the number of ions in the levels decaying through this AD channel at the beginning of the measurement. However, it could not influence the time dependence of the signal. Additionally, these feeding levels can also undergo AD. For the $\mathrm{B}^2\Sigma_u^+$ state this destructive decay is much faster than radiative de-excitation while only an upper rate limit of $1\times10^8\,\mathrm{s}^{-1}$ is known for levels in the $\mathrm{A}^2\Pi_u$ state [13]. Repopulation will therefore also be neglected for AD from the $\mathrm{X}^2\Sigma_g^+$ state.

For levels in the doublet states contributing to the AF signal, very high rotational excitations are required. Here, the radiative decay rates differ strongly in comparison to the low-N case (see Sec. 4.3.2). Hence, repopulation is considered in the results presented in the next Sec. 4.6.3 for this decay channel. A comparison with and without one cascade step in the population model shows, that this process only has a small effect on the overall modelled signal. For population scenario 1 (see Tab. 4.11), the integral of the modelled signal increases by a relative fraction of $\sim 5.2 \times 10^{-7}$ when feeding is included in the model. This is predominantly due to the small overall contribution of doublet levels to this decay channel for scenario 1 (see Sec. 4.6.3). In the doublet-only scenario 2 (see Tab. 4.11), the relative increase of the integral of the modelled signal is much higher with $\sim 1.2 \times 10^{-2}$. However, it does not significantly affect the storage time evolution or magnitude of the signal. A closer inspection reveals, that the repopulation is predominantly driven by the radiative decay from $\mathrm{X}^2\Sigma_g^+$ to $\mathrm{A}^2\Pi_u$ levels. This can be understood by the rearrangement of the two doublet states at high N (see Sec. 4.2.3). As a result, levels in the $\mathrm{X}^2\Sigma_g^+$ state typically sit more deeply in the potential than the levels in the $\mathrm{A}^2\Pi_u$ state they radiatively decay to. Consequentially, they exhibit longer AF lifetimes and are therefore more likely to repopulate the lower-lying level. Levels in the $\mathrm{A}^2\Pi_u$ state on the other hand typically have faster AF rates than the levels they are potentially feeding. As a result, vibrations in this state which lie high enough to repopulate levels in the $\mathrm{X}^2\Sigma_g^+$ state that contribute to the AF signal typically auto-fragment on time-scales shorter than the lower limit of the measurement window.

4.6.3 Comparison between experiment and model

Using Eq. (4.37) and the internal population model derived in Sec. 4.6.2, the expected signals measured on the detector at the CSR (see Sec. 4.1) can be estimated. The measured signal at the charged fragment position of the detector $s_c(t)$ can be directly compared to the modelled AF curve $s_f(t)$:

$$s_c(t) = s_f(t). \tag{4.55}$$

For the measured neutral signal $s_n(t)$, the sum of the modelled AD signal $s_d(t)$ and $s_f(t)$ has to be calculated. Here, the AF signal is scaled by $\eta = 0.75$ to match the experimental conditions (see Fig. 4.2):

$$s_n(t) = s_d(t) + \eta s_f(t). \tag{4.56}$$

Below, the modelled signals will be compared to the experimental data for the two different initial population scenarios outlined in Sec. 4.6.2.

Population scenario 1

Fig. 4.21 shows the comparison between the experimental and modelled signals using population scenario 1 (see Tab. 4.11). Here, it is assumed that a small fraction of ions occupy the $\mathrm{C}^4\Sigma_u^+$ quartet state of C_2^-. The AF signals are shown in panel (a). The AF yields for the three anionic states displayed in Fig. 4.18 were used for the model. The overall modelled signal (solid blue line) reproduces the measurement reasonably well. The AF model is dominated by contributions from levels in the $\mathrm{C}^4\Sigma_u^+$ state, which are drawn individually with grey lines in the figure. The underlying overall decay rates k' of these levels are distributed over the entire measurement window

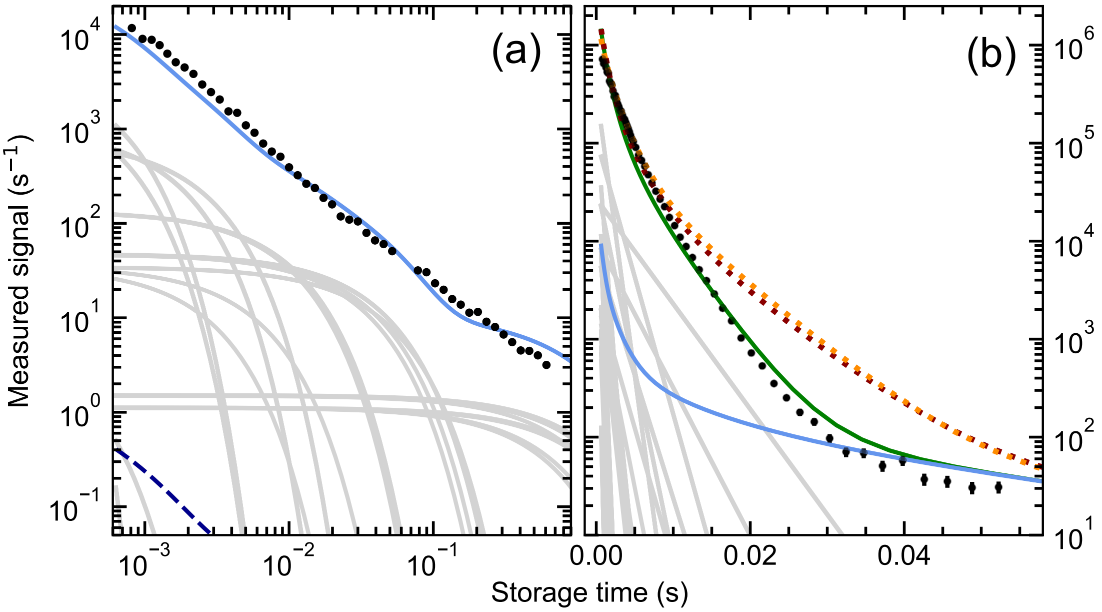

Figure 4.21: Comparison of measured decay signals (black dots) and the simulation using population scenario 1. (a) Fragmentation signal $s_f(t)$ with the model including all levels shown in a solid blue line. Grey lines mark decay signals from individual quartet levels. The dashed, dark-blue line marks the entire contribution from all doublet levels ($X^2\Sigma_g^+$ and $A^2\Pi_u$). (b) Neutral signal $s_n(t)$ using the sum of AD and AF curves. The model employing the AD rates from the quartet potential shifted upwards is shown in a solid green line. The corresponding modelled signals for the unshifted/downward-shifted quartet potential are shown in dark red/orange dotted lines. The solid blue line marks the modelled fragmentation signal $s_f(t)$ from (a), grey lines indicate the AD signal from individual quartet levels for the upwards shifted potential.

resulting in a power-law behaviour of the signal. This might be surprising at first, due the small number of ro-vibrational levels contributing for this electronic state. However, as discussed in Sec. 4.3.3, the large scatter of radiative decay rates even for fine-structure levels with the same ro-vibrational excitation results in the large spread and reasonable density of k' observed here. A dashed dark blue line in Fig. 4.21(a) indicates the total contribution of all levels in the two doublet states, $X^2\Sigma_g^+$ and $A^2\Pi_u$. It is multiple orders of magnitude weaker than the dominant contributions from the quartet state. This weak contribution can be explained by the small population probability of the doublet levels undergoing AF in scenario 1 (see Fig. 4.20).

In Fig. 4.21(b), the neutral signals $s_n(t)$ are compared for population scenario 1.

The model is given by the sum of the calculated AF signal $s_f(t)$ from panel (a) and the AD signal $s_d(t)$ (see Eq. (4.56)). Former is additionally drawn individually in a blue line in the plot. For the AD part of the neutral signal, the three sets of decay rates stemming from the slightly different shapes of the quartet curve (see Sec. 4.5.3 and Fig. 4.3) are considered separately. The corresponding yields were taken from Fig. 4.19. Three modelled neutral curves are given in Fig. 4.21(b) in dotted orange, dotted dark-red, and solid green lines corresponding to the unshifted, downwards shifted and upwards shifted quartet curve, respectively. The signal corresponding to the upwards shifted potential (solid green) reproduces the measured data reasonably well. The rate sets for the other two $\mathrm{C}^4\Sigma_u^+$ potentials result in AD signals, which strongly overestimate the count rate for $t \gtrsim 10\,\mathrm{ms}$. At those storage times, the modelled signal is dominated by only one component with an overall decay rate $k' < 300\,\mathrm{s}^{-1}$, smaller than the fitted rate of the measured signal (see Fig. 4.1). As discussed in Sec. 4.6.1, the decay rate of this longest lived component in the model is closest to the fitted rate for the upwards shifted potential, resulting in the best agreement with the data. Independent of the employed $\mathrm{C}^4\Sigma_u^+$ potential curve, the modelled AD signal is predominantly caused by levels from the $\mathrm{C}^4\Sigma_u^+$ state. Individual contributions of these for the upwards-shifted potential are drawn in grey lines in the figure.

Even though only 0.6% of the ions are in the $\mathrm{C}^4\Sigma_u^+$ state of the system in this population scenario, both decay channels are dominated by contributions from this state in the model. This can be understood by the large ro-vibrational excitation necessary in both doublet states to contribute to either of the measured signals. As a result, the population probability of the relevant levels in both states is strongly suppressed (see Fig. 4.20). This also influences the effect of repopulation on the measured signal, which was found to be negligible for this population scenario (see Sec. 4.6.2). Therefore, no comparison of the modelled signals with and without repopulation are carried out in Fig. 4.21, since they would be indistinguishable in the plot.

Population scenario 2

Fig. 4.22 shows the comparison between the experimental and modelled signals using population scenario 2 (see Tab. 4.11). Here, the ions are equally distributed between the two doublet states $\mathrm{X}^2\Sigma_g^+$ and $\mathrm{A}^2\Pi_u$, while the $\mathrm{C}^4\Sigma_u^+$ quartet state is not populated. Panel (a) of Fig. 4.22 shows the AF signals $s_f(t)$. Individual contributions to the modelled signal are drawn in solid/dashed lines for levels originating in the $\mathrm{X}^2\Sigma_g^+/\mathrm{A}^2\Pi_u$ state of the system. As was expected from the yields of the two states, see Fig. 4.18, levels in the $\mathrm{A}^2\Pi_u$ state contribute more strongly to the AF signal than those in the $\mathrm{X}^2\Sigma_g^+$ state. The overall model including one cascade step of repopulation is drawn in a solid blue line. A dashed, dark-blue line indicates the model neglecting repopulation. The difference between the two is not significant,

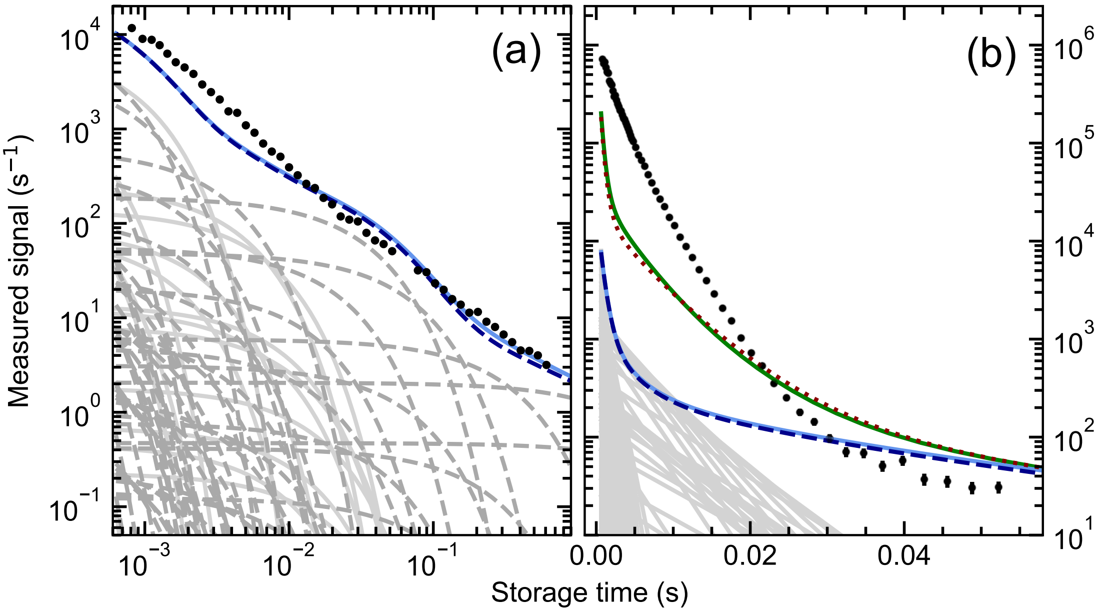

Figure 4.22: Comparison of measured decay signals (black dots) and the simulation using population model 2. (a) Fragmentation signal $s_f(t)$ with the model containing all levels and including/excluding feeding shown in a solid/dashed blue line. Decay signals from individual levels in the $X^2\Sigma_g^+$ and $A^2\Pi_u$ states are shown in solid light grey and dashed dark grey lines, respectively. (b) Neutral signal $s_n(t)$ with the model including all levels and AD rates for the spectroscopic neutral potential curves shown in a solid green line. The model using the *ab initio* neutral potentials for the AD rate calculations is plotted in a dotted dark red line. Grey lines indicate the decay of individual levels in the $X^2\Sigma_g^+$ state using the spectroscopic neutral potentials. The solid/dashed blue line is the fragmentation signal $s_f(t)$ including/excluding feeding from (a).

but visible in the plot. Neither of the modelled AF signals (with and without repopulation) reproduces the time-dependence of the measured data as well as scenario 1 discussed above.

In panel (b) of Fig. 4.22, the neutral signals are displayed. These are again the sum of products from both the AD and AF decay channels (see Eq. (4.56)). The modelled AF curves from panel (a), one including and one excluding repopulation, are drawn individually here. The overall neutral model including both AF and AD signals is drawn separately for the two different sets of AD rates for levels originating in the $X^2\Sigma_g^+$ state. The modelled signal corresponding to the rates, which employ the spectroscopic neutral potentials is drawn in a solid green line. Meanwhile, the model using the *ab initio* neutral potentials for the AD rate calculation is drawn in a dotted, dark-red line. Both models display a very similar time-dependency and do not reproduce the measured signal. In contrast to the AD model dominated by $C^4\Sigma_u^+$ levels (scenario 1, see Fig. 4.21(b)), the disagreement here is not due to a single longer-lived component in the beam. Instead, many levels contributing to the AD signal in scenario 2 have overall decay rates k', which are incompatible with the measured signal. This can be seen in Fig. 4.22(b) in form of the grey lines, which indicate the individual contributions of levels for the calculations employing the spectroscopic neutral potentials, as well as in the AD yields for this state displayed in Fig. 4.19.

4.7 Discussion

The origin of the nearly-exponential AD signal of highly excited C_2^- anions has remained elusive for multiple decades. The calculations presented in this chapter aim to finally identify the underlying mechanism and the initial levels of both this AD process as well as the AF signal measured at the CSR facility (see Sec. 4.1). To achieve this goal, decay rates for a wide range of ro-vibronic states in the C_2^- dimer were considered and the vast majority also explicitly calculated here.

The three well understood doublet states of the system were investigated as a possible origin for the measured signals for a wide range of ro-vibrational excitations. The second excited $B^2\Sigma_u^+$ state could be excluded as a possible source early on in the study due to its insufficient lifetime at any internal excitation. For the lower-lying doublet states, $A^2\Pi_u$ and $X^2\Sigma_g^+$, radiative decay rates were calculate for a large range of rotational excitations N. Here, it was found, that the two states energetically rearrange at high rotational excitations ($N \gtrsim 220$, see Sec. 4.2.3). This strongly effects the radiative lifetimes of both states (see Sec. 4.3.2). Furthermore, at these high rotations, auto-fragmentation rates for a wide range of ro-vibrational levels were calculated (see Sec. 4.4.1). Additionally, at low to moderate rotational excitation, the possibility of AD of the $X^2\Sigma_g^+$ was considered. Rate calculations for this process, which requires strong vibrational-electronic coupling, are presented in Sec. 4.5.2. A model was then constructed to estimate the detector count rates in the experiment using all the derived decay rates (AD, AF, radiative relaxation, see Sec. 4.6). Even when allowing unrealistic population scenarios (temperatures $T > 10\,000\,\mathrm{K}$ and tail fractions $\alpha > 0.01$) in order to boost the agreement between the models for the neutral and charged count rate and the measured signals, both modelled signals still differed strongly from the experimental data (see Fig. 4.22). Especially the nearly exponential shape of the AD signal could not be reproduced at all. The AF model is also in poor agreement with the measured data. Based on these results, neither the measured AD nor AF signal are predominantly caused by the three doublet state of C_2^- with a high degree of probability.

If none of the known bound states of C_2^- are responsible for the measured signals, the origin has to lie elsewhere. Based on previous theoretical works [15, 78, 79], any additional electronic states of the dimer are resonances, which lie in the detachment continuum. Due to their energetic position above a neutral state to which they have a spin-allowed decay channel, these states are expected to live on atomic timescales, which are inaccessible for the experiments discussed in this work. However, calculations presented here show, that at high rotational excitation the lowest resonance, the $C^4\Sigma_u^+$ quartet state, energetically rearranges with the $A^3\Pi_u$ neutral state. This is the lowest neutral state into which it can detach. As a result, levels in this state become metastable with respect to auto-detachment and hence are a possible source for the measured signals.

Different decay channels are available for these metastable levels in the $C^4\Sigma_u^+$ state at high rotation. One is radiative relaxation. Due to the lack of lower-lying quartet states, this decay is only possible through the admixture of the $A^2\Pi_u$ state enabled by spin-orbit coupling. This in turns facilitates the decay to the $X^2\Sigma_g^+$ ground state. The mathematical description of this process was not available in the literature and is presented in Sec. 4.3.3 and Appendix 2B of [90]. The resulting radiative rates show fluctuations over multiple orders of magnitude both for the fine-structure levels within one ro-vibrational excitation as well as different excitations (see Fig. 4.9). All radiative rates calculated here are sufficiently small to allow the observation of signals from these levels in the measurement. Furthermore, auto-fragmentation calculations carried out in Sec. 4.4.1 found a group of levels which have AF rates matching the timescales of the experiment.

The energetic rearrangement with the neutral curve prohibits the auto-detachment of $C^4\Sigma_u^+$ levels by AD mechanisms previously discussed in literature. However, detachment is still energetically accessible through the coupling to neutral levels with significantly smaller rotational excitation than the anionic system. Here, the ejected electron has to carry away the excess rotational excitation. The mechanism, rotationally assisted auto-detachment, is described in this work in Sec. 4.5.3 and in [95] for the first time. It produces AD rates, which are very similar for levels that require the same minimal angular momentum for the ejected electron l. These lie within one to two orders of magnitude of each other. However, rates corresponding to different l values differ by multiple orders of magnitude. This could in principle enable a nearly exponential time-dependency for a superposition of levels from one l value alone. Additionally, AD rates corresponding to the ejection of an electron with $l = 6$ are very similar to the time dependence of the measured AD signal.

In order to estimate the feasibility of the $C^4\Sigma_u^+$ state as the origin for the measured AD and AF signals, another population scenario was derived. Here, a small fraction of ions (0.6 %) populate the metastable levels in the quartet state at the beginning of the measurement. In contrast to the population scenario described above for the doublet states alone, the rotational and vibrational temperatures for this scenario were chosen in accordance with available knowledge of internal populations in sputter sources. The resulting modelled decay signals match the measured data reasonably well and significantly better than the doublet-states-only model. For both the AD and AF signals, the model is dominated by levels originating in the $C^4\Sigma_u^+$ state.

This agreement between the measured and modelled signals is remarkable, considering the amount of uncertainty in the underlying calculations. No experimental data on the $C^4\Sigma_u^+$ state of C_2^- is currently available. Consequentially, only theoretical results for both the shape and the energetic position of this potential were employed here. The calculation of all of the decay rates (AD, AF and radiative relaxation) are strongly and non-trivially dependent on both of these parameters. The good agreement with the measured data with only minimal alterations to the quartet curve parameters is therefore not only an indication for the excellent underlying *ab initio* calculation by Ass. Prof. Dr. Milan Ončák. It is also a strong indication, that even better agreement between model and measurement can be achieve if the quartet potential is adjusted accordingly.

The results of the calculations presented in this chapter strongly suggest, that both the measured AD and AF signal is predominantly caused by levels originating in the $C^4\Sigma_u^+$ state. These become metastable with respect to auto-detachment for high rotational excitations. In order to gain a better understanding of this quartet state, experimental data is necessary. Especially spectroscopy experiments focusing on transition involving the $C^4\Sigma_u^+$ state could offer more insights into its shape and energetic positions. A recent publication by Iizawa et al. at the RICE storage ring in Japan [19] most likely already provides a first such study. Here, the authors point to a multitude of unidentified lines in their spectra. They suggest that a sub-set of those, which display lifetimes in a window of $1.5 - 3.0\,\mathrm{ms}$, could be the cause for the AD signal also reported in the paper (see Fig. 4.1(c)). Furthermore, they report on a second sub-set of unidentified lines with lifetimes of more than 10 ms. These lifetimes were also reported to strongly scatter, which would fit the pattern of the spin-forbidden radiative decay rates derived in Sec. 4.3.3. For the electronic transition probed in the experiment, Iizawa et al. proposed a coupling from the $C^4\Sigma_u^+$ state to a higher-lying $^4\Delta_u$ state. However, this is unlikely, since both states have the same *ungerade* parity (see Sec. 4.3). A previous study by Shi et al. [15] identified a $^4\Sigma_g^+$ state roughly $20\,000\,\mathrm{cm}^{-1}$ above the $C^4\Sigma_u^+$ state. Here, dipole- and spin-allowed transitions would be possible and the excitation energy between the two quartet states also roughly matches that of the measured lines ($\sim 18\,000\,\mathrm{cm}^{-1}$). A stringent comparison of the calculated energy separation between the two quartet states of [15] and the energy of the unidentified transitions in [19] would not be advisable here, since the measured transitions most likely involve states of high rotational excitation. As discussed in Sec. 4.2.3, the potential landscape can be very different at those N and therefore the energetic separation might differ from the rotationless case discussed in the *ab initio* calculations by Shi et al.. Therefore, additional experiments as well as a detailed theoretical studies of these quartet levels at high rotational excitations are necessary. It is clear that there are still new and interesting things to discover about history's most studied molecular anion.

5 Summary and Outlook

Within this thesis two research topics have been addressed. One is the implementation of the first isochronous operation of the CSR in Chap. 3. This also presents the first isochronous operation of any electrostatic storage ring. The method is used for the identification of the different species stored inside the device. It has a sufficient resolution to resolve molecular isobars with relative mass differences of $\Delta m/m \gtrsim 10^{-5}$. Furthermore, a sensitivity of relative beam fractions below 10^{-3} could be reached in the measurements. Since its implementation, this method has become a standard tool to measure the ion beam composition used prior to all measurements carried out at the CSR. It has also enabled studies at the facility, which would not have been possible to this extent otherwise [47, 62, 101]. This project additionally includes first tests to remove unwanted contaminants from the stored beam. Further development of different beam-cleaning methods is still ongoing as are additional investigations of the performance of the CSR in isochronous operation.

The second project focused on the study of the decay of highly-excited C_2^- anions and is discussed in Chap. 4. Here, the goal was the identification of the origins of the auto-detachment signal measured at multiple ion storage facilities since the 1990s including the CSR, as well as the auto-fragmentation signal, recorded at the CSR. The calculations presented in this thesis strongly suggests, that the lowest quartet electronic state of the system, $\mathrm{C}^4\Sigma_u^+$, is predominantly responsible for both measured signals. This state is of resonant character at moderate rotational excitations, but was found here to become metastable with respect to auto-detachment at high rotational excitation. A subset of levels in this state could be identified, which detach their excess electron on the millisecond timescale observed in the different experiments [16, 17, 18, 19]. The underlying mechanism of rotationally assisted auto-detachment has been described for the first time in the course of this project.

The successful assignment of the newly discovered process of rotationally assisted auto-detachment to the millisecond AD signal of C_2^- raises the question, if this decay channel can also be observed in other systems. As discussed in Sec. 4.5.3, the ejection of electrons in high angular momenta is strongly suppressed, if a detachment channel corresponding to a lower value of the angular momentum of the ejected electron is available. Therefore, this process can only be observed in levels, for which AD is possible exclusively when the electron carries away multiple quanta of rotational excitation. Based on the results presented in Chap. 4, a list of criteria can be drawn up for electronic states with similar properties than the $\mathrm{C}^4\Sigma_u^+$ state of C_2^-, which could potential support levels displaying rotationally assisted AD:

- The state has to lie above at least one neutral state into which it can detach at its equilibrium distance R_0 in the absence of rotation excitation ($N = 0$).
- The potential has to intersect with all lower-lying neutral states, into which it can detach, at internuclear distances close to (but above) its equilibrium distance $R_0(N = 0)$. The restriction on the intersection point(s) is necessary here in order to ensure that the potential is still sufficiently deep after the energetic rearrangement to support vibrational levels. If the rearrangement only occurs at large internuclear distances, the rotational excitation necessary would result in an anionic curve, which is completely dissociative.
- Radiative transitions inside the state and to lower-lying electronic states have to be sufficiently slow. In the case of homo-nuclear dimers, where transitions inside the same electronic state are dipole-forbidden, this would necessitate that there are either no lower-lying electronic states or that these have, e.g., a different spin than or the same u/g symmetry as the state of interest.

An initial scan of the available literature indicated a $^4\Sigma_u^-$ state of the anionic sulphur dimer, S_2^-, as a potential candidate [102]. However, preliminary tests carried out at the CSR in March 2024 could not verify this assumption. In general, the search for potential candidates proved difficult, since the available *ab initio* calculations published on anionic systems often do not include electronic states in the detachment continuum. Results presented in this thesis will hopefully serve as a motivation to also investigate low-lying detachment resonances in future calculations.

List of publications

Parts of this thesis have been published or prepared in the following articles

- M. Grieser, **V. C. Schmidt**, K. Blaum, F. Grussie, R. von Hahn, Á. Kálosi, H. Kreckel, D. Müll, O. Novotný, F. Nuesslein, A. Wolf, "Isochronous mass spectrometry in an electrostatic storage ring", Rev. Sci. Instrum. 93, 6, 063302 (2022), `https://doi.org/10.1063/5.0090131`
- **V. C. Schmidt**, R. Čurík, M. Ončák, K. Blaum, S. George, J. Göck, M. Grieser, F. Grussie, R. von Hahn, C. Krantz, H. Kreckel, O. Novotný, K. Spruck, A. Wolf, "Unimolecular processes in diatomic carbon anions at high rotational excitation", *to be submitted to Phys. Rev. A*, `https://doi.org/10.48550/arXiv.2405.06493`
- **V. C. Schmidt**, R. Čurík, M. Ončák, K. Blaum, S. George, J. Göck, M. Grieser, F. Grussie, R. von Hahn, C. Krantz, H. Kreckel, O. Novotný, K. Spruck, A. Wolf, "Autodetachment of diatomic carbon anions from long-lived high-rotation quartet states", *to be submitted to Phys. Rev. Lett.*, `https://doi.org/10.48550/arXiv.2405.06514`

Additional publications with own contributions:

- D. Müll, F. Grussie, K. Blaum, S. George, J. Göck, M. Grieser, R. von Hahn, Z. Harman, Á. Kálosi, C. H. Keitel, C. Krantz, C. Lyu, O. Novotný, F. Nuesslein, D. Paul, **V. C. Schmidt**, S. Singh, S. Sunil Kumar, X. Urbain, A. Wolf, H. Kreckel, "Metastable states of Si^- observed in a cryogenic storage ring", Phys. Rev. A 104 , 3, 032811 (2021), `https://link.aps.org/doi/10.1103/PhysRevA.104.032811`
- Á. Kálosi, L. Gamer, M. Grieser, R. von Hahn, L. W. Isberner, J. I. Jäger, H. Kreckel, D. A. Neufeld, D. Paul, D. W. Savin, S. Schippers, **V. C. Schmidt**, A. Wolf, M. G. Wolfire, O. Novotný, "Dissociative Recombination of Rotationally Cold OH^+ and Its Implications for the Cosmic Ray Ionization Rate in Diffuse Clouds", ApJL 955, 2, L26 (2023), `https://dx.doi.org/10.3847/2041-8213/acf71d`

Bibliography

[1] A. Avogadro, “Essay on a manner of determining the relative masses of the elementary molecules of bodies, and the proportions in which they enter into these compounds,” *Journal de physique*, pp. 58–76, 1811.

[2] K. P. Huber and G. Herzberg, *Molecular Spectra and Molecular Structure: IV. Constants of Diatomic Molecules.* Van Nostrand Reinhold Inc., 1979.

[3] NIST, “NIST Chemistry WebBook.” `https://webbook.nist.gov/chemistry/`.

[4] B. A. McGuire, “2021 census of interstellar, circumstellar, extragalactic, protoplanetary disk, and exoplanetary molecules,” *The Astrophysical Journal Supplement Series*, vol. 259, p. 30, mar 2022.

[5] J. Fedor, K. Hansen, J. U. Andersen, and P. Hvelplund, “Nonthermal Power Law Decay of Metal Dimer Anions,” *Phys. Rev. Lett.*, vol. 94, p. 113201, Mar 2005.

[6] K. Hansen, J. U. Andersen, P. Hvelplund, S. P. Møller, U. V. Pedersen, and V. V. Petrunin, “Observation of a $1/t$ decay law for hot clusters and molecules in a storage ring,” *Phys. Rev. Lett.*, vol. 87, p. 123401, Aug 2001.

[7] Y. Toker, O. Aviv, M. Eritt, M. L. Rappaport, O. Heber, D. Schwalm, and D. Zajfman, “Radiative cooling of $\mathrm{Al_4}^-$ clusters,” *Phys. Rev. A*, vol. 76, p. 053201, Nov 2007.

[8] S. Martin, J. Bernard, R. Brédy, B. Concina, C. Joblin, M. Ji, C. Ortega, and L. Chen, “Fast radiative cooling of anthracene observed in a compact electrostatic storage ring,” *Phys. Rev. Lett.*, vol. 110, p. 063003, Feb 2013.

[9] S. Menk, S. Das, K. Blaum, M. W. Froese, M. Lange, M. Mukherjee, R. Repnow, D. Schwalm, R. von Hahn, and A. Wolf, “Vibrational autodetachment of sulfur hexafluoride anions at its long-lifetime limit,” *Phys. Rev. A*, vol. 89, p. 022502, Feb 2014.

[10] C. Breitenfeldt, K. Blaum, S. George, J. Göck, G. Guzmán-Ramírez, J. Karthein, T. Kolling, M. Lange, S. Menk, C. Meyer, J. Mohrbach,

G. Niedner-Schatteburg, D. Schwalm, L. Schweikhard, and A. Wolf, "Long-term monitoring of the internal energy distribution of isolated cluster systems," *Phys. Rev. Lett.*, vol. 120, p. 253001, Jun 2018.

[11] E. K. Anderson, A. F. Schmidt-May, P. K. Najeeb, G. Eklund, K. C. Chartkunchand, S. Rosén, A. Larson, K. Hansen, H. Cederquist, H. Zettergren, and H. T. Schmidt, "Spontaneous Electron Emission from Hot Silver Dimer Anions: Breakdown of the Born-Oppenheimer Approximation," *Phys. Rev. Lett.*, vol. 124, p. 173001, Apr 2020.

[12] P. Rosmus and H. Werner, "Multireference-CI calculations of radiative transition probabilities in C_2^-," *The Journal of Chemical Physics*, vol. 80, pp. 5085–5088, 05 1984.

[13] U. Hefter, R. D. Mead, P. A. Schulz, and W. C. Lineberger, "Ultrahigh-resolution study of autodetachment in C_2^-," *Phys. Rev. A*, vol. 28, pp. 1429–1439, Sep 1983.

[14] B. D. Rehfuss, D. Liu, B. M. Dinelli, M. Jagod, W. C. Ho, M. W. Crofton, and T. Oka, "Infrared spectroscopy of carbo-ions. IV. The $A^2\Pi_u$–$X^2\Sigma_g^+$ electronic transition of C_2^-," *The Journal of Chemical Physics*, vol. 89, pp. 129–137, 07 1988.

[15] W. Shi, C. Li, H. Meng, J. Wei, L. Deng, and C. Yang, "Ab initio study of the low-lying electronic states of the C_2^- anion," *Computational and Theoretical Chemistry*, vol. 1079, pp. 57–63, 2016.

[16] H. B. Pedersen, C. Brink, L. H. Andersen, N. Bjerre, P. Hvelplund, D. Kella, and H. Shen, "Experimental investigation of radiative lifetimes of vibrational levels at the electronic ground state of C_2^-," *The Journal of Chemical Physics*, vol. 109, pp. 5849–5855, 10 1998.

[17] A. Naaman, K. G. Bhushan, H. B. Pedersen, N. Altstein, O. Heber, M. L. Rappaport, R. Moalem, and D. Zajfman, "Metastable states of negative carbon clusters: C_n^-, n=2-6," *The Journal of Chemical Physics*, vol. 113, pp. 4662–4667, 09 2000.

[18] T. Takao, S. Jinno, K. Hanada, M. Goto, K. Oshikiri, K. Okuno, H. Tanuma, T. Azuma, and H. Shiromaru, "Storage of negative carbon ions in an electrostatic ring," *Journal of Physics: Conference Series*, vol. 88, p. 012044, nov 2007.

[19] M. Iizawa, S. Kuma, N. Kimura, K. Chartkunchand, S. Harayama, T. Azuma, and Y. Nakano, "Photodetachment Spectroscopy of Highly Excited C_2^- and

Their Temporal Evolution in the Ion Storage Ring RICE," *Journal of the Physical Society of Japan*, vol. 91, no. 8, p. 084302, 2022.

[20] R. von Hahn, A. Becker, F. Berg, K. Blaum, C. Breitenfeldt, H. Fadil, F. Fellenberger, M. Froese, S. George, J. Göck, M. Grieser, F. Grussie, E. A. Guerin, O. Heber, P. Herwig, J. Karthein, C. Krantz, H. Kreckel, M. Lange, F. Laux, S. Lohmann, S. Menk, C. Meyer, P. M. Mishra, O. Novotný, A. P. O'Connor, D. A. Orlov, M. L. Rappaport, R. Repnow, S. Saurabh, S. Schippers, C. D. Schröter, D. Schwalm, L. Schweikhard, T. Sieber, A. Shornikov, K. Spruck, S. Sunil Kumar, J. Ullrich, X. Urbain, S. Vogel, P. Wilhelm, A. Wolf, and D. Zajfman, "The cryogenic storage ring CSR," *Rev. Sci. Instrum.*, vol. 87, p. 063115, June 2016.

[21] R. D. Thomas, H. T. Schmidt, G. Andler, M. Björkhage, M. Blom, L. Brännholm, E. Bäckström, H. Danared, S. Das, N. Haag, P. Halldén, F. Hellberg, A. I. S. Holm, H. A. B. Johansson, A. Källberg, G. Källersjö, M. Larsson, S. Leontein, L. Liljeby, P. Löfgren, B. Malm, S. Mannervik, M. Masuda, D. Misra, A. Orbán, A. Paál, P. Reinhed, K.-G. Rensfelt, S. Rosén, K. Schmidt, F. Seitz, A. Simonsson, J. Weimer, H. Zettergren, and H. Cederquist, "The double electrostatic ion ring experiment: A unique cryogenic electrostatic storage ring for merged ion-beams studies," *Review of Scientific Instruments*, vol. 82, p. 065112, 06 2011.

[22] L. H. Andersen, O. Heber, and D. Zajfman, "Physics with electrostatic rings and traps," *Journal of Physics B: Atomic, Molecular and Optical Physics*, vol. 37, p. R57, may 2004.

[23] H. B. Pedersen, A. Svendsen, L. S. Harbo, H. V. Kiefer, H. Kjeldsen, L. Lammich, Y. Toker, and L. H. Andersen, "Characterization of a new electrostatic storage ring for photofragmentation experiments," *Review of Scientific Instruments*, vol. 86, p. 063107, 06 2015.

[24] Y. Nakano, Y. Enomoto, T. Masunaga, S. Menk, P. Bertier, and T. Azuma, "Design and commissioning of the RIKEN cryogenic electrostatic ring (RICE)," *Review of Scientific Instruments*, vol. 88, p. 033110, 03 2017.

[25] K. Geistlinger, M. Fischer, S. Spieler, L. Remmers, F. Duensing, F. Dahlmann, E. Endres, and R. Wester, "A sub-4 Kelvin radio frequency linear multipole wire trap," *Review of Scientific Instruments*, vol. 92, p. 023204, 02 2021.

[26] C. Meyer, A. Becker, K. Blaum, C. Breitenfeldt, S. George, J. Göck, M. Grieser, F. Grussie, E. A. Guerin, R. von Hahn, P. Herwig, C. Krantz, H. Kreckel, J. Lion, S. Lohmann, P. M. Mishra, O. Novotný, A. P. O'Connor,

R. Repnow, S. Saurabh, D. Schwalm, L. Schweikhard, K. Spruck, S. Sunil Kumar, S. Vogel, and A. Wolf, “Radiative Rotational Lifetimes and State-Resolved Relative Detachment Cross Sections from Photodetachment Thermometry of Molecular Anions in a Cryogenic Storage Ring,” *Phys. Rev. Lett.*, vol. 119, p. 023202, Jul 2017.

[27] O. Novotný, P. Wilhelm, D. Paul, Ábel Kálosi, S. Saurabh, A. Becker, K. Blaum, S. George, J. Göck, M. Grieser, F. Grussie, R. von Hahn, C. Krantz, H. Kreckel, C. Meyer, P. M. Mishra, D. Muell, F. Nuesslein, D. A. Orlov, M. Rimmler, V. C. Schmidt, A. Shornikov, A. S. Terekhov, S. Vogel, D. Zajfman, and A. Wolf, “Quantum-state selective electron recombination studies suggest enhanced abundance of primordial HeH^+,” *Science*, vol. 365, no. 6454, pp. 676–679, 2019.

[28] F. Grussie, A. P. O’Connor, M. Grieser, D. Müll, A. Znotins, X. Urbain, and H. Kreckel, “An ion-atom merged beams setup at the Cryogenic Storage Ring,” *Review of Scientific Instruments*, vol. 93, p. 053305, 05 2022.

[29] W. Paul and M. Raether, “Das elektrische Massenfilter,” *Zeitschrift für Physik*, vol. 140, pp. 262–273, may 1955.

[30] K. Blaum, “High-accuracy mass spectrometry with stored ions,” *Physics Reports*, vol. 425, no. 1, pp. 1–78, 2006.

[31] D. Zajfman, Y. Rudich, I. Sagi, D. Strasser, D. Savin, S. Goldberg, M. Rappaport, and O. Heber, “High resolution mass spectrometry using a linear electrostatic ion beam trap,” *International Journal of Mass Spectrometry*, vol. 229, no. 1, pp. 55–60, 2003. Mass Spectrometry Contributions to Nanosciences and Nanotechnology.

[32] R. Diener, J. Dreyling-Eschweiler, H. Ehrlichmann, I. Gregor, U. Kötz, U. Krämer, N. Meyners, N. Potylitsina-Kube, A. Schütz, P. Schütze, and M. Stanitzki, “The DESY II test beam facility,” *Nuclear Instruments and Methods in Physics Research Section A: Accelerators, Spectrometers, Detectors and Associated Equipment*, vol. 922, pp. 265–286, 2019.

[33] D. W. Kerst, “The Acceleration of Electrons by Magnetic Induction,” *Phys. Rev.*, vol. 60, pp. 47–53, Jul 1941.

[34] M. Grieser, V. C. Schmidt, K. Blaum, F. Grussie, R. von Hahn, b. Kálosi, H. Kreckel, D. Müll, O. Novotný, F. Nuesslein, and A. Wolf, “Isochronous mass spectrometry in an electrostatic storage ring,” *Review of Scientific Instruments*, vol. 93, p. 063302, 06 2022.

[35] V. C. Schmidt, *Design of an ion beam extraction optics and analysis of the molecular composition of an ion beam in an electrostatic storage ring.* Bachelor's thesis, Heidelberg University, 2018.

[36] S. Schippers, P.-M. Hillenbrand, A. Perry-Sassmannshausen, T. Buhr, S. Fuchs, S. Reinwardt, F. Trinter, A. Müller, and M. Martins, "Vibrationally Resolved Inner-Shell Photoexcitation of the Molecular Anion C_2^- ," *ChemPhysChem*, vol. 24, no. 11, p. e202300061, 2023.

[37] K. Snowdon, W. Hentschke, and P. Hertel, "Rotational and Vibrational Excitation of Sputtered Diatomic Molecules," *Zeitschrift für Physik A - Atoms and Nuclei*, vol. 318, 1984.

[38] A. Wucher and B. J. Garrison, "Cluster formation in sputtering: A molecular dynamics study using the MD/MC-corrected effective medium potential," *J. Chem. Phys.*, vol. 105, pp. 5999–6007, 10 1996.

[39] C. Anders, R. Pedrys, and H. M. Urbassek, "Molecule emission from condensed Ar and O2 targets by 750eV Ne impact," *Nuclear Instruments and Methods in Physics Research Section B: Beam Interactions with Materials and Atoms*, vol. 352, pp. 195–201, 2015. Proceedings of the 12th International Conference on Computer Simulation of Radiation Effects in Solids, Alacant, Spain, 8-13 June, 2014.

[40] R. R. Corderman, P. C. Engelking, and W. C. Lineberger, "Laser photoelectron spectrometry measurement of characteristic electronic and vibrational temperatures of sputtered negative ions," *Appl. Phys. Lett.*, vol. 36, no. 7, pp. 533–535, 1980.

[41] Z. Nouri, R. Li, R. Holt, and S. Rosner, "A Penning sputter ion source with very low energy spread," *Nuclear Instruments and Methods in Physics Research Section A: Accelerators, Spectrometers, Detectors and Associated Equipment*, vol. 614, no. 2, pp. 174–178, 2010.

[42] S. Vogel, *Developments at an Electrostatic Cryogenic Storage Ring for Electron-Cooled keV Energy Ion Beams.* PhD thesis, Heidelberg University, 2016.

[43] H. Kreckel, O. Novotný, and A. Wolf, "Astrochemical studies at the Cryogenic Storage Ring," *Philosophical Transactions of the Royal Society A: Mathematical, Physical and Engineering Sciences*, vol. 377, no. 2154, p. 20180412, 2019.

[44] H. Poth, "Electron cooling: Theory, experiment, application," *Physics Reports*, vol. 196, no. 3, pp. 135–297, 1990.

[45] A. Kálosi, M. Grieser, R. von Hahn, U. Hechtfischer, C. Krantz, H. Kreckel, D. Müll, D. Paul, D. W. Savin, P. Wilhelm, A. Wolf, and O. c. v. Novotný, "Laser Probing of the Rotational Cooling of Molecular Ions by Electron Collisions," *Phys. Rev. Lett.*, vol. 128, p. 183402, May 2022.

[46] D. Paul, M. Grieser, F. Grussie, R. von Hahn, L. W. Isberner, Ábel Kálosi, C. Krantz, H. Kreckel, D. Müll, D. A. Neufeld, D. W. Savin, S. Schippers, P. Wilhelm, A. Wolf, M. G. Wolfire, and O. Novotný, "Experimental Determination of the Dissociative Recombination Rate Coefficient for Rotationally Cold CH^+ and Its Implications for Diffuse Cloud Chemistry," *The Astrophysical Journal*, vol. 939, p. 122, nov 2022.

[47] A. Kálosi, L. Gamer, M. Grieser, R. von Hahn, L. W. Isberner, J. I. Jäger, H. Kreckel, D. A. Neufeld, D. Paul, D. W. Savin, S. Schippers, V. C. Schmidt, A. Wolf, M. G. Wolfire, and O. Novotný, "Dissociative Recombination of Rotationally Cold OH+ and Its Implications for the Cosmic Ray Ionization Rate in Diffuse Clouds," *The Astrophysical Journal Letters*, vol. 955, p. L26, sep 2023.

[48] A. P. O'Connor, A. Becker, K. Blaum, C. Breitenfeldt, S. George, J. Göck, M. Grieser, F. Grussie, E. A. Guerin, R. von Hahn, U. Hechtfischer, P. Herwig, J. Karthein, C. Krantz, H. Kreckel, S. Lohmann, C. Meyer, P. M. Mishra, O. Novotný, R. Repnow, S. Saurabh, D. Schwalm, K. Spruck, S. Sunil Kumar, S. Vogel, and A. Wolf, "Photodissociation of an Internally Cold Beam of CH^+ Ions in a Cryogenic Storage Ring," *Phys. Rev. Lett.*, vol. 116, p. 113002, Mar 2016.

[49] D. Müll, F. Grussie, K. Blaum, S. George, J. Göck, M. Grieser, R. von Hahn, Z. Harman, A. Kálosi, C. H. Keitel, C. Krantz, C. Lyu, O. Novotný, F. Nuesslein, D. Paul, V. C. Schmidt, S. Singh, S. Sunil Kumar, X. Urbain, A. Wolf, and H. Kreckel, "Metastable states of Si^- observed in a cryogenic storage ring," *Phys. Rev. A*, vol. 104, p. 032811, Sep 2021.

[50] K. Spruck, A. Becker, F. Fellenberger, M. Grieser, R. von Hahn, V. Klinkhamer, O. Novotný, S. Schippers, S. Vogel, A. Wolf, and C. Krantz, "An efficient, movable single-particle detector for use in cryogenic ultra-high vacuum environments," *Review of Scientific Instruments*, vol. 86, p. 023303, 02 2015.

[51] A. Becker, *Imaging of Neutral Fragmentation Products from Fast Molecular Ion Beams: Paving the Way for Reaction Studies in Cryogenic Environment.* PhD thesis, Heidelberg University, 2016.

[52] F. Herrmann, *in preparation.* PhD thesis, Heidelberg University.

[53] K. Kromer, C. Lyu, M. Door, P. Filianin, Z. Harman, J. Herkenhoff, P. Indelicato, C. H. Keitel, D. Lange, Y. N. Novikov, C. Schweiger, S. Eliseev, and K. Blaum, "Observation of a Low-Lying Metastable Electronic State in Highly Charged Lead by Penning-Trap Mass Spectrometry," *Phys. Rev. Lett.*, vol. 131, p. 223002, Nov 2023.

[54] B. Franzke, H. Geissel, and G. Münzenberg, "Mass and lifetime measurements of exotic nuclei in storage rings," *Mass Spectrometry Reviews*, vol. 27, no. 5, pp. 428–469, 2008.

[55] X. Tu, M. Wang, Y. Litvinov, Y. Zhang, H. Xu, Z. Sun, G. Audi, K. Blaum, C. Du, W. Huang, Z. Hu, P. Geng, S. Jin, L. Liu, Y. Liu, B. Mei, R. Mao, X. Ma, H. Suzuki, P. Shuai, Y. Sun, S. Tang, J. Wang, S. Wang, G. Xiao, X. Xu, J. Xia, J. Yang, R. Ye, T. Yamaguchi, X. Yan, Y. Yuan, Y. Yamaguchi, Y. Zang, H. Zhao, T. Zhao, X. Zhang, X. Zhou, and W. Zhan, "Precision isochronous mass measurements at the storage ring CSRe in Lanzhou," *Nuclear Instruments and Methods in Physics Research Section A: Accelerators, Spectrometers, Detectors and Associated Equipment*, vol. 654, no. 1, pp. 213–218, 2011.

[56] W. R. Plaß, T. Dickel, and C. Scheidenberger, "Multiple-reflection time-of-flight mass spectrometry," *International Journal of Mass Spectrometry*, vol. 349-350, pp. 134–144, 2013. 100 years of Mass Spectrometry.

[57] H. Wollnik and M. Przewloka, "Time-of-flight mass spectrometers with multiply reflected ion trajectories," *International Journal of Mass Spectrometry and Ion Processes*, vol. 96, no. 3, pp. 267–274, 1990.

[58] M. Hausmann, F. Attallah, K. Beckert, F. Bosch, A. Dolinskiy, H. Eickhoff, M. Falch, B. Franczak, B. Franzke, H. Geissel, T. Kerscher, O. Klepper, H.-J. Kluge, C. Kozhuharov, K. Löbner, G. Münzenberg, F. Nolden, Y. Novikov, T. Radon, H. Schatz, C. Scheidenberger, J. Stadlmann, M. Steck, T. Winkler, and H. Wollnik, "First isochronous mass spectrometry at the experimental storage ring ESR," *Nuclear Instruments and Methods in Physics Research Section A: Accelerators, Spectrometers, Detectors and Associated Equipment*, vol. 446, no. 3, pp. 569–580, 2000.

[59] T. Dickel, M. I. Yavor, J. Lang, W. R. Plaß, W. Lippert, H. Geissel, and C. Scheidenberger, "Dynamical time focus shift in multiple-reflection time-of-flight mass spectrometers," *International Journal of Mass Spectrometry*, vol. 412, pp. 1–7, 2017.

[60] S. Bandelow, F. Martinez, S. König, and L. Schweikhard, "Production of polyanionic aluminium clusters with up to 10 excess electrons," *International Journal of Mass Spectrometry*, vol. 473, p. 116780, 2022.

[61] M. Grieser, R. von Hahn, S. Vogel, and A. Wolf, "The phase slip factor of the electrostatic cryogenic storage ring CSR," *Journal of Physics: Conference Series*, vol. 874, no. 012049, 2017.

[62] F. Nuesslein, *Storage ring experiments on the stability of negative ions in the gas phase.* PhD thesis, Heidelberg University, 2024.

[63] NIST, "Atomic Weights and Isotopic Compositions for All Elements." `https://physics.nist.gov/cgi-bin/Compositions/stand_alone.pl`.

[64] T. Orlemann, *Multi-frequency search in discrete sparse data for isochronous mass spectrometry at CSR.* Bachelor's thesis, Heidelberg University, 2024.

[65] G. Herzberg and A. Lagerqvist, "A new spectrum associated with diatomic carbon," *Canadian Journal of Physics*, pp. 2363–2373, 1968.

[66] R. D. Mead, U. Hefter, P. A. Schulz, and W. C. Lineberger, "Ultrahigh resolution spectroscopy of C_2^-: The $A^2\Pi_u$ state characterized by deperturbation methods," *The Journal of Chemical Physics*, vol. 82, pp. 1723–1731, 02 1985.

[67] J. D. Watts and R. J. Bartlett, "Coupled-cluster calculations on the C2 molecule and the C_2^+ and C_2^- molecular ions," *The Journal of Chemical Physics*, vol. 96, pp. 6073–6084, 04 1992.

[68] A. E. Bragg, R. Wester, A. V. Davis, A. Kammrath, and D. M. Neumark, "Excited-state detachment dynamics and rotational coherences of C_2^- via time-resolved photoelectron imaging," *Chemical Physics Letters*, vol. 376, no. 5, pp. 767–775, 2003.

[69] T. [Sbreve]edivcová and V. [Sbreve]pirko, "Potential energy and transition dipole moment functions of C_2^-," *Molecular Physics*, vol. 104, no. 13-14, pp. 1999–2005, 2006.

[70] P. L. Jones, R. D. Mead, B. E. Kohler, S. D. Rosner, and W. C. Lineberger, "Photodetachment spectroscopy of C_2^- autodetaching resonances," *The Journal of Chemical Physics*, vol. 73, pp. 4419–4432, 07 2008.

[71] S. Iida, S. Kuma, H. Tanuma, T. Azuma, and H. Shiromaru, "State-Selective Observation of Radiative Cooling of Vibrationally Excited C_2^-," *The Journal of Physical Chemistry Letters*, vol. 11, no. 24, pp. 10526–10531, 2020. PMID: 33289570.

[72] M. Nötzold, R. Wild, C. Lochmann, and R. Wester, "Spectroscopy and ion thermometry of C_2^- using laser-cooling transitions," *Phys. Rev. A*, vol. 106, p. 023111, Aug 2022.

[73] J. M. Göck, *A novel approach for mid-infrared spectroscopy of large carbon systems and the nonthermal fragmentation process of diatomic anions.* PhD thesis, Heidelberg University, 2020.

[74] R. J. Le Roy, "LEVEL: A computer program for solving the radial Schrödinger equation for bound and quasibound levels," *Journal of Quantitative Spectroscopy and Radiative Transfer*, vol. 186, pp. 167–178, 2017. Satellite Remote Sensing and Spectroscopy: Joint ACE-Odin Meeting, October 2015.

[75] V. C. Schmidt, *Competition of detachment, dissociation, and radiative decay channels in highly excited* C_2^-. Master's thesis, Heidelberg University, 2020.

[76] C. Krantz, O. Novotný, A. Becker, S. George, M. Grieser, R. von Hahn, C. Meyer, S. Schippers, K. Spruck, S. Vogel, and A. Wolf, "Single-particle detection of products from atomic and molecular reactions in a cryogenic ion storage ring," *Nuclear Instruments and Methods in Physics Research Section A: Accelerators, Spectrometers, Detectors and Associated Equipment*, vol. 851, pp. 92–102, 2017.

[77] P. F. Bernath, *Spectra of Atoms and Molecules.* Oxford University Press, third ed., 2016.

[78] G. Halmová, J. D. Gorfinkiel, and J. Tennyson, "Low-energy electron collisions with C_2 using the R-matrix method," *Journal of Physics B: Atomic, Molecular and Optical Physics*, vol. 39, p. 2849, jun 2006.

[79] G. Halmová, *R-matrix calculations of electron-molecule collisions with* C_2 *and* C_2^-. PhD thesis, University College London, 2008.

[80] H. J. Werner, P. J. Knowles, R. Lindh, F. R. Knizia, F. R. Manby, M. Schütz, and Others, "MOLPRO, version 2012.1, a package of ab initio programs," 2012.

[81] J. Dunning, Thom H., "Gaussian basis sets for use in correlated molecular calculations. I. The atoms boron through neon and hydrogen," *The Journal of Chemical Physics*, vol. 90, pp. 1007–1023, 01 1989.

[82] P. G. Burke, I. Mackey, and I. Shimamura, "R-matrix theory of electron-molecule scattering," *Journal of Physics B: Atomic and Molecular Physics*, vol. 10, p. 2497, aug 1977.

[83] K. M. Ervin and W. Lineberger, "Photoelectron spectra of dicarbon (1-) and ethynyl (1-)," *The Journal of Physical Chemistry*, vol. 95, no. 3, pp. 1167–1177, 1991.

[84] S.-I. Lu, "Electron affinities with diffusion quantum Monte Carlo for C2 and BO molecules," *The Journal of Chemical Physics*, vol. 121, pp. 10495–10497, 12 2004.

[85] J. M. Blatt, "Practical points concerning the solution of the Schrödinger equation," *Journal of Computational Physics*, vol. 1, no. 3, pp. 382–396, 1967.

[86] J. K. Watson, "Hönl–London factors for multiplet transitions in Hund's case a or b," *Journal of Molecular Spectroscopy*, vol. 252, no. 1, pp. 5–8, 2008.

[87] A. Hansson and J. K. Watson, "A comment on Hönl-London factors," *Journal of Molecular Spectroscopy*, vol. 233, no. 2, pp. 169–173, 2005.

[88] S. Leutwyler, J. P. Maier, and L. Misev, "Lifetimes of C_2^- in rotational levels of the $B^2\Sigma_u^+$ state in the gas phase," *Chemical Physics Letters*, vol. 91, no. 3, pp. 206–208, 1982.

[89] E. P. Wigner, *On the Matrices Which Reduce the Kronecker Products of Representations of S. R. Groups.* Berlin, Heidelberg: Springer Berlin Heidelberg, 1993.

[90] V. C. Schmidt, R. Čurík, M. Ončák, K. Blaum, S. George, J. Göck, M. Grieser, F. Grussie, R. von Hahn, C. Krantz, H. Kreckel, O. Novotný, K. Spruck, and A. Wolf, "Unimolecular processes in diatomic carbon anions at high rotatinal excitation." `https://doi.org/10.48550/arXiv.2405.06493`. *to be submitted to Phys. Rev. A.*

[91] N. Douguet, S. Fonseca dos Santos, M. Raoult, O. Dulieu, A. E. Orel, and V. Kokoouline, "Theoretical study of radiative electron attachment to CN, C_2H, and C_4H radicals," *The Journal of Chemical Physics*, vol. 142, p. 234309, 06 2015.

[92] R. Čurík. private communications, 2023.

[93] P. Jasik, J. Franz, D. Kędziera, T. Kilich, J. Kozicki, and J. E. Sienkiewicz, "Spontaneous electron emission vs dissociation in internally hot silver dimer anions," *The Journal of Chemical Physics*, vol. 154, p. 164301, 04 2021.

[94] M. Ončák. private communications, 2020.

[95] V. C. Schmidt, R. Čurík, M. Ončák, K. Blaum, S. George, J. Göck, M. Grieser, F. Grussie, R. von Hahn, C. Krantz, H. Kreckel, O. Novotný, K. Spruck, and A. Wolf, "Autodetachment of diatomic carbon aionis from long-lived high-rotation quartet states." `https://doi.org/10.48550/arXiv.2405.06514`. *to be submitted to Phys. Rev. Lett.*

[96] R. Golser, H. Gnaser, W. Kutschera, A. Priller, P. Steier, A. Wallner, M. Čížek, J. Horáček, and W. Domcke, "Experimental and Theoretical Evidence for Long-Lived Molecular Hydrogen Anions ${H_2}^-$ and ${D_2}^-$," *Phys. Rev. Lett.*, vol. 94, p. 223003, Jun 2005.

[97] R. Marion, M. Čížek, and X. Urbain, "Autodetachment spectroscopy of metastable ${D_2}^-$ and HD^-," *Phys. Rev. A*, vol. 107, p. 052808, May 2023.

[98] M. Čížek and K. Houfek, "Nonlocal theory of resonance electron-molecule scattering," in *Low-energy electron scattering from molecules, biomolecules and surfaces* (P. Čársky and R. Čurík, eds.), ch. 4, pp. 91–125, Boca Raton: CRC Press, 1 ed., 2012.

[99] H. Urbassek, "Sputtering of molecules," *Nuclear Instruments and Methods in Physics Research Section B: Beam Interactions with Materials and Atoms*, vol. 18, no. 1, pp. 587–595, 1986.

[100] A. Wucher, "Internal energy of sputtered metal clusters," *Phys. Rev. B*, vol. 49, pp. 2012–2020, Jan 1994.

[101] A. Znotiņš, *Electron recombination of rotationally cold deuterated triatomic hydrogen ions at the Cryogenic Storage Ring.* PhD thesis, Heidelberg University, 2024.

[102] C. Heinemann, W. Koch, G.-G. Lindner, and D. Reinen, "Electronic spectrum of S_2^-, the electron affinity of S_2, and the binding energies of neutral and anionic S_3 clusters," *Phys. Rev. A*, vol. 52, pp. 1024–1038, Aug 1995.

Part I

Appendix

A Lists

A.1 List of Figures

A.2 List of Tables

Acknowledgements

This thesis would not have been possible without the help of a large group of people. Even though this section will never do my gratitude justice, I would still like to thank them here.

First of all, I would like to thank Prof. Dr. Klaus Blaum for his unwavering support in the last ∼ 9 years (I started at the institute as a HiWi in my first Bachelor semester). He has not only strongly influenced and promoted my scientific career during the supervising of my Bachelor-, Master- and now PhD-thesis, but he has also enabled me to (in an arguably rather feisty manner) fight for the interests of my fellow students in last years in the role of PhD representative. I am sure, there are very few students out there with the privilege to tell considerably more senior people their unfiltered opinion, knowing full well their supervisor will fight it out for them if that behaviour gets them into trouble. To draw a comparison to my favourite fictional character during childhood: Klaus is my Dumbledore.

My gratitude goes out to Prof. Dr. Roland Wester, who kindly agreed to be my second examiner even though that not only meant reading and writing a report on this thesis but also travelling all the way from Innsbruck for the defence.

I would also like to thank PD Dr. Zoltan Harman and Prof. Dr. Mark Ladd for being members of my defence committee.

My endless gratitude goes out to Dr. Oldřich Novotný, my group leader. Not only is he my go-to example for truly excellent supervision, he has also patiently endured and often even participated in my endless list of shenanigans over the years. These ranged from being a member of committees I made up (like the "CSR present committee") all the way to showering office plants to dust them off. He also thoroughly proof-read this thesis.

Besides my formal and informal supervisor, I had the great privilege to (unofficially) be supervised by two additional, truly exceptional physicists whom I would like to express my gratitude to. One of them is Dr. Manfred Grieser, the lord of the rings. His profound understanding of storage ring physics, which he is always willing to patiently share with everyone, made the isochronous operation of the CSR possible. He is also one of the kindest people I know. The other is Apl. Prof. Dr. Andreas Wolf who was mainly, but not only, involved in the C_2^- project. It is safe to say that the detailed investigation of the decay rates of the dimer, especially the radiative channel, would not have been possible in this form without him. His approach to derive mathematical descriptions from scratch if no satisfying model can be found in literature is inspiring. He might be an experimentalist, but, to quote a gifted theoretician: "Andreas could put many theorists to shame".

The C_2^- project would not have been possible without the collaboration with two quantum chemists I would like to thank here. One is Ass. Prof. Dr. Milan Ončák, who carried out the *ab initio* calculations. He also patiently answered all of our questions about those calculations in the subsequent three years while we were

working out how to calculate all the decay rates. The other one is Dr. Roman Čurík, who was not only willing to look into rate calculations for all AD processes we could possible think of, but actually managed to work out how to do them. Especially the derivation of the theory for rotationally assisted auto-detachment was very difficult and I assume there are very few people who could have managed that.

I was very lucky to be part of (arguably) the best research group out there. I would like to thank everyone in the CSR team, who has made my time here so wonderful. After nine years, the amount of things to be grateful for could probably fill another thesis, so I will restrict myself to some highlights here. I would like to thank Dr. Florian Grussie and PD Dr. Holger Kreckel for always having an open door to answer any CSR- or physics-related (or unrelated) questions that came up. I would like to thank Dirk Kaiser for being my tea-buddy (and his wife Sabine for constantly supplying us with delicious cakes from her Café Polly for tea-time). I would like thank the "junior" scientists, Dr. Felix Nüßlein, Dr. Damian Müll, Dr. Daniel Paul, Dr. Lisa Gamer, Leonard Isberner, Christopher Jakob, Lukas Berger, Dr. Aigars Znotiņš, Dr. Ábel Kálosi, Selina Gaisser, Annika Oetjens, Julia Jäger, Lauren Seeger, Jonas Bechtel, Tobias Orlemann and Bhalchandra Choudhari, for all of the great (after) work distractions like viking chess games or ice cream breaks. Ein großer Dank geht auch an das technische Team des CSRs, Rolf Epking, Natalie Zahn, Erik Werner, Oliver Koschorreck, Manfred König, Max Trebis, Elmar Scheurich und Kevin Hebert. Nicht nur sorgen sie dafür, dass alles am CSR auch läuft, sie sind auch immer sofort zur Stelle, wenn man mal Hilfe braucht.

I would like to thank the people, who have fought alongside me for the interests of PhD students. At the MPIK, these are especially my fellow PhD representatives over the years, Dr. Kathrin Kromer, Stefan Dickopf and Annabelle Kaiser, as well as our two excellent PhD contact people PD Dr. Teresa Marrodan Undagoitia and Dr. Brian Reville. At Heidelberg university, a special thank you goes to my fellow PhD senators in the last three years, Dr. Marvin Möhler, Dr. Franziska Grün, Christina Schmidt, Hannah Klein and Matthias Heil as well as the head of the Graduate Academy, Dr. Helke Hillebrand.

I would also like to thank my friends, especially the "LeBinPhys", for their support and companionship over the years and also for not being mad that I have once again been neglecting them in the final stages of writing a thesis. I would like to thank my partner Dr. Michael Quin for providing me both with a counter-balance to work and also with food during the writing stage of this thesis and also for letting me share my life with him. Last, but not least, I would like to express my endless gratitude to my family for their unconditional support, especially my parents Katharina Wegner and Helmut Schmidt and my sister Laura Schmidt.